SURFACE REACTIONS OF LOW ENERGY ELECTRONS AND IONS WITH ORGANOMETALLIC PRECURSORS FOR CHARGED PARTICLE DEPOSITION PROCESSES

by

Rachel M. Thorman

A dissertation submitted to Johns Hopkins University

in conformity with the requirements for the degree of

Doctor of Philosophy

Baltimore, Maryland

March 2020

Abstract

Focused electron beam induced deposition (FEBID) and focused ion beam induced deposition (FIBID) are maskless, resistless nanofabrication techniques that are capable of directly writing three-dimensional nanostructures onto surfaces with nonplanar topographies, making both techniques distinctly versatile. In FEBID and FIBID, tightly focused beams of electrons or ions create metal-containing nanostructures by decomposing organometallic precursors in low pressure environments. Deposit purity is often limited by incomplete precursor decomposition and ligand co-deposition; consequently, understanding the interactions of electrons and ions with surface-bound organometallic precursors is fundamental to improve the purity of nanostructures produced by these processes.

The primary aim of this dissertation is to show that a low temperature, UHV surface science approach can be used to study the reactions of both low energy electrons and ions with organometallic precursors. In these experiments, X-ray photoelectron spectroscopy (XPS) and mass spectroscopy (MS) are used to study the interactions of low energy electrons and ions with nanometer-thick films of physisorbed precursors. Additionally, electron beam induced deposition (EBID) and ion beam induced deposition (IBID)

performed in UHV chambers are used to bridge the gap between the well-controlled UHV experiments and deposition performed in high vacuum environments. First, a study of low energy electron and ion interactions with adsorbed $(\eta^5\text{-Cp})\text{Fe(CO)}_2\text{Re(CO)}_5$ showed markedly different electron- and ion-induced decomposition reactions. Further, low energy electron interactions with $\text{Ru(CO)}_4\text{I}_2$ in the gas phase and on surfaces were compared with EBID performed in a UHV chamber, elucidating the low energy electron-induced decomposition reactions that induce deposition for this molecule. These results were also compared to low energy argon ion interactions with adsorbed $\text{Ru(CO)}_4\text{I}_2$, showing different decomposition. Finally, the kinetics of low energy electron-induced decomposition of adsorbed Fe(CO)_5 were studied and compared to ion-induced decomposition and IBID performed with Fe(CO)_5 in a UHV chamber. It is hoped that these contributions will expand the current understanding of electron and ion interactions with organometallic molecules that underly deposition in FEBID and FIBID, as well as inform the design and selection of new precursors.

Primary Reader and Advisor: Dr. D. Howard Fairbrother
Secondary Reader: Dr. Kit H. Bowen
Secondary Reader: Dr. Paul J. Dagdigian

Acknowledgments

Although the writing of this PhD thesis has been a fairly solitary effort, the work that has gone into producing the research that comprises the thesis has been anything but solitary. There are many important people who have supported me through the years of this PhD - academically, socially, and emotionally - and I am glad to have this opportunity to thank them.

First, I would like to thank past and present members of the Fairbrother lab. I would especially like to thank Dr. Julie Spencer and Dr. Michael Barclay, who taught me most of what I know about the vacuum instrumentation that I used in this thesis. I would also like to thank former member Dr. Joshua Wnuk, who set me on this journey when I was an undergraduate at Princeton and had the wonderful luck to work with him as a postdoc in Professor Steven Bernasek's lab. I would also like to thank former members Dr. David Goodwin, Dr. Miranda Gallagher, Dr. Ronald Lankone, Dr. David Durkin, and Dominique Porcincula and current members Benjamin Frank, Leslie Sigmon, Alexa Wallace, Casey Smith, Sophia Sommerkamp, Dr. Alyssa Deline, and Dr. Arancha Fernández for all their help and friendship over the past years. Your presence has made laboratory work more fun and kept me sane. A special thanks must also go to the JHU chemistry department administrators and

support staff. I'd particularly like to thank Boris Steinberg for his constant help with fixing and modifying instruments and for putting out all the little fires that stand in the way of accomplishing research in the chemistry department.

I would also like to thank my collaborators - particularly the Ingólfsson laboratory at the University of Iceland, where I got my first PhD in Chemistry. I would especially like to thank my former advisor, Professor Oddur Ingólfsson for his fantastic mentorship, Dr. Pernille Ahlmann Jensen for a great collaboration, and Dr. Ragesh Kumar T. P., Dr. Benedikt Ómarsson, and Dr. Frímann Ómarsson for their help and support. I would also like to thank Elif Bilgilisoy at Friedrich Alexander University Erlangen-Nürnberg for her collaboration and friendship. Professor Lisa McElwee-White and her group deserve a special thanks for several years of fruitful collaboration. Finally, I would like to thank Professor Paul Dagdigian and Professor Kit Bowen for serving as my PhD committee.

My PhD advisor, Professor Howard Fairbrother, has been a true mentor for me. He has taught me a great deal about science, as well as challenged me to dive deeper into the fundamental chemistry that underlies our field. I am grateful for his advice and motivation, as well as his shipping me off to Iceland for three years, where I received an extra PhD and met my husband.

Finally, I would like to thank my friends and family for their love and support. Thank you to my parents: Dr. Raymond Thorman, Patricia Thorman, and Dr. John Hallowell for your encouragement and for trying to make sure I'm still have fun even when I'm buried in work. Thank you to my brother and sister-in-law, Dan and Aly Thorman, for always showing up for me. Thank

Table of Contents

List of Tables

List of Figures

Chapter 1

Introduction

In 1965, Gordon E. Moore published the seminal article "Cramming more components onto integrated circuits," in which he theorized about the future of integrated electronics, observing that the number of components in an integrated circuit had historically doubled each year since 1962 and suggesting that this trend might continue.[1] In 1975, Moore revised his prediction to reflect a doubling of components per chip every two years by 1980,[2] while his colleague, David House, noted that the continuation of this trend would double computational performance approximately every 18 months.[3] The semiconductor industry has aggressively pursued a continuation of that prediction, known today as Moore's Law, which has proven accurate for many decades. In order to pack an increasing number of components into integrated circuits, components have been shrunk smaller and smaller over that time. In 2017, Intel introduced the 10 nm generation of chips, packing over 100 million transistors into each square millimeter of chip.[4] As the size of chip features approaches the limits of conventional lithography, innovations in nanofabrication technology are increasingly necessary in order to maintain

the rate of increasing computational performance.

The ability to produce ever-smaller nanostructures with controllable size, shape, and composition is thus increasingly important in a wide variety of fields. Nanoscale plasmonic structures, which must have high metal purities and well-defined structures,[5] can be used to break the diffraction limit of optical integrated circuits.[6–9] High purity metallic nanostructures also have applications in nanoelectronics[10] and nanosensing.[11]

Many innovative top-down methods exist to produce such nanostructures, including conventional photolithography, extreme ultraviolet lithography (EUVL), and electron beam lithography (EBL). These techniques are considered planar processes and have a number of important advantages, including high throughput (photolithography), and high precision within their respective ranges of resolution. However, optical lithography methods require the use of masks, and both optical and electron lithography require the use of resists. Additionally, conventional lithography techniques require a large number of steps involving many different masks and resists in order to produce a complete device. As the required dimensions of nanostructures reduces to sub-100 nanometers, these requirements increase the potential for both propagation of errors from masks and contamination from resists.

Focused electron beam induced deposition (FEBID) and focused ion beam induced deposition (FIBID) are bottom-up nanofabrication techniques that take advantage of the tight focus achievable with a high energy charged particle (electron or ion) beam to directly write three-dimensional nanostructures onto nonplanar surfaces.[12–14] In both techniques, a gaseous precursor

molecule (generally an organometallic compound) is introduced into a high vacuum chamber equipped with a high energy (1 – 30 keV) charged particle beam, which impacts a substrate. Electron or ion-driven reactions cause the precursor molecule to decompose on the substrate in a spatially localized area defined by the tightly-focused high energy charged particle beam. Patterns may be drawn on the substrate by moving the charged particle beam in the x and y directions, while vertical growth may be controlled through variation of dwell time at a particular point. Neither technique requires the use of masks or resists, and both techniques can produce complex three-dimensional nanostructures in a single step.

While both FEBID and FIBID can be considered relatively recent deposition techniques compared to conventional photolithography methods, they have each found commercial use. Both techniques have been used industrially to repair photomasks used in conventional photolithography;[15, 16] Zeiss manufactures a commercial FEBID tool for repair of extreme ultra-violet (EUV) and high durable phase shifting masks (HD PS).[17] Additionally, both techniques have been used in the fabrication of high-resolution atomic force microscopy (AFM) tips.[18, 19] FIBID-fabricated tips have been found to have poorer resolution than FEBID tips;[12] however, focused ion beams also have the ability to trim the scanning probe sensors, increasing their desirability in this application.[20]

One outstanding issue facing the practical applications of both FEBID and FIBID is that deposits created from organometallic precursors are rarely composed exclusively of the desired metal (i.e., 100% metal purity). For example,

3

metal purities for nanostructures deposited by both FEBID and FIBID from MeCpPtMe$_3$, a popular precursor, typically have purities of < 20 at. % Pt.[21, 22] Strategies used to the increase purity of FEBID and FEBID nanostructures generally fall into three categories: post-deposition purification, *in situ* deposit purification, and precursor choice.[12–14, 23]

Post-deposition processing of FEBID and FIBID structures includes strategies such as annealing, which has been found to improve both conductivity and purity. For example, *in vacuo* annealing of nanowires deposited from Co(CO)$_3$NO using both FEBID and FIBID decreased resistivity of both type of nanowire, although the decrease was much greater for the FEBID-deposited nanowires due to their initial high resistivity.[24] Reactive gases can also be used – when deposits made from FEBID and FIBID using MeCpPtMe$_3$ were annealed in O$_2$ at 500 °C, the deposit purities increased from 6 – 50 at. % Pt and 19 – 30 at. % Pt, respectively.[25] Additionally, annealing wires deposited using FEBID from WF$_6$ to 500 °C under an atmosphere of H$_2$ was found to increase conductance by 1 – 3 orders of magnitude,[26] while annealing FEBID deposits made from (η^3-C$_3$H$_5$)Ru(CO)$_3$Br to 300 °C under an atmosphere of forming gas increased ruthenium content from 23 – 83 at. %.[27] Another post-deposition strategy that has been explored is the use of atomic hydrogen, which was successfully used to remove most of the residual chlorine from PtCl$_2$ deposits made using FEBID from the precursor Pt(CO)$_2$Cl$_2$.[28] Oxygen plasma cleaning has also been used to improve the purity of FEBID deposits made from Me$_2$Au(acac).[29]

Deposit purification strategies used *in situ* during deposition include

the use of coreactants as well as specialized stage modifications. Codosing MeCpPtMe$_3$ with O$_2$ during FEBID and FIBID produced decreased C/Pt ratios from about 0.78 – 0.18 and 0.61 – 0.27, respectively.[30] Additionally, codosing Pt(PF$_3$)$_4$ with O$_2$ during FEBID caused deposit purity to rise from about 16 – 25 at. % Pt.[31] Water has been used as an oxidative enhancer during the deposition of gold from Me$_2$Au(tfac) using FEBID, increasing deposit purity from 30 at. % Au to approximately pure gold nanostructures.[32] Another *in situ* purification technique that has been explored is increasing the substrate temperature; heating the Cr-coated Si(100) substrate to 80 °C when performing FEBID using Pt(PF$_3$)$_4$ produced a further increase in deposit purity to 60 at. % Pt.[31]

Although each of these methods can produce highly pure nanostructures, they can also have some drawbacks. Annealing is known to change nanostructure morphology and may also cause deformation. While the FEBID deposits made from (η^3-C$_3$H$_5$)Ru(CO)$_3$Br and annealed under forming gas had improved metal purity, the deposits also experienced significant volume loss (79%), largely in the vertical dimension.[27] Additionally, atomic hydrogen cleaning of FEBID deposits made from Pt(CO)$_2$Cl$_2$ was found to produce porous structures, which can lead to diminished structural integrity of deposited nanostructures.[28] Although FEBID deposits made from Me$_2$Au(acac) and exposed to oxygen plasma had decreased carbon content, their surface roughness increased.[29] Use of O$_2$ as a coreactant with Pt(PF$_3$)$_4$ during FEBID increased the platinum purity of the deposits, but also resulted in incorporation of oxygen into the deposited structure.[31] Such issues may limit the

implementation of these strategies in FEBID and FIBID.

The most direct method used to improve the purity of nanostructures made using FEBID and FIBID is through precursor selection and design. Most precursors currently used commercially were developed for use in chemical vapor deposition (CVD), a technique in which organometallic precursors are thermally decomposed under high vacuum conditions in order to deposit a thin film of pure metal. While these precursors are therefore optimal for thermally-induced decomposition, they may not be ideal candidates for electron- or ion-induced decomposition. To improve the purity of FEB- and FIB-grown deposits and therefore the utility of these charged particle deposition strategies, it is thus critically important to understand the molecular-level bond-breaking processes that occur during deposition. Some success has already been achieved in the development of gold precursors for FEBID, with Au(I) precursors $ClAuPF_3$ and $ClAuCO$, which were found to produce deposits with low resistivity (22 $\mu\Omega$cm from $ClAuPF_3$)[33] and high purity (> 95 at. % Au from $ClAuCO$).[34] However, these compounds were found to be highly sensitive to air and water, as well as being sensitive to thermal decomposition, making them unsuitable for commercial use.[33–35] Another compound that has shown promise as a FEBID precursor is $Pt(CO)_2Cl_2$, which has been shown to make carbon-free nanostructures,[28, 36] although residual chlorides must be removed by, e.g., atomic hydrogen cleaning.

While FEBID is now generally known to proceed by an initial step involving several low energy electron-induced decomposition reactions,[37] the underlying reactions driving deposition in FIBID are less understood. To

address this issue, we undertook a molecular-level approach to compare the sequences of bond-breaking steps that occur when an organometallic precursor physisorbed onto an inert substrate is exposed to either argon ions or electrons. This study demonstrated that a low temperature, ultra-high vacuum (UHV) surface science approach can serve as a platform to study and compare the reactions of low energy electrons (500 eV) and ions (800 eV Ar^+ ions) with organometallic precursors. The precursor $(\eta^5\text{-Cp})Fe(CO)_2Re(CO)_5$ was used as an illustrative example of an organometallic complex with different metal centers and ligand types. By comparing the different decomposition behavior of adsorbed $CpFe(CO)_2Re(CO)_5$ upon exposure to 500 eV electrons and 860 eV Ar^+ ions, we were able to demonstrate that, under electron- and ion-limited conditions, FEBID and FIBID of this molecule proceed via distinctly different mechanisms. Additionally, we elucidated the differing bond-breaking reactions underlying deposition in FEBID and FIBID of $CpFe(CO)_2Re(CO)_5$.[38]

Gas phase studies of the low energy electron-induced decomposition of organometallic molecules can be used to elucidate the electron-driven reactions that underly deposition in FEBID. To this end, the low-energy electron-induced decomposition of $Ru(CO)_4I_2$ in the gas phase and adsorbed on surfaces was studied and compared to FEBID deposits made from $Ru(CO)_4I_2$ in order to determine the initial electron-induced bond-breaking step leading to deposition in FEBID of $Ru(CO)_4I_2$ and to understand its impact on the ultimate composition of the deposit. Taken together, these studies showed that FEBID of $Ru(CO)_4I_2$ likely proceeds via an initial DEA-induced decomposition step and may ultimately produce carbon-free deposits. Additionally, the kinetics

of low energy argon ion-induced decomposition of adsorbed $Ru(CO)_4I_2$ were studied, showing that FIBID using $Ru(CO)_4I_2$ may produce pure ruthenium deposits.

The low temperature, UHV surface science approach described above and used extensively throughout this thesis has previously been used to study the low energy electron-induced decomposition of several common FEBID precursors, including $MeCpPtMe_3$, $Pt(PF_3)_4$, $W(CO)_6$, and $Co(CO)_3NO$.[39–43] Many of these precursors, which were initially used in CVD, have also found use in FIBID; however, this surface science approach has not been previously used to study the low energy ion-induced decomposition of such a common precursor. Because of this, the low energy electron- and ion-induced decomposition of surface-adsorbed $Fe(CO)_5$, a common FEBID precursor, was studied in order to elucidate the molecular-level reactions that lead to deposition in FEBID and FIBID using $Fe(CO)_5$. The kinetics of low energy electron-induced deposition of adsorbed $Fe(CO)_5$ were also studied, showing the fundamental reactions that lead to iron and iron oxide deposition from $Fe(CO)_5$ using FEBID. Additionally, deposits were made from $Fe(CO)_5$ using ion beam induced deposition (IBID) in a UHV chamber, showing that pure iron deposits may be made with low energy IBID using $Fe(CO)_5$.

In chapter 2 of this thesis, I give a detailed theoretical overview of the fundamental electron- and ion-molecule interactions relevant to FEBID and FIBID and describe the experimental methods and instrumentation used at Johns Hopkins University to perform the UHV surface science experiments and deposition experiments described in this work. In chapters 3-5, I give

an overview of the experimental results obtained in the previously described studies on $CpFe(CO)_2Re(CO)_5$, $Ru(CO)_4I_2$, and $Fe(CO)_5$. In chapter 3, I discuss the effects of low energy electron and argon ion exposure on adsorbed thin films of $CpFe(CO)_2Re(CO)_5$. In chapter 4, I discuss gas phase low energy electron-induced reactions with $Ru(CO)_4I_2$ and compare them to studies of low energy electron and Ar^+-induced decomposition of physisorbed films of $Ru(CO)_4I_2$ and electron beam induced deposition (EBID) experiments with $Ru(CO)_4I_2$ performed in a UHV chamber. In chapter 5, I discuss studies performed on the low energy electron- and ion-induced decomposition of adsorbed films of $Fe(CO)5$ and compare them to deposits produced by ion beam induced deposition (IBID) from $Fe(CO)_5$ performed in a UHV chamber.

References

[1] G. E. Moore, *Electronics* **1965**, *38*, 114–117.

[2] G. E. Moore, *International Electron Devices Meeting IEEE* **1975**, 11–13.

[3] M. Kanellos, Moore's Law to roll on for another decade, **2003**.

[4] R. Courtland, Intel Now Packs 100 Million Transistors in Each Square Millimeter, **2017**.

[5] K. M. McPeak, S. V. Jayanti, S. J. P. Kress, S. Meyer, S. Iotti, A. Rossinelli, D. J. Norris, *ACS Photonics* **2015**, *2*, 326–333.

[6] M. I. Stockman, K. Kneipp, S. I. Bozhevolnyi, S. Saha, A. Dutta, J. Ndukaife, N. Kinsey, H. Reddy, U. Guler, V. M. Shalaev, A. Boltasseva, B. Gholipour, H. N. S. Krishnamoorthy, K. F. MacDonald, C. Soci, N. I. Zheludev, V. Savinov, R. Singh, P. Groß, C. Lienau, M. Vadai, M. L. Solomon, D. R. Barton, M. Lawrence, J. A. Dionne, S. V. Boriskina, R. Esteban, J. Aizpurua, X. Zhang, S. Yang, D. Wang, W. Wang, T. W. Odom, N. Accanto, P. M. de Roque, I. M. Hancu, L. Piatkowski, N. F. van Hulst, M. F. Kling, *Journal of Optics* **2018**, *20*, 043001.

[7] N. C. Lindquist, P. Nagpal, K. M. McPeak, D. J. Norris, S.-H. Oh, *Reports on Progress in Physics* **2012**, *75*, 036501.

[8] E. Ozbay, *Science* **2006**, *311*, 189–193.

[9] R. Zia, J. A. Schuller, A. Chandran, M. L. Brongersma, *Materials Today* **2006**, *9*, 20–27.

[10] M. M. Shawrav, D. Belic, M. Gavagnin, S. Wachter, M. Schinnerl, H. D. Wanzenboeck, E. Bertagnolli, *Chemical Vapor Deposition* **2014**, *20*, 251–257.

[11] M. Gabureac, L. Bernau, I. Utke, G. Boero, *Nanotechnology* **2010**, *21*, 115503.

[12] I. Utke, P. Hoffmann, J. Melngailis, *Journal of Vacuum Science & Technology B: Microelectronics and Nanometer Structures* **2008**, *26*, 1197.

[13] W. F. van Dorp, C. W. Hagen, *Journal of Applied Physics* **2008**, *104*, 081301.

[14] M. Huth, F. Porrati, C. Schwalb, M. Winhold, R. Sachser, M. Dukic, J. Adams, G. Fantner, *Beilstein Journal of Nanotechnology* **2012**, *3*, 597–619.

[15] T. Liang, G. Zhang, P. Naulleau, A. Myers, S.-J. Park, A. Stivers, G. Vandentop in, *Vol. 6283*, (Ed.: M. Hoga), International Society for Optics and Photonics, **2006**, 62830K.

[16] T. Liang, A. Stivers, R. Livengood, P.-Y. Yan, G. Zhang, F.-C. Lo, *Journal of Vacuum Science & Technology B: Microelectronics and Nanometer Structures* **2000**, *18*, 3216.

[17] ZEISS International, MeRiT® neXT.

[18] nanotools GmbH, EAR - nanotools AFM probes.

[19] nanotools GmbH, biosphere™ - nanotools AFM probes.

[20] M. Huth, F. Porrati, O. Dobrovolskiy, *Microelectronic Engineering* **2018**, *185-186*, 9–28.

[21] J. M. De Teresa, R. Córdoba, A. Fernández-Pacheco, O. Montero, P. Strichovanec, M. R. Ibarra, *Journal of Nanomaterials* **2009**, *2009*, 936863.

[22] C. A. Sanford, L. Stern, L. Barriss, L. Farkas, M. DiManna, R. Mello, D. J. Maas, P. F. A. Alkemade, *Journal of Vacuum Science & Technology B: Microelectronics and Nanometer Structures* **2009**, *27*, 2660.

[23] A Botman, J. J. L. Mulders, C. W. Hagen, *Nanotechnology* **2009**, *20*, 372001.

[24] G. Gazzadi, J. Mulders, P. Trompenaars, A. Ghirri, A. Rota, M. Affronte, S. Frabboni, *Microelectronic Engineering* **2011**, *88*, 1955–1958.

[25] J.-Y. Fang, S.-Q. Qin, X.-A. Zhang, D.-Q. Liu, S.-L. Chang, *Chinese Physics B* **2014**, *23*, 088111.

[26] M Komuro, H Hiroshima, A Takechi, *Nanotechnology* **1998**, *9*, 104–107.

[27] J. Jurczyk, C. R. Brewer, O. M. Hawkins, M. N. Polyakov, C. Kapusta, L. McElwee-White, I. Utke, *ACS Applied Materials & Interfaces* **2019**, *11*, 28164–28171.

[28] J. A. Spencer, M. Barclay, M. J. Gallagher, R. Winkler, I. Unlu, Y.-C. Wu, H. Plank, L. McElwee-White, D. H. Fairbrother, *Beilstein Journal of Nanotechnology* **2017**, *8*, 2410–2424.

[29] D. Belić, M. M. Shawrav, E. Bertagnolli, H. D. Wanzenboeck, *Beilstein J. Nanotechnol* **2017**, *8*, 2530–2543.

[30] M. J. Perez-Roldan, F Tatti, P Vavassori, A Berger, A Chuvilin, *Nanotechnology* **2015**, *26*, 375302.

[31] S. Wang, Y.-M. Sun, Q. Wang, J. M. White, *Journal of Vacuum Science & Technology B: Microelectronics and Nanometer Structures* **2004**, *22*, 1803.

[32] M. M. Shawrav, P. Taus, H. D. Wanzenboeck, M. Schinnerl, M. Stöger-Pollach, S. Schwarz, A. Steiger-Thirsfeld, E. Bertagnolli, *Scientific Reports* **2016**, *6*, 34003.

[33] I. Utke, P. Hoffmann, B. Dwir, K. Leifer, E. Kapon, P. Doppelt, *Journal of Vacuum Science & Technology B: Microelectronics and Nanometer Structures* **2000**, *18*, 3168.

[34] J. J. L. Mulders, J. M. Veerhoek, E. G. T. Bosch, P. H. F. Trompenaars, *Journal of Physics D: Applied Physics* **2012**, *45*, 475301.

[35] W. F. van Dorp, X. Wu, J. J. L. Mulders, S. Harder, P. Rudolf, J. T. M. De Hosson, *Langmuir* **2014**, *30*, 12097–12105.

[36] J. A. Spencer, Y.-C. Wu, L. McElwee-White, D. H. Fairbrother, *Journal of the American Chemical Society* **2016**, *138*, 9172–9182.

[37] R. M. Thorman, R. K. T. P., D. H. Fairbrother, O. Ingólfsson, *Beilstein Journal of Nanotechnology* **2015**, *6*, 1904–1926.

[38] R. M. Thorman, S. J. Matsuda, L. McElwee-White, D. H. Fairbrother, *The Journal of Physical Chemistry Letters* **2020**, *11*, 2006–2013.

[39] W. F. van Dorp, J. D. Wnuk, J. M. Gorham, D. H. Fairbrother, T. E. Madey, C. W. Hagen, *Journal of Applied Physics* **2009**, *106*, 074903.

[40] J. D. Wnuk, J. M. Gorham, S. G. Rosenberg, W. F. van Dorp, T. E. Madey, C. W. Hagen, D. H. Fairbrother, *The Journal of Physical Chemistry C* **2009**, *113*, 2487–2496.

[41] K. Landheer, S. G. Rosenberg, L. Bernau, P. Swiderek, I. Utke, C. W. Hagen, D. H. Fairbrother, *The Journal of Physical Chemistry C* **2011**, *115*, 17452–17463.

[42] S. G. Rosenberg, M. Barclay, D. H. Fairbrother, *The Journal of Physical Chemistry C* **2013**, *117*, 16053–16064.

[43] S. G. Rosenberg, M. Barclay, D. H. Fairbrother, *Physical Chemistry Chemical Physics* **2013**, *15*, 4002–4015.

Chapter 2

Theoretical overview and experimental methods

2.1 Theoretical overview

The fundamental concept of both FEBID and FIBID is fairly simple – an organometallic precursor molecule is introduced via a gas inlet system into a high vacuum chamber equipped with a high energy (1 – 30 kV) electron or ion beam and containing a substrate.[1–3] The precursor gas is allowed to physisorb onto the substrate, which is then impacted by the high energy charged particle beam. Ideally, electron- or ion-driven reactions cause the organometallic precursor to fully decompose under the area of the charged particle beam, causing the desired metal to deposit onto the surface and the organic ligands to desorb from the surface into the vacuum. This is not necessarily the result of *in situ* FEBID and FIBID experiments, which commonly produce deposits with significant organic contamination. In order to improve the quality of nanostructures fabricated by FEBID and FIBID, it is thus important to understand the low energy electron- and ion-driven

reactions that underly the deposition processes. The first part of this chapter will discuss the fundamental interactions leading to deposition in FEBID and FIBID.

2.1.1 Fundamental interactions in FEBID

Interactions of low energy electrons (LEEs) with organometallic precursor molecules have an important role in FEBID, in which low energy electrons are abundant.[4, 5] Due to the impact of the primary electron beam, secondary electrons are emitted from the surface, as will be discussed in the following section. Currently, it is generally well accepted that these secondary electrons, defined here as electrons with energies < 50 eV, initiate precursor decomposition reactions that constitute the initial deposition step in FEBID. These low energy electron-induced decomposition reactions, which will be discussed in detail in this chapter, are known to initiate incomplete ligand dissociation reactions with organometallic precursor molecules. They are thus likely to contribute to adverse effects associated with FEBID, such as poor deposit purity due to co-deposition of ligands and ligand fragments from the organometallic precursor molecules. Understanding the low energy electron-induced decomposition of FEBID precursor molecules is thus vital to improving the quality of FEBID nanostructures.

2.1.1.1 Electron beam interactions with surfaces

In FEBID, a high energy electron beam impacts a substrate, causing the electrons to undergo both elastic and inelastic scattering. This produces a broad
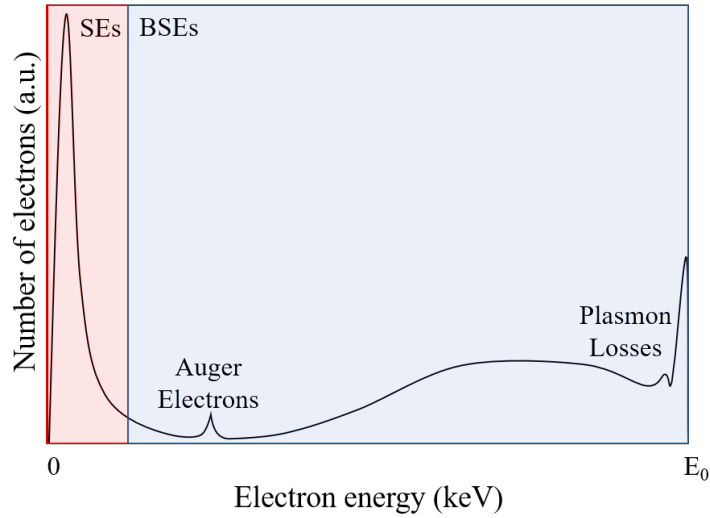
Figure 2.1: Schematic of a hypothetical electron energy distribution of a surface irradiated with an electron beam of energy E_0. Adapted with permission from [6].

energetic profile of electrons at a surface impacted by a high energy electron beam, including both low energy secondary electrons (SEs, commonly defined as having energies < 50 eV) and higher energy backscattered electrons (BSEs, commonly defined as having energies > 50 eV). Irradiation of a surface with a high energy electron beam may also produce electrons via excitation processes, such as Auger electrons. A schematic of a typical energy profile of electrons emitted from a substrate impacted by a high energy primary electron beam of energy E_0 is shown in Figure 2.1. As depicted in this typical energy profile, the majority of electrons emitted from the surface are SEs, with the electron energy distribution commonly peaking well below 10 eV for most surfaces. The remaining electrons emitted by the surface are largely BSEs. A relatively small contribution to the electron energy spectrum comes from Auger electrons. When a core electron is ejected from an atom by energy

15

transfer from the primary electron beam, a photon may be emitted when an outer shell electron drops down to replace it. This photon may in turn excite another electron in the atom, causing it to be emitted with a kinetic energy characteristic of the Auger transition, producing a well-defined peak in the electron energy spectrum, as seen in Fig. 2.1. Additional peaks are seen at energies close to that of the primary electron beam (E_0), which are caused by surface plasmon losses and are common in metals. The highest energy peak seen in the electron energy distribution is at E_0, which is the elastically scattered electron peak.

While the general shape of the energy distribution of electrons emitted from a surface bombarded with a high energy electron beam is similar for most surfaces, the exact distribution is dependent on surface composition. Figure 2.2 shows the energy distribution of secondary electrons emitted from Ni (111) (black solid line) and Ag (100) (red dotted line) overlaid with the typical energy regimes for the low energy electron-induced decomposition reactions generally understood to initiate deposition in FEBID.[5] These reactions will be discussed in detail in the following section. Ultimately, the composition of the deposited nanostructure will be reflective of a convolution of the SEs available at the surface to initiate these reactions and the cross sections for the individual reactions at the energies of the available SEs.

2.1.1.2 Electron interactions with precursor molecules

Electron-induced fragmentation of molecules at low incident electron energies is known to proceed through four processes shown in Equations 2.1 – 2.4:
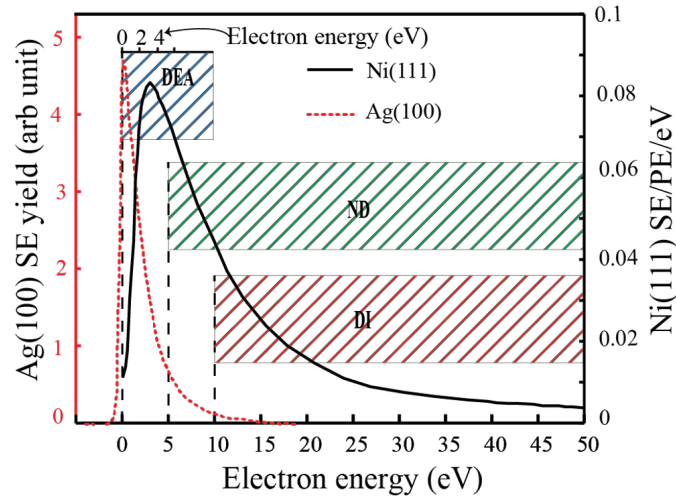
Figure 2.2: Electron energy distributions of Ni(111) (black solid line) and Ag(100) (red dotted line) shown with typical energy regimes for electron-induced decomposition reactions in FEBID. Reproduced with permission from Thorman et al.[5]

---

dissociative electron attachment (DEA, Eq. 2.1), dissociative ionization (DI, Eq. 2.2), neutral dissociation (ND, Eq. 2.3), and dipolar dissociation (DD, Eq. 2.4).[4, 5, 7]

$$AB + e^- \rightarrow [AB]^{(\ddagger)-} \rightarrow A^{(\ddagger)} + B^{(\ddagger)-} \tag{2.1}$$

$$AB + e^- \rightarrow [AB]^{(\ddagger)+} + 2e^- \rightarrow A^{(\ddagger)+} + B^{(\ddagger)} + 2e^- \tag{2.2}$$

$$AB + e^-(\epsilon_1) \rightarrow [AB]^* + e^-(\epsilon_2 < \epsilon_1) \rightarrow A^{(\ddagger)} + B^{(\ddagger)} + e^-(\epsilon_2 < \epsilon_1) \tag{2.3}$$

$$AB + e^-(\epsilon_1) \rightarrow [AB]^* + e^-(\epsilon_2 < \epsilon_1) \rightarrow A^{(\ddagger)+} + B^{(\ddagger)-} + e^-(\epsilon_2 < \epsilon_1) \tag{2.4}$$
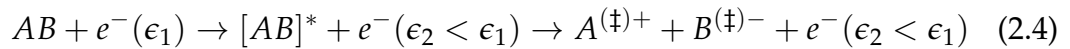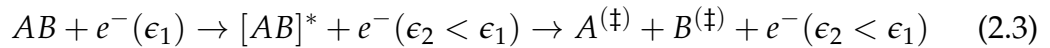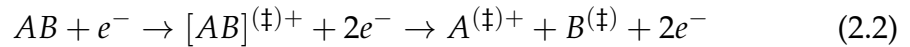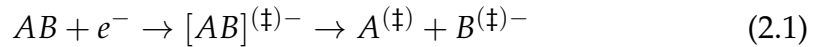
Here, ‡ symbolizes the potential for the parent ion or fragment(s) to be

in electronically and/or vibrationally excited states, while * represents the electronic excitation of the parent molecule, which then leads to ND or DD (Eq. 2.3 and 2.4, respectively). The symbols ϵ_1 and ϵ_2 represent the energy of the incident electron before (ϵ_1) and after (ϵ_2) the inelastic scattering event that electronically excites the parent molecule.

Precursor decomposition initiated by DEA (Eq. 2.1) has been hypothesized for several FEBID precursors (e.g., MeCpPtMe$_3$, Pt(PF$_3$)$_4$),[8–12] generally associated with single ligand loss. In FEBID, DI-induced precursor dissociation (Eq. 2.2) is commonly associated with multiple ligand loss and has been implicated in the initial decomposition/deposition of FEBID precursors (e.g. W(CO)$_6$).[13, 14] While the extent of ligand desorption is typically greater for DI, neither DEA or DI leads to the complete loss of all ligands associated with the precursor. Thus, the LEE-initiated deposition step in FEBID can best be characterized by a degree of ligand loss and the formation of a surface-bound intermediate that contains the metal atom and those residual ligands which did not desorb.[12, 14–20]

After the initial electron-induced deposition step, ultra-high vacuum (UHV) surface science studies have shown that further electron irradiation most often leads to decomposition of the residual ligands rather than further ligand desorption. As an illustrative example, Rosenberg et al. found that electron-induced deposition from W(CO)$_6$ proceeds through an initial step in which about 2 – 3 CO ligands desorb from the surface, and a second step in which the remaining CO ligands decompose into adsorbed carbon and reactive oxygen species which oxidize the deposited tungsten atoms.[14] This

electron-induced reaction scheme is common to many carbonyl-containing organometallic precursors, including $Co(CO)_3NO$, $HFeCo_3(CO)_{12}$, and $(\eta^5\text{-}Cp)Fe(CO)_2Mn(CO)_5$.[17–19] The second step is thus typically responsible for any oxidation of the metal atoms in the deposit and is principally responsible for incorporation of the unwanted organic contamination into the final deposit. This type of fundamental understanding has led to the development of new FEBID precursors, including $Pt(CO)_2Cl_2$,[16, 21] underscoring the importance of elucidating the LEE-induced reactions that underpin deposition processes.[1, 2, 5]

As both DEA and DI (Eq. 2.1 and 2.2, respectively) have been found to be important initial steps in FEBID, descriptions of these two processes will thus be given in the following sections due to their fundamental importance in FEBID. Briefer descriptions will then be given for ND and DD (Eq. 2.3 and 2.4, respectively).

Dissociative electron attachment

Dissociative electron attachment (Eq. 2.1) is a resonant process that commonly occurs at the lowest incident electron energies (< 15 eV). The process is shown graphically in Figure 2.3, with potential energy surfaces for the ground state of parent molecule AB, the ground state of the parent anion AB^-, and an excited antibonding state of the parent anion AB^{*-}. As can be seen in both Eq. 2.1 and Fig. 2.3, the first step in DEA is electron capture (EC in Fig. 2.3), forming a transient negative ion (TNI, $AB^{(\ddagger)-}$ in Eq. 2.1 and also called a resonance). The cross section for EC (σ_{EC} in Fig. 2.3) is highest at 0 eV incident electron
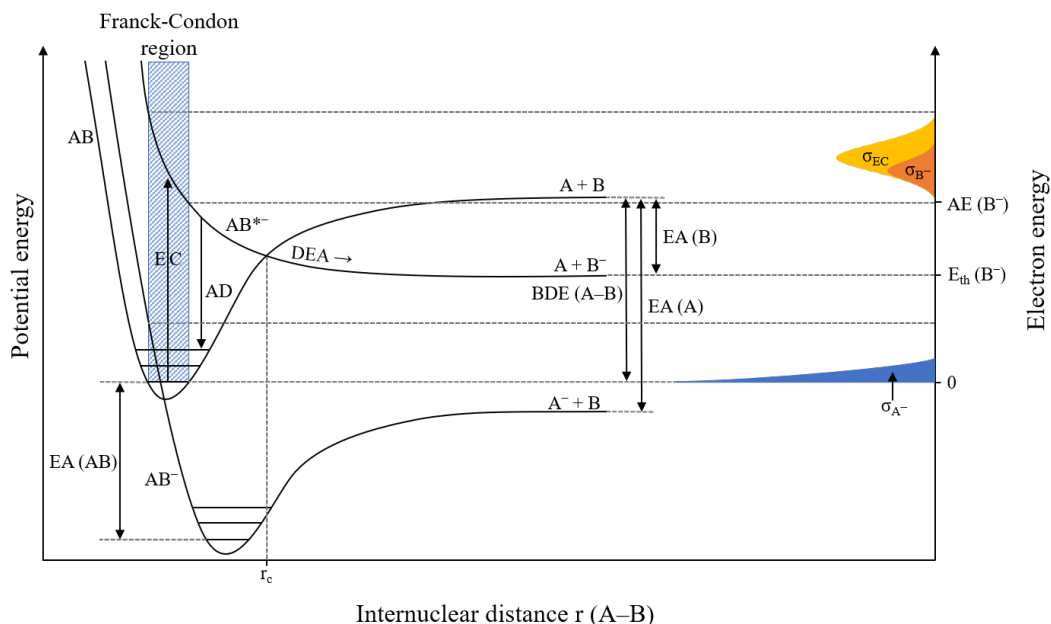
Figure 2.3: Depiction of dissociative electron attachment to a diatomic molecule AB. Adapted with permission from [6].

energy, and cross sections for DEA are thus typically highest close to 0 eV. The Franck-Condon principle states that nuclear motion is much slower than electronic transitions, leading EC to be seen as a vertical transition between the ground state of the parent molecule (AB in Fig. 2.3) and either the ground state of the parent anion (AB$^-$ in Fig. 2.3) or an excited state of the parent anion (AB^{*-} in Fig. 2.3) within the Franck-Condon region of overlap (shown as a blue cross-hatched box in Fig. 2.3).

Once formed, a TNI is commonly in a vibrationally and/or electronically excited state and will necessarily redistribute its excess energy through relaxation. The two major channels of relaxation are autodetachment (AD) and dissociation (DEA), both of which are shown graphically in Fig. 2.3. If an

electron is captured into an antibonding excited state AB^{*-}, as depicted in Fig. 2.3, the excess energy can be redistributed into kinetic energy of the A and B nuclei, causing the internuclear distance r(A-B) to lengthen. As r(A-B) lengthens, the TNI AB^{*-} may relax by emitting an electron (AD), producing a free electron and the parent molecule, which may be in a vibrationally and/or electronically excited state. This is the most dominant relaxation channel. Due to the potential for autodetachment, the energetic width (Γ) of the TNI is finite, with a lifetime (τ_{AD}) that can be derived from the Heisenberg uncertainty principle:

$$\tau_{AD} \sim \frac{\hbar}{\Gamma} \tag{2.5}$$

Here, $\hbar$ is the reduced Planck constant. As can be seen in Eq. 2.5, TNIs with long lifetimes (i.e., large τ_{AD}) will have correspondingly narrow energy ranges (i.e., small Γ), while TNIs with short lifetimes will have broad energy ranges.

Alternately, if r(A-B) lengthens past the point of overlap between the ground state AB and antibonding excited state AB^{*-} (the critical internuclear distance, marked in Fig. 2.5 as r_c), the TNI can only relax by dissociation (DEA). Figure 2.3 illustrates one example of this, showing electron capture from the ground state of AB into the excited anionic state AB^{*-}, dissociating to produce neutral fragment A and anionic fragment B^-. The cross section for the formation of B^- via DEA (σ_{B-}), shown graphically in Fig. 2.3, can be

given as:

$$\sigma_{DEA} \sim \sigma_{EC} \times e^{-\left(\frac{t}{\tau_{AD}}\right)} \quad (2.6)$$

The cross section for anionic fragment formation via DEA is thus dependent on both the cross section for electron capture (σ_{EC}) and the probability of the TNI surviving past the critical internuclear distance r_c, which is itself dependent on the TNI lifetime with respect to AD (Γ_{AD}) and the time required for the TNI to pass r_c (t_c). As can be seen in Fig. 2.3, the cross section for the formation of B$^-$ is a subset of the total cross section for electron capture. Due to the higher probability of AD at higher electron capture energies, σ_{B^-} drops off more rapidly than σ_{EC} at higher energies.

The threshold for the formation of an anion through DEA can also be derived from the potential energy curves shown in Fig. 2.3. Taking the formation of B$^-$ again as an illustrative example, the threshold for this reaction ($E_{th}(B^-)$) can be given as:

$$E_{th}(B^-) = BDE(A - B) - EA(B) \quad (2.7)$$

Here, BDE(A–B) is the bond dissociation energy (BDE) of bond A–B, and EA(B) is the electron affinity (EA) of B. For polyatomic parent molecules, which may produce fragments through multiple bond ruptures, Eq. 2.7 can be generalized such that the threshold is given by the sum of the BDEs of all bonds broken less the EA of the electron-retaining fragment. While this reaction energy defines the energetic threshold of B$^-$ formation, as can be seen

in Fig. 2.3, the appearance energy (AE) of anionic fragments is commonly above the threshold energy for their formation. As electron capture must occur within the Franck-Condon region of overlap, TNIs may be formed substantially above their threshold energy:

$$AE(B^-) = E_{th} + E^* = BDE(A - B) - EA(B) + E^* \qquad (2.8)$$

The appearance energy of an anionic fragment is thus equal to the threshold energy and an additional quantity of excess energy (E^*), which may manifest as kinetic energy or electronic or vibrational excitation of the product fragments.

Dissociative ionization

Dissociative ionization (Eq. 2.2), which is shown graphically in Figure 2.4, is a non-resonant process that occurs at or above the ionization energy (IE) of the respective parent molecule. This places the typical energetic threshold for DI processes at or above 10 eV. As can be seen in both Fig. 2.4 and Eq.2.2, electron impact ionizes the parent molecule, producing the parent cation in either its ground state or an electronically or vibrationally excited state. Similarly to TNI formation, this may be seen as a vertical transition from the ground state of the parent molecule to the respective state of the cation within the Franck-Condon region of overlap. The parent cation may then dissociate into a cationic fragment and one or more neutral fragments, as seen in Fig. 2.4 and Eq. 2.2.
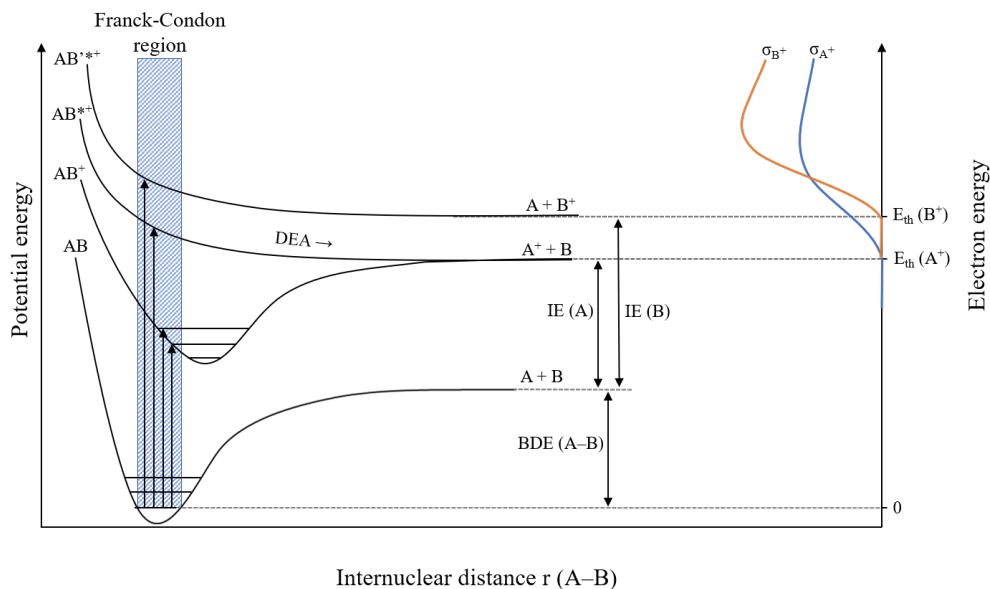
Figure 2.4: Depiction of dissociative ionizaton of to a diatomic molecule AB.

Unlike TNI formation, electron impact ionization is not a reversible reaction and the lifetime of the parent cation is thus not limited in this manner. Additionally, at the significantly higher energies of ionization, a continuum of excited states may be formed, causing electron impact ionization (and, subsequently, DI) to exhibit threshold behavior rather than resonant behavior. Taking the formation of A^+ from parent molecule AB as an illustrative example, as seen in Fig. 2.4, the threshold for this reaction ($E_{th}(A^+)$) can be given as:

$$E_{th}(A^+) = BDE(A - B) + IE(A) \qquad (2.9)$$

For polyatomic parent molecules, as for DEA, Eq. 2.9 can be generalized such that the thermodynamic threshold is equal to the sum of the BDEs of

all ruptured bonds and the IE of the cationic fragment. The cross sections for cationic fragment formation through DI, as shown in Fig. 2.4 (e.g. σ_{A^+}), increase from the thermodynamic threshold, reaching a maximum between 50 and 100 eV and then decreasing due to the decrease in the cross section for electron scattering. As the energy of the ionizing electron increases, multiple bond ruptures are favored, producing increasingly extensive fragmentation patterns. Due to its higher energetic threshold and broader energy range, DI generally produces significantly more fragmentation of the parent molecule than DEA.

Neutral dissociation and dipolar dissociation

Neutral dissociation (Eq. 2.3) and dipolar dissociation (Eq. 2.4) are both non-resonant processes that are initiated by an inelastic electron scattering event, which electronically excites the parent molecule. In ND, the electronically excited parent molecule then dissociates into two or more neutral fragments, which may be in electronically or vibrationally excited states. The thermodynamic threshold for ND is given simply by the BDEs of any bonds ruptured, which is generally within the energy range of the lowest electronic transitions in the parent molecule. The absence of ionic products makes ND more difficult to measure than DEA, DI, or DD; however, several recent studies of FEBID precursor molecules have combined experimentally determined electronic excitation cross sections with density functional theory (DFT) calculations in order to predict the relative importance of ND in FEBID.[22–24] Based on these studies, it is possible that ND is even more important to FEBID than DEA, which is considered a dominant process.

In DD, the electronically excited parent molecule dissociates into an anionic fragment and a cationic fragment, both of which may be produced in electronically or vibrationally excited states. The thermodynamic threshold for DD is given by the sum of the BDEs of any bonds ruptured and the IE of the cationic fragment, less the EA of the anionic fragment, and additional energy is necessary to overcome the coulombic attraction between the two fragments. Because of this additional energy requirement, DD is likely less efficient than ND.

2.1.2   Fundamental interactions in FIBID

In contrast to FEBID, far fewer insights exist on the fundamental bond-breaking processes involved in FIBID. This is in part because a number of different processes can contribute to the initial deposition step in FIBID, making it correspondingly more complex to understand.[1, 25–27] Contributions may come from secondary electrons, as in FEBID, as well as primary and scattered ions, sputtered atoms, and localized heating. There are three main candidates for the dominant deposition mechanism in FIBID: (i) the secondary electron model, which proceeds similarly to the model previously described for FEBID (Section 2.1.1); (ii) the collision cascade model, wherein energy transfer from the incident ions to the surface atoms via a cascade of atom-atom collisions leads to the decomposition of transiently adsorbed precursor molecules by energetic surface atoms;[25] and (iii) the thermal spike model, where energy transfer from the incident ions to the substrate (and subsequently the adsorbed precursor molecules) causes a localized temperature

spike in the near surface regions, which is responsible for precursor decomposition.[25] As the thermal spike model is less relevant to the subject matter of this dissertation, it will not be thoroughly discussed here. In this section, the collision cascade model will be reviewed and several FIBID studies that have aimed to elucidate whether the secondary electron model or the collision cascade model is most important will be discussed.

2.1.2.1 Collision cascade model

High energy ions incident on a surface can transfer a significant amount of energy via collision. Due to the low residence time of precursor molecules on a substrate within the area of the primary ion beam during FIBID, direct collisions between a high energy ion and a precursor molecule can be assumed to be rare. Instead, the energy is transferred to the substrate atoms by high energy ion impact, which can then transfer energy between substrate atoms in a cascade of substrate atom collisions, as shown in Figure 2.5. This "collision cascade" can produce excited surface atoms (ESAs), which then interact with transiently adsorbed precursor molecules, causing precursor decomposition and deposition. The interaction between ESAs and precursor molecules can be modelled as a head-on binary collision between an ESA and a transiently adsorbed precursor molecule, and thus this model is also sometimes called the binary collision model. In this model, the maximum energy that can be transferred between the two (E_{max}) can be given as:

$$E_{max} = 4E_{ESA}\frac{m_{ESA} \times m_p}{(m_{ESA} + m_p)^2} \tag{2.10}$$
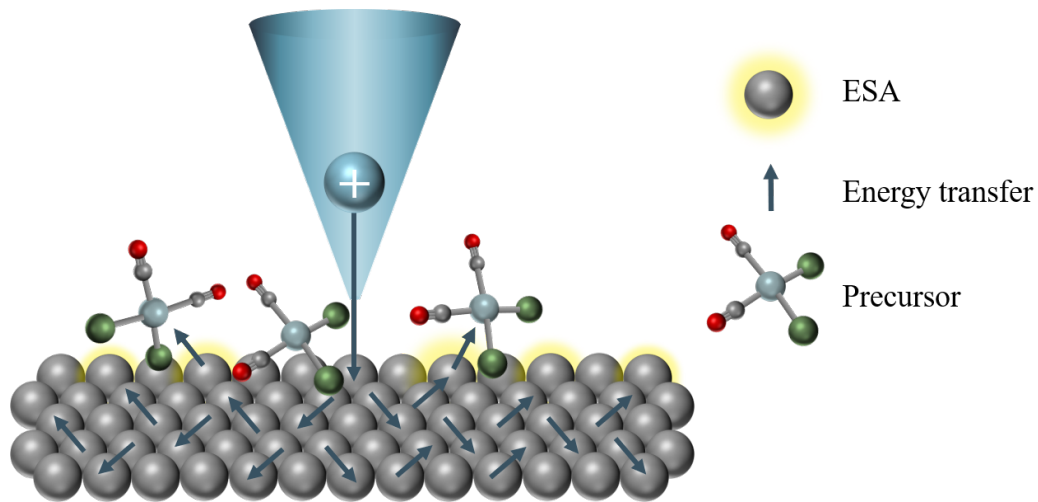
Figure 2.5: Depiction of the collision cascade model in FIBID.

Here, E_{ESA} is the energy of the excited surface atom, m_{ESA} is the mass of the ESA, and m_p is the mass of the precursor molecule. The energy transfer between the high energy ion beam and the precursor molecule will thus be mediated by the surface, and the total energy imparted to the precursor molecule will be relatively low when compared to the energy of the primary ions, particularly given that high energy ESAs are likely to be sputtered before interacting with a precursor molecule. Ultimately, the composition of a FIBID deposit according to this model will be a convolution of the energy distribution of ESAs and the cross sections for precursor decomposition at those energies.

2.1.2.2 Secondary electron vs. collision cascade model

Several previous FIBID studies have endeavored to elucidate which processes are most important by correlating macroscopic measurements of growth rates

with various deposition parameters. Several studies support the collision cas-cade model. For example, Dubner et al. and Ro et al. showed that deposition rates for gold deposited from dimethylgold(hfac) using 2 − 10 kV[25] and 50 − 100 kV[28] ion beams of Ne^+, Ar^+, Kr^+, and Xe^+, correlated well with nuclear stopping power but not with electronic stopping power. In contrast, other studies support the secondary electron model of deposition. Lipp et al. reported a linear relationship between secondary electron yield during ion beam milling and deposition yield when using 5 − 30 kV Ga^+ ion beams to deposit platinum from $CpPtMe_3$ onto silicon, supporting the secondary electron model.[29]

The complexity of FIBID is perhaps best illustrated by different deposition mechanisms invoked by the same research team to explain FIBID performed under different conditions. During deposition from $MeCpPtMe_3$ onto a silicon substrate with and without a 30 nm Cu coating using 5 − 30 kV Ga^+ ion beams, Chen et al. found that the deposition yield and secondary electron yield had very different energy dependences.[26] The deposition yield was found to be linearly related to the sputtering yield, supporting the collision-induced deposition model. However, the same research group used a He^+ beam to deposit platinum nanopillars from $MeCpPtMe_3$ onto a silicon substrate and found that the deposition yield was similar to that from Ga^+, despite the nuclear stopping power of He^+ and Ga^+ differing by about two orders of magnitude.[30] This led the authors to conclude that for He-FIBID, electronic excitation was the likely deposition mechanism. At this point, a more detailed

understanding of ion beam reactions with organometallic precursors is necessary in order to improve our understanding of FIBID and its relationship (if any) to FEBID.

2.1.2.3 Regimes in FEBID and FIBID

As deposit formation in both FEBID and FIBID is precipitated by the interaction of a charged particle (electron or ion) with a precursor molecule (albeit potentially mediated by the surface in FIBID), each of these must be present for deposition to occur. Thus, dependent on the charge density and flux of precursor molecules on the substrate, deposition may be limited by the number of charged particles available to initiate deposition (i.e., there exists an excess of precursor molecules) or by the number of precursor molecules available to be decomposed and subsequently deposited (i.e., there exists an excess of charged particles). These regimes of deposition are defined as the electron- or ion-limited process regime and the precursor-limited process regime, respectively. These two different regimes are associated with different growth characteristics and deposit shapes; additionally, the precursor-limited regime in FIBID may be associated with excess sputtering in the center of the deposit with higher ion fluxes. A more detailed discussion of the characteristics of these regimes may be found in the literature.[1, 31]

2.2 Experimental Methods

Three different types of experiments are reported in this thesis: (i) electron and argon ion irradiation of adsorbed thin films of organometallic molecules,

(ii) *in situ* electron- and ion-beam induced deposition (EBID and IBID, respectively) of organometallic molecules in UHV instruments, and (iii) gas phase measurements of low energy electron-induced decomposition of an organometallic molecule under single collision conditions. The experimental setup used for the gas phase measurements are given in detail elsewhere.[32] This section will focus on the experimental setup used to perform and analyze the experiments performed on the adsorbed thin films and deposits, as well as the analytical techniques used.

2.2.1 Surface analytical methods

The experiments described in the following chapters predominantly utilized four analytical techniques: mass spectrometry (MS), which is a gas phase analytical technique, and X-ray photoelectron spectroscopy (XPS), scanning electron microscopy (SEM), and energy-dispersive X-ray spectroscopy (EDX), each of which are techniques that analyze surfaces. A general overview of the surface analytical techniques (XPS, SEM, and EDX) will be given in this section.

2.2.1.1 X-ray Photoelectron Spectroscopy (XPS)

X-ray photoelectron spectroscopy is a surface-sensitive, UHV analytical technique that utilizes the photoelectric effect to characterize the elemental composition of a surface, as well as the bonding environment of surface species. Figure 2.6 shows a schematic of the photoionization process used in XPS, wherein an X-ray (in this work, Mg Kα = 1254 eV) excites a core level electron,
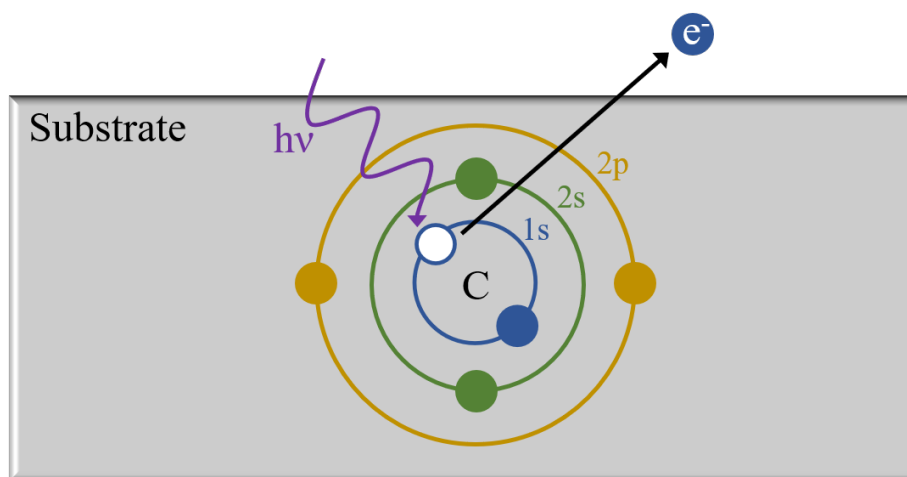
Figure 2.6: Schematic of the photoionization of a surface carbon atom in XPS.

causing it to be ejected from the surface. The ejected electron, called a photo-electron, is ejected with a kinetic energy characteristic of its respective element and orbital, as well as the energy of the incident photon. Photoelectrons may then be detected as a function of their kinetic energy by a hemispherical analyzer, and the binding energy (BE) of the detected photoelectrons may be determined by:

$$BE = h\nu - KE - \phi_s \qquad (2.11)$$

Here, $h\nu$ is the energy of the incident photon, KE is the measured kinetic energy of the emitted photoelectron, and ϕ_s is the work function of the spectrometer. The BE of the ejected photoelectron is dependent on the specific element and orbital from which it originates, as well as the bonding environment of its respective element. Due to their lack of core electrons, hydrogen
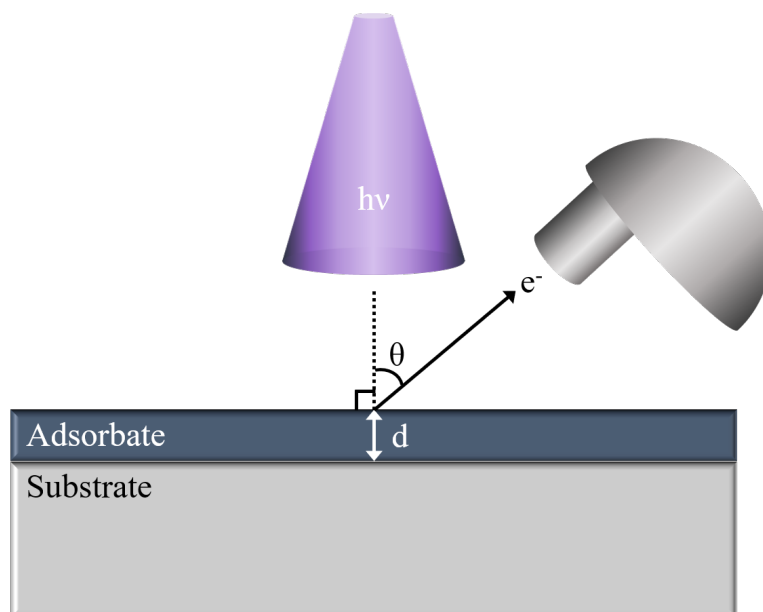
Figure 2.7: Schematic detailing the measurement of adsorbate thickness XPS.

and helium may not be detected using XPS. Typically, a photoelectron origi-
nating from an element that is bound to a species that is more electronegative,
or electron-withdrawing, will have a higher BE, while a photoelectron orig-
inating from an element bound to a species that is less electronegative, or
electron-donating, will have a lower BE.

Photoelectrons will only retain their characteristic BE if they do not ex-
perience significant inelastic collisions, which cause them to lose energy. As
electrons generally have a small inelastic mean free path (IMFP, λ) – electrons
originating from the Au (4f) orbital typically have an IMFP of about 1.47 nm
- the utility of XPS is thus limited to characterizing species at the surface of
a sample (typically the top 10 nm), making it a highly surface sensitive tech-
nique. This can also be advantaged to determine the thickness of an adsorbate

on a substrate, as depicted in Figure 2.7. The presence of an adsorbate will cause the XPS peaks associated with the substrate to attenuate, the quantity of which is dependent on the thickness of the adsorbate. The film thickness may thus be measured by taking XPS spectra of the substrate with and without the adsorbate via an application of Beer's Law, giving the equation:

$$d = \ln \frac{[I_s]_a}{[I_s]_0} \cdot \lambda \cos \theta \qquad (2.12)$$

Here, d is the film thickness, $[I_s]_a$ is the intensity of the substrate peaks with the adsorbate present, $[I_s]_0$ is the intensity of the substrate peaks with no adsorbate present, λ is the IMFP of the photoelectrons at the KE associated with the specific substrate peaks, and θ is the angle between the detector (generally a hemispherical analyzer, as shown in Fig. 2.7) and the surface normal. In this thesis, the IMFP of the substrate photoelectrons was determined using the NIST Electron Inelastic Mean Free Path Database.[33]

2.2.1.2 Scanning Electron Microscopy (SEM) and Energy-Dispersive X-Ray Spectroscopy (EDX)

As discussed above, a high energy electron beam impacting a surface will produce a large number of secondary electrons and backscattered electrons through elastic and inelastic scattering events. Scanning electron microscopy (SEM) utilizes a tightly focused high energy primary electron beam to produce secondary electrons, which are then detected in order to image surfaces at exceedingly high magnifications with higher resolutions than are possible with optical microscopy. Resolution in a microscope is limited by the Abbe

diffraction limit:

$$d = \frac{\lambda}{2n \sin \theta} \approx \frac{\lambda}{2.8} \qquad (2.13)$$

Here, d is the diffraction limit, λ is the wavelength of the probe particle (e.g. the photon), and $n \sin \theta$ is the numerical aperture of the microscope. In optical systems, the numerical aperture is typically $1.4 - 1.6$. For visible light (λ = 390 - 700 nm), the diffraction limit is typically on the order of 140 - 250 nm. For electrons and other massive particles, the de Broglie wavelength is:

$$\lambda = \frac{h}{p} \qquad (2.14)$$

Here, h is the Planck constant and p is the momentum of the particle. A 10 kV beam of electrons has a de Broglie wavelength of 0.001 nm and thus an Abbe diffraction limit of 0.0036 nm. Thus, SEM has the potential for sub-nanometer resolution, although typical resolutions of commercial SEMs are on the order of 1 - 20 nm.

Secondary electrons, which have energies below about 50 eV, are used in SEM due to their high surface sensitivity. The universal curve of electron IMFPs shows that electrons with energies of 10 - 100 eV have the smallest IMFPs, making them the most surface sensitive. Thus, the use of SEs in imaging provides the most precise topographical information. Images produced using the higher energy BSEs can provide more information about subsurface features. Figure 2.8 gives a qualitative schematic of the relative escape depths of various signals produced by impacting a surface with a high energy
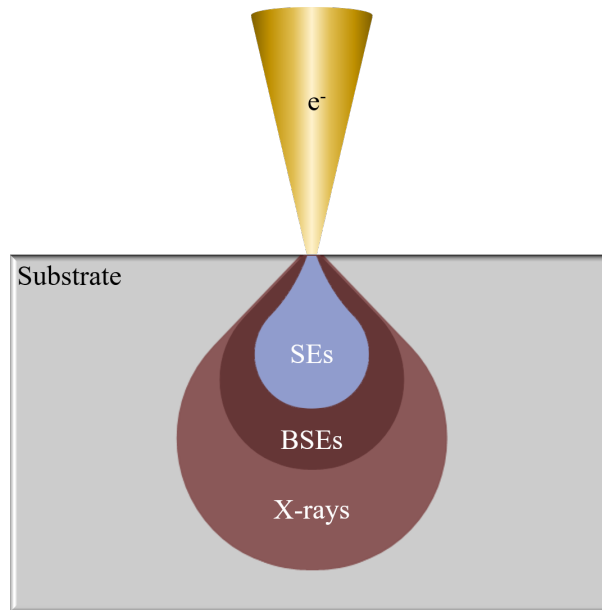
Figure 2.8: Schematic showing the escape depth of secondary electrons (SEs), backscattered electrons (BSEs), and characteristic X-rays in SEM.

primary electron beam, including SEs, BSEs, and characteristic X-rays.

A high energy electron beam incident on a surface can also produce characteristic X-rays. This process is illustrated in Figure 2.9. Electron impact knocks out a core electron (left), after which an outer electron will drop down in energy to fill the core hole, releasing energy. This energy may then be expelled in the form of an X-ray with an energy equal to the difference in energy between the core level and outer level. This X-ray may then be detected in a technique called energy-dispersive X-ray spectroscopy (EDX), which is commonly used in tandem with techniques like SEM in order to determine the elemental composition of an imaged surface. As light does not interact as strongly with matter as electrons do, X-rays have much larger IMFPs than electrons and therefore can come from much deeper in a sample. Thus, EDX
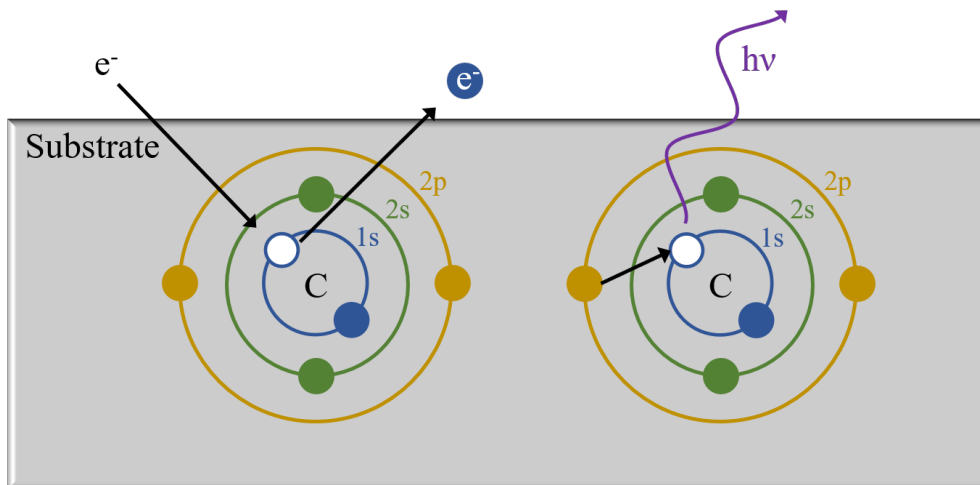
Figure 2.9: Electron impact ionization and subsequent emission of a characteristic X-ray from a carbon atom as used in EDX.

is not a surface sensitive technique. EDX may also be used to map elements on a surface, showing where various elements are localized.

2.2.2 Instrumentation

2.2.2.1 Main system experiments

Figure 2.10 shows the instrument used to perform *in situ* XPS and MS studies of the reactions of thin films of adsorbed organometallic species on cooled substrates upon exposure to electrons or argon ions. The substrate cooling system is shown on the right, and utilized liquid nitrogen-cooled compressed air that was blown through the substrate arm in order to cool the substrate. The substrate temperature was measured using a thermocouple. The substrate was able to be translated in the x, y, and z directions and rotated in the plane of the X-ray source, electron gun, and hemispherical analyzer (the yz plane).
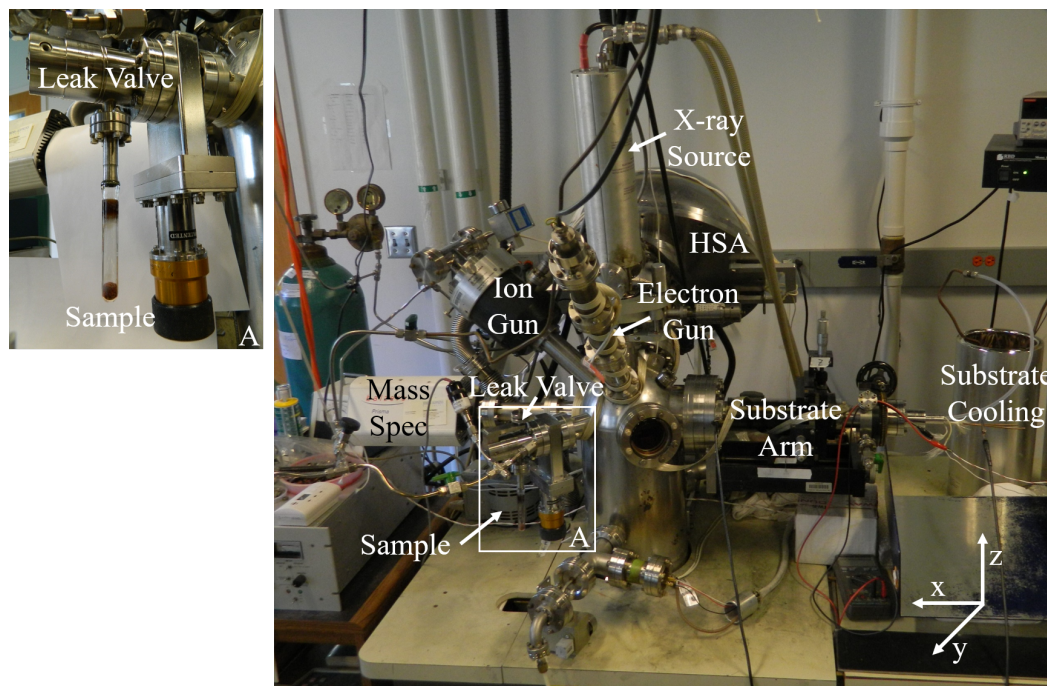
Figure 2.10: The primary instrument used in this dissertation, used for *in situ* XPS and MS measurements.

The electron gun and hemispherical analyzer are each at approximately 45° angles from the X-ray source, as is the ion gun. The sample holder is shown in the inset, labelled A. Sample compounds were sublimed either at room temperature or by heating with heating tape and leaked into the chamber using a leak valve, also pictured.

2.2.2.2 EBID experiments

Figure 2.11 shows the instrument used to perform EBID experiments with organometallic precursors. The substrate is introduced from an arm that is on the same plane as the sample arm, behind the instrument as seen in Fig. 2.11.
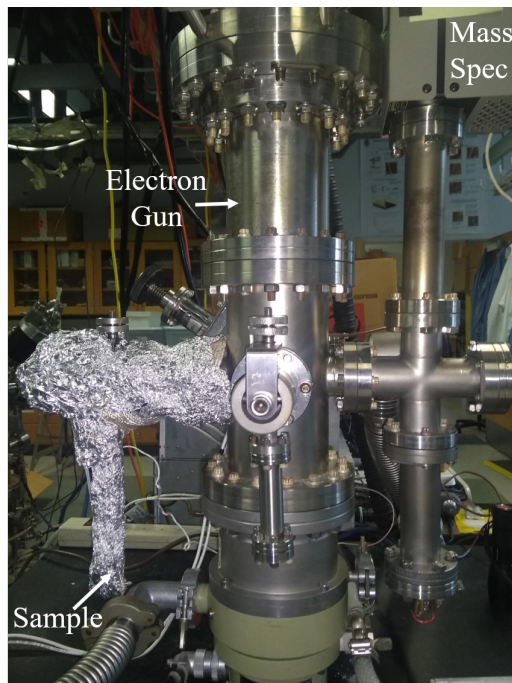
Figure 2.11: Instrument used to make electron beam induced deposition (EBID) deposits.

The sample holder, which is similar to that seen in Fig. 2.10, is shown with heating tape and aluminum foil used to maintain a constant heat along the sample arm. A metal capillary is used as a directional doser in order to deliver the precursor close to the substrate, similar to that which will be shown in Figure 2.12. The electron gun is also maintained at a small working distance (< 1 cm) from the substrate. The mass spectrometer may be used to ensure precursor purity as well as detect any volatile fragments produced during deposition.
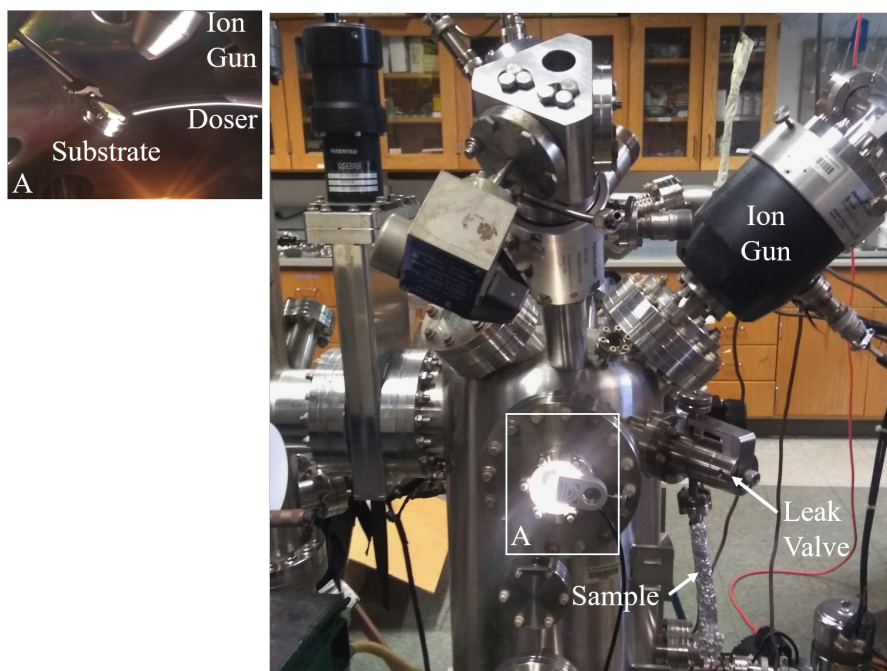
Figure 2.12: Instrument used to make ion beam induced deposition (IBID) deposits.

2.2.2.3 IBID experiments

Figure 2.12 shows the instrument used to perform IBID experiments with organometallic precursors. The sample is introduced through a leak valve attached to a metal capillary used as a directional doser, shown in inset A. The substrate is rotated such that the surface is normal to the ion gun, as is depicted in inset A.

References

[1] I. Utke, P. Hoffmann, J. Melngailis, *Journal of Vacuum Science & Technology B: Microelectronics and Nanometer Structures* **2008**, *26*, 1197.

[2] W. F. van Dorp, C. W. Hagen, *Journal of Applied Physics* **2008**, *104*, 081301.

[3] M. Huth, F. Porrati, C. Schwalb, M. Winhold, R. Sachser, M. Dukic, J. Adams, G. Fantner, *Beilstein Journal of Nanotechnology* **2012**, *3*, 597–619.

[4] O. Ingólfsson in *Low-Energy Electrons: Fundamentals and Applications*, (Ed.: O. Ingólfsson), Pan Stanford Publishing Pte. Ltd., Singapore, **2019**, Chapter Low Energy, pp. 47–120.

[5] R. M. Thorman, R. K. T. P., D. H. Fairbrother, O. Ingólfsson, *Beilstein Journal of Nanotechnology* **2015**, *6*, 1904–1926.

[6] R. M. Thorman, PhD thesis, University of Iceland, **2017**, pp. 1–130.

[7] E. Böhler, J. Warneke, P. Swiderek, *Chemical Society Reviews* **2013**, *42*, 9219–9231.

[8] S. Engmann, M. Stano, S. Matejčík, O. Ingólfsson, *Physical chemistry chemical physics : PCCP* **2012**, *14*, 14611–8.

[9] J. D. Wnuk, J. M. Gorham, S. G. Rosenberg, W. F. van Dorp, T. E. Madey, C. W. Hagen, D. H. Fairbrother, *The Journal of Physical Chemistry C* **2009**, *113*, 2487–2496.

[10] W. F. van Dorp, J. D. Wnuk, J. M. Gorham, D. H. Fairbrother, T. E. Madey, C. W. Hagen, *Journal of Applied Physics* **2009**, *106*, 074903.

[11] O. May, D. Kubala, M. Allan, A. A. Viggiano, G. K. Rekha, A. E. Stevens, G. A. Tolstikov, *Phys. Chem. Chem. Phys.* **2012**, *14*, 2979–2982.

[12] K. Landheer, S. G. Rosenberg, L. Bernau, P. Swiderek, I. Utke, C. W. Hagen, D. H. Fairbrother, *The Journal of Physical Chemistry C* **2011**, *115*, 17452–17463.

[13] K. Wnorowski, M. Stano, C. Matias, S. Denifl, W. Barszczewska, Š. Matejčík, *Rapid Communications in Mass Spectrometry* **2012**, *26*, 2093–2098.

[14] S. G. Rosenberg, M. Barclay, D. H. Fairbrother, *Physical Chemistry Chemical Physics* **2013**, *15*, 4002–4015.

[15] J. A. Spencer, J. A. Brannaka, M. Barclay, L. McElwee-White, D. H. Fairbrother, *The Journal of Physical Chemistry C* **2015**, *119*, 15349–15359.

[16] J. A. Spencer, Y.-C. Wu, L. McElwee-White, D. H. Fairbrother, *Journal of the American Chemical Society* **2016**, *138*, 9172–9182.

[17] I. Unlu, J. A. Spencer, K. R. Johnson, R. M. Thorman, O. Ingólfsson, L. McElwee-White, D. H. Fairbrother, *Physical Chemistry Chemical Physics* **2018**, *20*, 7862–7874.

[18] S. G. Rosenberg, M. Barclay, D. H. Fairbrother, *The Journal of Physical Chemistry C* **2013**, *117*, 16053–16064.

[19] R. K. T. P., I. Unlu, S. Barth, O. Ingólfsson, D. H. Fairbrother, *The Journal of Physical Chemistry C* **2018**, *122*, 2648–2660.

[20] R. K. T. P., P. Weirich, L. Hrachowina, M. Hanefeld, R. Bjornsson, H. R. Hrodmarsson, S. Barth, D. H. Fairbrother, M. Huth, O. Ingólfsson, *Beilstein Journal of Nanotechnology* **2018**, *9*, 555–579.

[21] J. A. Spencer, M. Barclay, M. J. Gallagher, R. Winkler, I. Unlu, Y.-C. Wu, H. Plank, L. McElwee-White, D. H. Fairbrother, *Beilstein Journal of Nanotechnology* **2017**, *8*, 2410–2424.

[22] M. Zlatar, M. Allan, J. Fedor, *The Journal of Physical Chemistry C* **2016**, *120*, 10667–10674.

[23] M. Allan, M. Lacko, P. Papp, Š. Matejčík, M. Zlatar, I. I. Fabrikant, J. Kočišek, J. Fedor, *Physical Chemistry Chemical Physics* **2018**, *20*, 11692–11701.

[24] M. Mendes, K. Regeta, F. Ferreira da Silva, N. C. Jones, S. V. Hoffmann, G. García, C. Daniel, P. Limão-Vieira, *Beilstein Journal of Nanotechnology* **2017**, *8*, 2208–2218.

[25] A. D. Dubner, A. Wagner, J. Melngailis, C. V. Thompson, *Journal of Applied Physics* **1991**, *70*, 665–673.

[26] P. Chen, H. W. M. Salemink, P. F. A. Alkemade, *Journal of Vacuum Science & Technology B: Microelectronics and Nanometer Structures* **2009**, *27*, 2718.

[27] J. Melngailis, *Journal of Vacuum Science & Technology B: Microelectronics and Nanometer Structures* **1987**, *5*, 469.

[28] J. S. Ro, C. V. Thompson, J. Melngailis, *Journal of Vacuum Science & Technology B: Microelectronics and Nanometer Structures* **1994**, *12*, 73.

[29] S. Lipp, L. Frey, C. Lehrer, E. Demm, S. Pauthner, H. Ryssel, *Microelectronics Reliability* **1996**, *36*, 1779–1782.

[30] P. Chen, E. van Veldhoven, C. A. Sanford, H. W. M. Salemink, D. J. Maas, D. A. Smith, P. D. Rack, P. F. A. Alkemade, *Nanotechnology* **2010**, *21*, 455302.

[31] I. Utke in *Nanofabrication using focused ion and electron beams: principles and applications*, (Eds.: I. Utke, S. Moshkalev, P. Russell), Oxford University Press, New York, **2012**, Chapter 6, pp. 248–285.

[32] E. H. Bjarnason, B. Ómarsson, S. Engmann, F. H. Ómarsson, O. Ingólfsson, *European Physical Journal D* **2014**, *68*, 121.

[33] NIST Mass Spectrometry Center; William E. Wallace; director in *NIST Chemistry WebBook, NIST Standard Reference Database Number 69*, (Eds.: P. Linstrom, W. Mallard), National Institute of Standards and Technology, Gaithersburg, MD 20899, Chapter Mass Spect.

Chapter 3

Identifying and rationalizing the differing surface reactions of low energy electrons and ions with an organometallic precursor

This work is adapted with permission from:

R. M. Thorman, S. J. Matsuda, L. McElwee-White, D. H. Fairbrother, Identifying and Rationalizing the Differing Surface Reactions of Low-Energy Electrons and Ions with an Organometallic Precursor, *The Journal of Physical Chemistry Letters* **2020**, 11(6), 2006–2013. DOI: 10.1021/acs.jpclett.0c00061

Copyright 2020, American Chemical Society.

3.1 Introduction

Focused electron beam-induced deposition (FEBID) and focused ion beam-induced deposition (FIBID) are single-step deposition process where well-defined three-dimensional nanostructures can be "written" onto planar or

nonplanar surfaces with an electron or ion beam "pen".[1–5] In both FEBID and FIBID, a substrate in a high vacuum system is exposed to a constant flux of a volatile organometallic precursor via a gas inlet system. A high energy (1 – 30 kV), tightly-focused electron or ion beam impacts the surface, decomposing physisorbed precursor molecules. Nonvolatile metal-containing fragments deposit onto the substrate, creating metal-containing nanostructures, while volatile fragments/ligands desorb.

In FEBID, deposition is generally understood to be initiated by low-energy electrons (LEEs, < 100 eV) generated by the interaction of the primary beam with the substrate.[1, 6–8] The initial reaction step involves electron attachment, ionization, or electronic excitation of the precursor and is typically characterized by a degree of ligand loss and the formation of a surface-bound intermediate containing the metal atom and residual ligands.[9–16] Further electron irradiation, however, typically leads to decomposition of the residual ligands rather than further ligand desorption.[11–13, 15] An exception to this process occurs when metal-halogen bonds are present, where the halogen atoms can be removed by electron-stimulated desorption.[9, 10] The second step is typically responsible for the majority of the organic contamination in the final deposit (e.g. $W(CO)_6$).[13]

Far fewer insights exist on the fundamental bond-breaking processes involved in FIBID. This is in part because a number of different processes can contribute to the initial deposition step in FIBID,[1, 17, 18] including interactions between the primary ion and the adsorbate and/or reactions between the adsorbate and secondary electrons generated by the impact of the primary ion

beam with the substrate. FIBID can also proceed through momentum/energy transfer between the incident ion and the substrate.[17] In the ion-limited regime of FIBID, deposition is limited by the flux of incident ions rather than the coverage of precursor molecules.[1] Ion-molecule interactions are therefore expected to play a particularly important role in this regime, although the interaction of the ion beam with the adsorbate/substrate will also generate secondary electrons and thus electron-molecule interactions may also contribute. The importance of studying ion-induced reactions with adsorbed films of precursor molecules has been further emphasized by a recent report demonstrating the use of cryo-FIBID to grow metallic contacts over 600 times faster than in conventional FIBID.[19, 20]

In this study, we undertake a molecular-level surface science approach to determine and compare the sequence of bond-breaking steps that occur when an organometallic precursor ((η^5-Cp)Fe(CO)$_2$Re(CO)$_5$) is exposed to either low energy (< 1 keV) argon ions or electrons. Argon ions were used to eliminate ion implantation, which was not observed on the Au substrate, and reactions associated with ion fragmentation (e.g., oxidation when using O^{2+}). The effects of low energy electron (500 eV) and Ar^+ (860 eV) irradiation on nanometer-scale films of (η^5-Cp)Fe(CO)$_2$Re(CO)$_5$ have been studied using *in situ* X-ray photoelectron spectroscopy (XPS) to probe changes in bonding and chemical composition and mass spectrometry (MS) to identify volatile species, produced during electron/ion exposure.
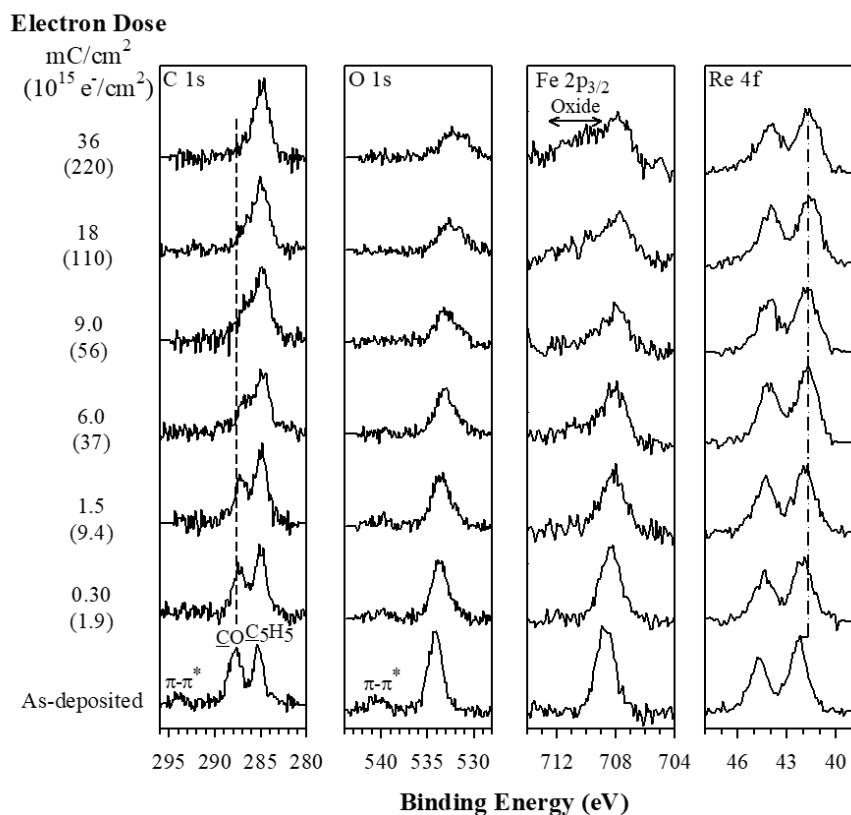
Figure 3.1: Changes to the C (1s), O (1s), Fe ($2p_{3/2}$), and Re (4f) XPS regions upon 500 eV electron irradiation of $\approx 1.5 - 2.0$ nm CpFe(CO)$_2$Re(CO)$_5$ thin films adsorbed on polycrystalline gold substrates at -100 °C, corresponding to approximately 1-2ML coverage. The bottom spectrum represents the adsorbed ("as deposited") film prior to electron irradiation. A dashed line in the C (1s) region denotes the binding energy of carbon associated with the carbonyl ligand. The horizontal arrows in the Fe ($2p_{3/2}$) spectrum show the region where oxidized iron is observed. The dash-dot line in the Re (4f) region shows the change in binding energies of the Re ($4f_{7/2}$) peak during electron irradiation. Electron dose is shown on the left-hand side expressed in terms of both current density (mC/cm^2) and in effective dose (e$^-$/cm^2).

3.2   Results and Discussion

Figures 3.1 and 3.2 contrast the effect of electron and Ar$^+$ irradiation on 1.5-2.0 nm thick (η^5-Cp)Fe(CO)$_2$Re(CO)$_5$ films, respectively. Analysis of the "as

47

deposited" films indicates that $(\eta^5\text{-Cp})\text{Fe(CO)}_2\text{Re(CO)}_5$ adsorbs molecularly onto the Au substrates at -100 °C (see SI for details), while control studies (Figure 3.7) reveal that $(\eta^5\text{-Cp})\text{Fe(CO)}_2\text{Re(CO)}_5$ films were unchanged by X-rays for the irradiation times needed to acquire spectra.

Under the influence of electron irradiation (Fig. 3.1), the carbonyl (CO) C (1s) peak initially at 287.8 eV decreases in intensity and shifts to slightly low binding energy, while the CO π-to-π* shakeup feature at 294.0 eV disappears. For electron doses > 6.0 mC/cm^2, the CO peak is observed as a higher binding energy shoulder to the larger C(1s) peak at 285.3 eV. This larger peak corresponds to CC/CH species, including the carbon atoms in the cyclopentadienyl ligand. For the highest electron doses (36 mC/cm^2), only a single C (1s) peak is observed at 284.9 eV.

In the O (1s) region, a systematic decrease in the O (1s) peak intensity occurs for electron doses < 6.0 mC/cm^2. At larger electron doses, however, the intensity in the O (1s) region remains roughly constant, although the peak shape changes. A lower binding energy shoulder grows in, culminating in a broad, low-intensity peak centered at $\approx$ 532.1 eV, consistent with oxide formation.[11] In the Fe (2p$_{3/2}$) region, the peak position downshifts slightly during the initial stages of electron irradiation, although the most obvious change is the peak broadening to higher binding energies for electron doses > 6.0 mC/cm^2, indicative of iron oxidation.[21] In the Re(4f) region, for electron doses < 6.0 mC/cm^2, the peaks broaden and the Re (4f$_{7/2}$) binding energy decreases from 42.3 eV to 41.6 eV. For doses > 6.0 mC/cm^2, the Re (4f) peak profile is essentially unchanged. In contrast to the C(1s) and O(1s) regions,
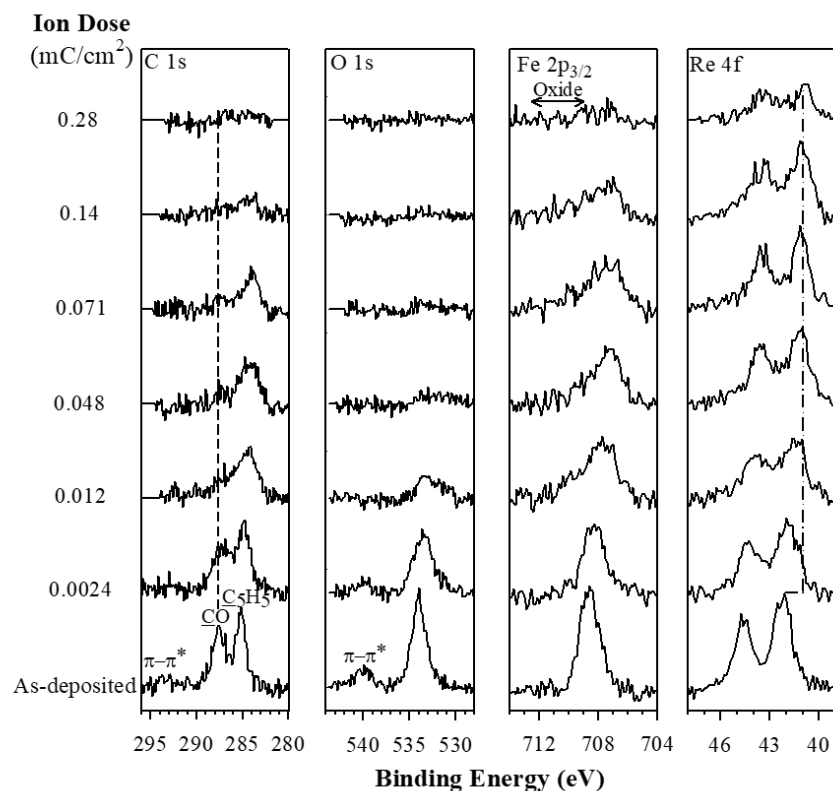
Figure 3.2: Evolution of C (1s), O (1s), Fe ($2p_{3/2}$), and Re (4f) XPS regions upon 860 eV Ar^+ bombardment of $\approx 1.3 - 1.8$ nm thin films of $CpFe(CO)_2Re(CO)_5$, corresponding to approximately 1-2ML coverage. The bottom spectrum represents the adsorbed film prior to argon ion bombardment. The dashed vertical line in the C (1s) region denotes the binding energy of carbon atoms associated with carbonyl ligands. Arrows in the top Fe ($2p_{3/2}$) spectrum show the region in which iron oxidation would be expected. The dash-dot line in the Re (4f) region shows the shift in binding energy of the Re ($4f_{7/2}$) peak. Argon ion dose is reported on the left-hand side in current density (mC/cm^2).

changes to the Fe(2p) spectral envelopes and Re (4f) regions occur without measurable changes to metal atom coverage (see Fig. 3.1).

Figure 3.2 shows that the effect of Ar^+ bombardment on adsorbed (η^5-Cp)Fe(CO)$_2$Re(CO)$_5$ molecules differs significantly from electron irradiation. In the C(1s) region, the CO peak decreases in intensity and has disappeared

after about 0.048 mC/cm^2 of Ar$^+$ exposure. During this same period of Ar$^+$ bombardment, the cyclopentadienyl C (1s) peak at 285.3 eV broadens, becoming an asymmetric peak centered at $\approx$ 284.1 eV with intensity of $\approx$ 80 % of the initial cyclopentadienyl C (1s) peak area. For Ar$^+$ exposures > 0.048 mC/cm^2, this peak begins to decrease in intensity until no carbon atoms remain after 0.28 mC/cm^2 of Ar$^+$ bombardment. Changes in the O (1s) region are even more distinct from those due to electron irradiation. Notably, Ar$^+$ bombardment leads to a rapid decrease in the coverage of oxygen atoms; after 0.048 mC/cm^2 of Ar$^+$ exposure, no oxygen atoms remain. Changes to the Fe (2p$_{3/2}$) region are characterized by peak broadening, a noticeable decrease in binding energy (from 708.7 eV to 707.2 eV after 0.14 mC/cm^2) and a steady decrease in overall signal intensity, albeit at a slower rate than in the O (1s) region. After 0.28 mC/cm^2 of Ar$^+$ exposure, virtually all the iron has been removed. In contrast to electron irradiation (Fig. 3.1), no iron oxide shoulder is observed in the Fe (2p$_{3/2}$) region between 709 and 711 eV. Analogous to the Fe (2p$_{3/2}$) region, the Re (4f) doublet also broadens and shifts to lower binding energy upon Ar$^+$ bombardment. The Re (4f) signal intensity also decreases, although a measurable Re atom coverage still remains after 0.28 mC/cm^2 of Ar$^+$ bombardment.

Electron irradiation: The electron beam-induced reactions of adsorbed (η^5-Cp)Fe(CO)$_2$Re(CO)$_5$ occur in two sequential steps: the first taking place at electron doses of $\leq$ 6.0 mC/cm^2, and the second at doses $\geq$ 6.0 mC/cm^2. This can be seen in Figure 3.3, which shows the effect of electron and ion beam irradiation on the fractional coverage of oxygen, carbon, and rhenium atoms,
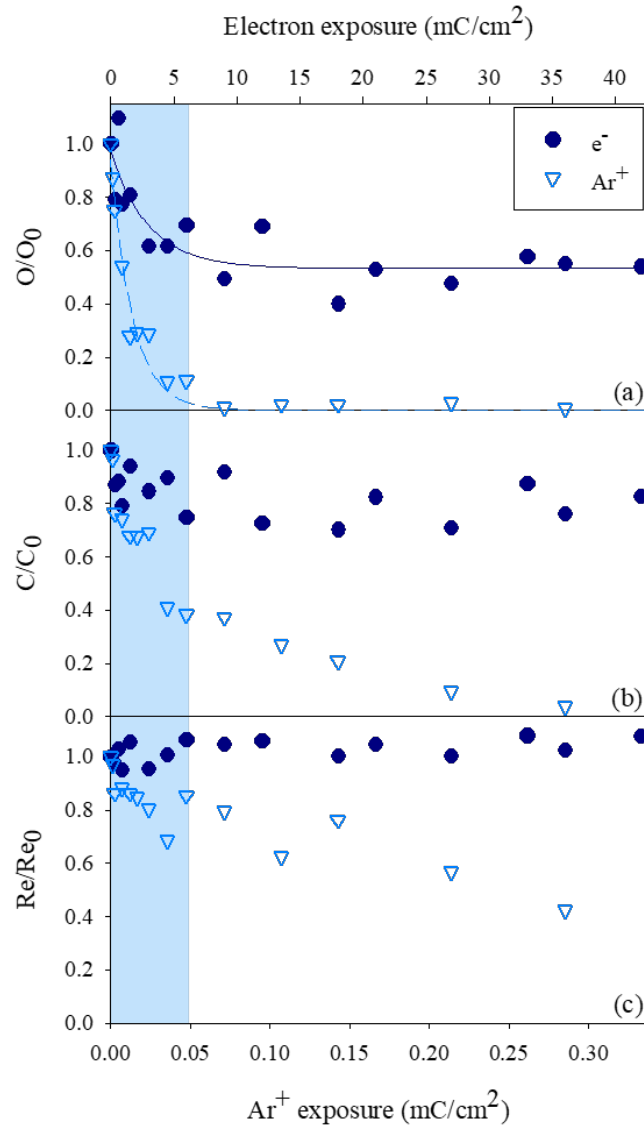
Figure 3.3: Changes in the fractional coverage of (a) oxygen, (b) carbon, and (c) rhenium atoms upon electron (dark circles, top x axis) and argon ion (light open triangles, bottom x axis) exposure. The changes in composition which occur during the initial region of electron (≈ 6.0 mC/cm^2) or argon ion (≈ 0.048 mC/cm^2) exposure are denoted by the blue shaded region. The decay in the fractional coverage of oxygen atoms by electron (dark solid line) and argon ion (light dashed line) exposure has been fit using an exponential decay profile of $(O_j/O_0) = Ae^{-b_j} + c$, where j is the total electron or argon exposure and (O_j/O_0) is the fractional coverage of oxygen atoms; A, b and c are constants.
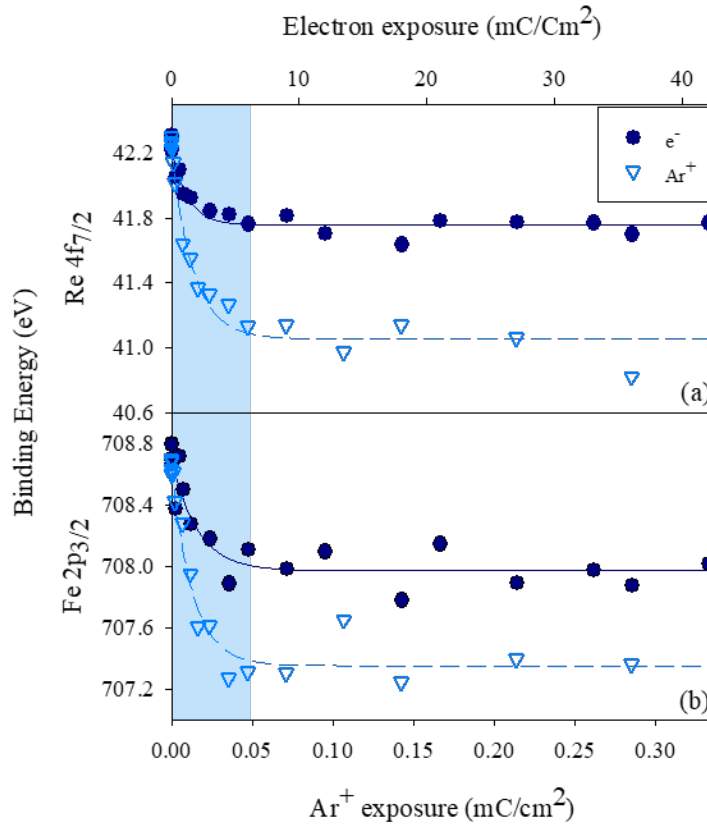
Figure 3.4: Changes in the binding energies of the (a) Re ($4f_{7/2}$) peak and (b) Fe ($2p_{3/2}$) peak upon electron (dark circles, top x axis) and argon ion (inverted open triangles, bottom x axis) exposure. The initial ≈ 6.0 mC/cm^2 of electron exposure and 0.048 mC/cm^2 of argon ion exposure are denoted by the blue shaded region. The shift in peak positions by electron (dark solid line) and argon ion (light dashed line) exposure has been fit using exponential decay profiles of the form $y_j = Ae^{-b_j} + c$, where y_j is the binding energy at electron or argon ion exposure j, and c is the binding energy at the end of the exposure.

and Figure 3.4, which shows the corresponding changes in binding energies of the Re ($4f_{7/2}$) and Fe ($2p_{3/2}$) peaks. Electron doses < 6.0 mC/cm^2, shown as the blue shaded region, produce an exponential loss in the relative coverage of oxygen and carbon (Fig. 3.3) along with a concomitant decrease in the binding energies of the Fe ($2p_{3/2}$) and Re ($4f$) peaks (Fig. 3.4). For electron doses ≥ 6.0
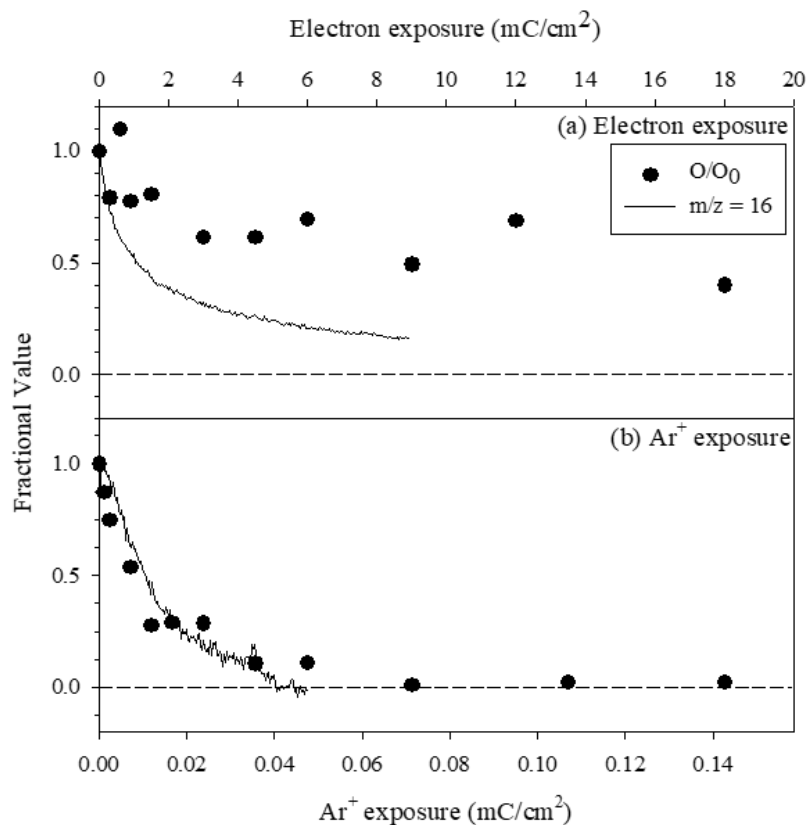
Figure 3.5: Kinetics of gas phase CO evolution from $\approx$ 1.5 – 2.0 nm thin films of adsorbed $CpFe(CO)_2Re(CO)_5$ upon (a) 500 eV electron irradiation (top x axis) and (b) 860 eV Ar^+ bombardment (bottom x axis) as measured by the O (m/z = 16) peak (solid black line). For both electron and ion exposure the normalized O signal observed by mass spectrometry is overlaid with the concurrent change in the fractional oxygen coverage as measured by the O (1s) XPS signal (solid black circles). The O signal was chosen over the more intense m/z = 28 signal in order to avoid potential contamination from other species (e.g. N_2) at m/z = 28. The C signal (m/z = 12) exhibited the same decay profile as the O (m/z = 16) signal (Figure 3.9), showing that both fragments originate exclusively from CO.

mC/cm^2, each of these parameters remains constant. These initial changes

in the XPS spectra are caused by electron-stimulated decomposition of the

precursor, which leads to CO desorption as observed directly by MS (Figs.

3.5 and 3.8). Based on the fractional decreases in the O (1s) regions, we can

53

conclude that about half (3 - 4) of the CO ligands in the precursor desorb as a consequence of electron-stimulated decomposition (Fig. 3.9). The decrease in both the Fe ($2p_{3/2}$) and Re ($4f_{7/2}$) binding energies during this same period of electron irradiation (Figs. 3.1 and 3.4) is a consequence of precursor decomposition/decarbonylation. Analysis of Figs. 3.1 and 3.3 demonstrates that all of the carbon atoms in the Cp ligand remain.[9, 11] While the presence or absence of H cannot be detected with XPS, previous studies have demonstrated electron-stimulated C–H bond cleavage in adsorbed organic molecules.[22–25] We can therefore reasonably assume that the Cp ligand decomposes thus:

$$C_5H_{5(ads)} + e^- \rightarrow 5C_{(ads)} + \frac{5}{2}H_{2(g)} \uparrow \tag{3.1}$$
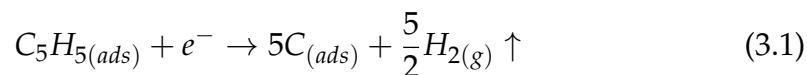
The initial precursor decomposition/deposition step can therefore be summarized as:

$$CpFe(CO)_2Re(CO)_{5(ads)} + e^- \rightarrow C_5FeRe(CO)_{(7-n)(ads)} + nCO_{(g)} \uparrow \tag{3.2}$$

$$+ \frac{5}{2}H_{2(g)} \uparrow \quad (n = 3 - 4)$$
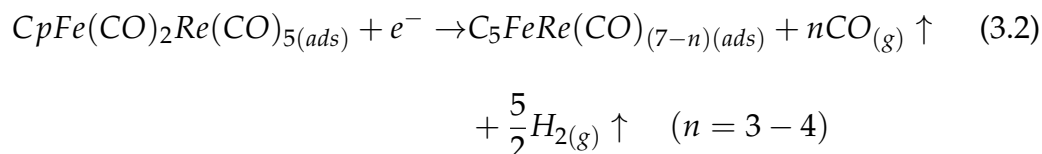
This reaction step is illustrated in Figure 3.6 (top), with the product best viewed as a partially decarbonylated intermediate.[9, 11–13, 16] Based on previous studies, the desorption of multiple CO ligands suggests that precursor decomposition is a consequence of dissociative ionization;[26, 27] however, this cannot be conclusively determined. This hypothesis is supported by MS data of gas phase (η^5-Cp)Fe(CO)$_2$Re(CO)$_5$ (Figure 3.10) which shows that 70 eV electron bombardment also leads principally to fragments formed by
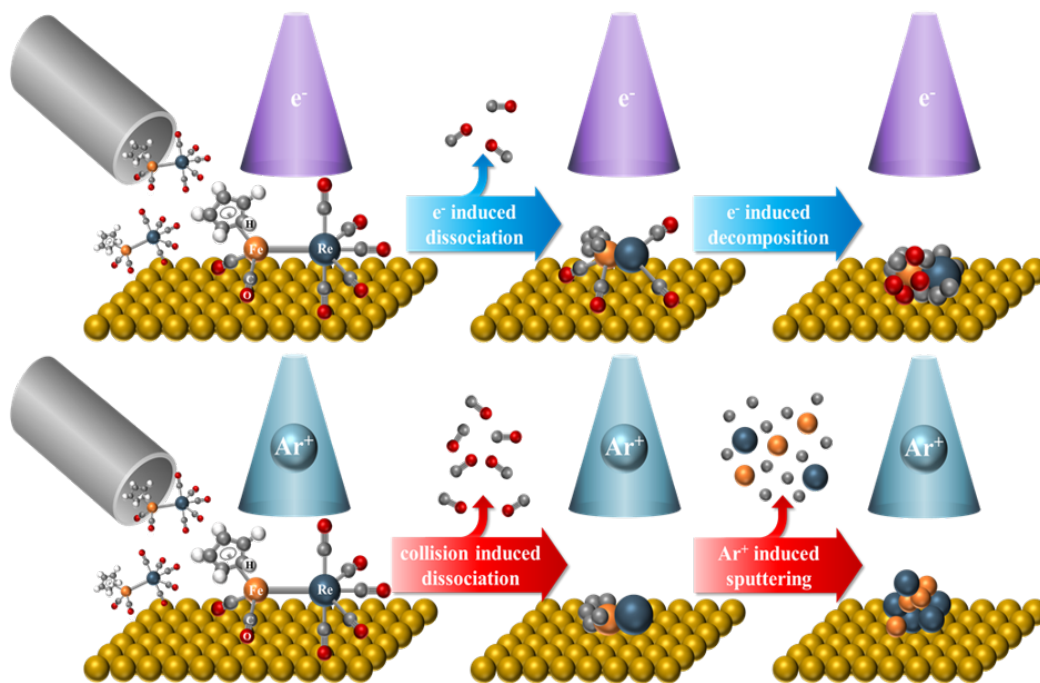
Figure 3.6: Schematic representation of the sequence of molecular-level events that accompany the 500 eV electron (top) and 860 eV Ar^+ ion (bottom) exposure of adsorbed $CpFe(CO)_2Re(CO)_5$ on a gold substrate.

multiple CO ligand loss.

For electron doses ≥ 6.0 mC/cm^2, the XPS data (Figs. 3.1, 3.3, and 3.4) show that no further carbon or oxygen desorbs and the Fe ($2p_{3/2}$) and Re ($4f$) binding energies remain unchanged. However, changes in the C ($1s$) and O ($1s$) spectral envelopes indicate that the CO ligands in the partially decarbonylated intermediate described in Eq. 3.2 decompose under the influence of continued electron irradiation. In the C ($1s$) region, the high binding energy shoulder associated with the residual CO groups disappears while the principal carbon peak at 284.9 eV associated with C-C/C-H species increases in intensity. In the O ($1s$) region, the appearance of a lower-binding energy O ($1s$) shoulder

and the growth of the higher-binding energy Fe ($2p_{3/2}$) shoulder indicate iron oxidation. Thus, electron-stimulated decomposition of these residual CO ligands produces graphitic carbon and reactive oxygen species (ROS) which oxidize iron:

$$CO_{(ads)} + e^- \rightarrow C_{(ads)} + ROS \tag{3.3}$$

$$ROS + Fe_{(ads)} \rightarrow Fe_xO_{y(ads)} \tag{3.4}$$
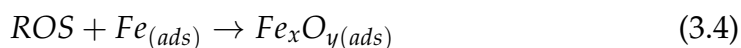
The sequence of electron-induced reactions shown in Fig. 3.6 (top) is similar to the electron-stimulated reactions reported for other carbonyl-containing organometallics.[11–13, 15] The incomplete desorption of the CO ligands from (η^5-Cp)Fe(CO)$_2$Re(CO)$_5$ also provides a rationale for the poor fit between the CO desorption rate and the oxygen coverage determined by XPS (Fig. 3.5). However, we can re-analyze the CO desorption data, adding an offset (determined by XPS) to reflect the observation that only some of the oxygen atoms/CO ligands desorb. The rate of CO desorption is now well correlated with the fractional loss of oxygen that occurs during the electron-stimulated decomposition of the precursor (Figure 3.11).

Ion bombardment: Analysis of Figs. 3.2 and 3.3 shows that ion-induced reactions with (η^5-Cp)Fe(CO)$_2$Re(CO)$_5$ also occur in two regimes, the first of which is indicated by the shaded blue region in Figs. 3.3 and 3.4. In this initial $\approx$ 0.048 mC/cm^2 of ion bombardment, some ion-induced precursor desorption may occur as demonstrated by the $\approx$ 20 % decrease in the Re signal, but the much more significant changes in both the C (1s) and O (1s) regions indicate that this initial phase is dominated by ion-induced reactions

with the organometallic precursor. Most significantly, Fig. 2 shows that $\approx$ 0.048 mC/cm^2 of Ar$^+$ exposure completely removes all intensity in the O (1s) region, as well as all C (1s) intensity at 287.8 eV associated with the carbonyl ligand, suggesting that all carbonyl ligands have desorbed. This assertion is supported by the correlation between the CO desorption rate observed by MS and the fractional CO coverage on the surface determined by the O (1s) XPS area (Figure 3.5). Figures 3.2 and 3.4 also show that both the Fe (2p$_{3/2}$) and Re (4f) peaks decrease in binding energy as all of the CO ligands desorb, to values proximate to those of the pure metals.[28–30] In comparison, the decrease in the Fe (2p$_{3/2}$) and Re (4f) peak positions during electron exposure is roughly half of that from ion exposure, likely a consequence of the incomplete CO desorption during electron exposure. At this stage of the Ar$^+$-induced reaction sequence, when all CO ligands have desorbed from the (η^5-Cp)Fe(CO)$_2$Re(CO)$_5$ molecules, $\approx$ 40 % of the initial carbon remains (Fig. 3.3), consistent with the remaining carbon being derived from the cyclopentadienyl ring. Based on previous studies of molecular ion-induced reactions with hydrocarbons[31] and the significant broadening of the C (1s) peak, we believe that the cyclopentadienyl ligand is dehydrogenated during this period. Therefore, in addition to a small amount of ion-induced sputtering/desorption, the initial ion-induced reactions can be summarized by Eq.3.5 and Fig. 3.6 (bottom):

$$CpFe(CO)_2Re(CO)_{5(ads)} + Ar^+_{(g)}(860eV) \rightarrow C_5FeRe_{(ads)} + 7CO_{(g)} \uparrow \quad (3.5)$$

$$+ \frac{5}{2}H_{2(g)} \uparrow$$
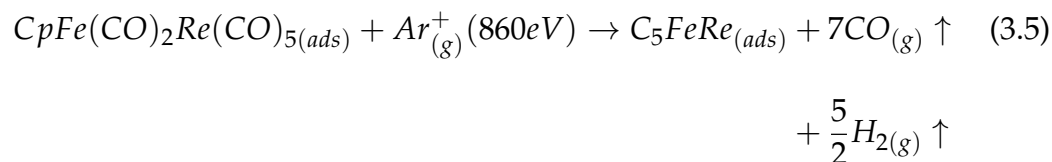
Thus, while all the carbonyl ligands desorb, no cyclopentadienyl carbon atoms are removed from the surface. More sustained Ar^+ bombardment (> 0.048 mC/cm^2) causes ion-induced physical sputtering, as shown in Fig. 3.6 (bottom). This is evidenced by decreases in intensities within the C (1s), Fe (2p$_{3/2}$), and Re (4f) regions (Figs. 3.2 and 3.3).

In our experiment, the low energy (860 eV) and ion flux (measured target current < -100 nA/cm^2; calculated ion current $\approx$ 40 nA/cm^2) are likely to limit any processes initiated by surface activation, including thermal effects. Indeed, we did not observe any increase in substrate temperature during ion exposure, even when the ion beam was incident upon the thermocouple attached to the backside of the sample holder. Consequently, our results are a consequence of low-energy ion-molecule and/or electron-molecule interactions.

Comparing the effects of low-energy electron and Ar^+ exposure, it is evident that the two processes are mechanistically different. Electron-induced reactions of (η^5-Cp)Fe(CO)$_2$Re(CO)$_5$ are characterized by desorption of only half of the CO ligands (Eq. 3.2) followed by decomposition of the residual CO ligands (Eq. 3.3). In contrast, all CO ligands desorb during ion-beam exposure (Eq. 3.5) followed by physical sputtering of the remaining atoms. These differences support the hypothesis that direct ion-induced reactions of (η^5-Cp)Fe(CO)$_2$Re(CO)$_5$ are dominated by ion-molecule interactions, rather

58

than reactions between the adsorbate and low energy secondary electrons generated by the interactions of the primary ion beam with the substrate.

In direct ion-molecule interactions, a significant amount of energy will be transferred during the collision of the 860 eV Ar^+ and the adsorbed (stationary) $(\eta^5\text{-Cp})Fe(CO)_2Re(CO)_5$ molecules. If this interaction is modelled as a simple head-on collision between an incident ion and an adsorbed precursor,[17] then the maximum energy (ΔK) that can be transferred assuming a perfectly elastic collision with impact parameter $b \approx 0$ is:

$$\Delta K = K \times \frac{4m_{ion}m_{mol}}{(m_{ion} + m_{mol}^2}$$

(3.6)

Where K is the kinetic energy of the incident ion, m_{ion} is the mass of the ion, and m_{mol} is the mass of the adsorbed molecule. Using this equation for an 860 eV incident Ar^+, the maximum energy that can be transferred to $(\eta^5\text{-Cp})Fe(CO)_2Re(CO)_5$ is calculated as 235 eV. In reality, the energy transferred will depend on the impact parameter and thus fall between 0 – 218.3 eV. Typically, M-CO ligands have bond dissociation energies (BDEs) of 1-2 eV.[32–37] It is thus apparent that, for the vast majority of the collisions, the energy transferred will be well in excess of that required to dissociate all the M-CO ligands. The MS data (Fig. 3.8) shows that CO desorbs once it has been generated. We postulate that for the CO ligands, energy transfer leads to M-CO dissociation rather than C≡O dissociation because of the significant disparity in the energy required for M-CO dissociation (< 2 eV) as compared to C≡O dissociation (BDE = 11.16 eV).[38]

The η^5-cyclopentadienyl ligand has a slightly higher M-L BDE than the CO

ligands (the first Fe-Cp BDE in ferrocene is 4 eV, while the second is 2.2 eV),[39] while the C-C and C-H bonds have BDEs of $\approx$ 5 eV.[40, 41] It is thus likely that the energy transferred during the ion-precursor collision will lead to a mixture of ligand dissociation and decomposition. Although our experimental data does not allow determination of the detailed fate of the Cp ligand, it is apparent that any Fe-Cp bond dissociation does not lead to Cp desorption as the carbon atoms associated with it remain on the surface during this initial period (Figs. 3.2 and 3.3) and it is not evident desorbing from the surface via MS (Fig. 3.8). On Cu(100), cyclopentadienyl has been shown to be stable up to 600 K due to strong chemisorption;[42] it is therefore possible that any intact Cp ligands dissociated from Fe during precursor decomposition will similarly remain on the surface and be decomposed by subsequent ion bombardment as hypothesized in Eq. 3.5. Interestingly, despite the large quantity of energy transferred to $(\eta^5\text{-Cp})\text{Fe}(CO)_2\text{Re}(CO)_5$ upon Ar^+ impact, bond dissociation within the precursor rather than molecular desorption dominates, even though the molecules are only physisorbed.

Our results can also be compared to previous studies of ion-induced reactions with adsorbed molecules and thin films. For example, physical sputtering of CO and NH_3 was dominant during $10 - 1000$ eV Xe^+ and SF_5^+ bombardment of CO or NH_3 adsorbed on Ni(111).[43] This is consistent with our observation of CO desorption predominating over CO decomposition. In related studies, the modification of alkanethiolate self-assembled monolayers by organic ions was independent of the chemical ion and consistent with momentum transfer,[31] analogous to the mechanism proposed in the present

study and similar to models used to explain surface-induced dissociation.[44]

3.3 Conclusions

The present study reveals for the first time how a surface science approach can elucidate and compare the sequence of elementary steps involved in FEBID and FIBID of metal containing nanostructures, including reactions of different ligands. In FEBID, this involves a two-step process characterized by initial ligand desorption mediated by electronic excitation and decomposition of the precursor, typically followed by ligand decomposition as seen for $(\eta^5\text{-Cp})\text{Fe(CO)}_2\text{Re(CO)}_5$ and other precursors.[11–15] In contrast, FIBID is found to be initiated by a transfer of energy between the incident ion and the stationary adsorbate, which in the case of $(\eta^5\text{-Cp})\text{Fe(CO)}_2\text{Re(CO)}_5$ leads to complete CO desorption. The residual carbon atoms associated with the Cp ligand are subsequently removed by physical sputtering, along with the Fe and Re atoms. In FEBID, this type of fundamental information has already been used to rationalize the composition of deposits and to develop new precursors for FEBID (e.g. $\text{Pt(CO)}_2\text{Cl}_2$).[10, 45] Data from the present study indicates that deposits created by FIBID using $(\eta^5\text{-Cp})\text{Fe(CO)}_2\text{Re(CO)}_5$ will be devoid of CO and it would be possible to create deposits containing only Fe and Re atoms by tuning the ion/precursor flux. Our results also suggest that the momentum transfer process underlying deposition in low energy FIBID in the ion-limited regime will lead to complete or near-complete carbonyl removal for some metal carbonyls, a process typically not found in FEBID.[46] Low energy ion-induced deposition using inert ions and metal carbonyl precursors

could thus provide a route to produce deposits with extremely high metal contents,[47] although deposit composition will also depend on the balance between precursor and ion flux.

3.4 Supporting Information

3.4.1 Experimental Procedures

Synthesis. General: Unless otherwise stated, all reactions were carried out under an inert atmosphere (N_2) using standard Schlenk techniques. $Re_2(CO)_{10}$ was purchased from Strem Chemicals. All other reagents were purchased from Sigma-Aldrich and used without further purification. All solvents were purified using a MBraun MB-SP solvent purification system and stored over 4 Å molecular sieves.

CpFe(CO)₂Re(CO)₅: CpFe(CO)$_2$Re(CO)$_5$ was synthesized using a modified literature procedure.[48] $Re_2(CO)_{10}$ (223.5 mg, 0.3425 mmol) and [CpFe(CO)$_2$]$_2$ (250.8 mg, 0.7086 mmol) were dissolved in 300 mL of toluene. The solution was purged with CO for 1 h. The solution was then irradiated using a 450 W medium pressure mercury arc lamp for 3 h in the presence of slowly bubbling CO. Solvent was then removed *in vacuo*, and the product was isolated by column chromatography on silica with hexanes as the eluent. Only a single dark orange band was evident on the column. Collection of this band and removal of the solvent by evaporation afforded the crude product as a brown precipitate that sublimed at room temperature at 100 mTorr. Crude yield: 175.4 mg, 51%. Yield after sublimation: 117.5 mg, 34%. The compound was characterized by comparison to literature data.1 ^{1}H NMR (300 MHz, C$_6$D$_6$)

δ 4.05 (s, 5H). IR (hexanes): 2103 (m), 2029 (w), 1993 (vs), 1975 (s), 1966 (w), 1933 (m) cm^{-1}.

Thin film preparation and characterization: All surface science experiments were performed in an ultra-high vacuum (UHV) chamber equipped with an XPS, quadrupole mass spectrometer (QMS), flood electron gun, and ion gun.[49–51] The compound was heated to 40-45 °C and deposited onto a cooled gold substrate (-100 °C). The adsorbed compound formed $\approx 1.5 - 2.0$ nm thin films, measured by XPS.

Electron irradiation: The incident electron energy was 500 eV, calculated from the energy of the flood gun (480 eV) and a bias applied to the substrate (+20 V) to ensure secondary electrons remained on the substrate. Electron flux is reported in terms of current density (mC/cm^2) and dose (e$^-$/cm^2, 1 x 10^{17} e$^-$/cm^2 = 16 mC/cm^2), in order to be more directly comparable to previous electron irradiation experiments. During electron irradiation, the sample was rotated so that the electron beam was incident along the surface normal.

Ion bombardment: Ion bombardment was performed using a Perkin-Elmer PHI model 04-303 differentially pumped ion gun. The primary Ar$^+$ beam energy was 880 V, and the substrate was biased at +20 V to prevent the escape of secondary electrons, giving a relative beam energy of 860 V. The ion gun was oriented at approximately 45° from the surface normal, giving a beam energy of approximately 600 V along the surface normal. A target current of $\approx$ -70 nA was maintained. Argon bombardment is reported in terms of current density (mC/cm^2). This was derived by performing a depth profile experiment on the well-studied SiO$_2$ native oxide grown on a silicon <100>

wafer using an analogous ion gun/XPS instrument with the same ion gun settings. By calculating the sputter rate (m/s) and using the known sputter yield of SiO_2 at 600 V ($\approx$ 1.02),[52] the current density on the surface could be calculated using the equation $j_p = z/t^*\rho^*N_A^*e/(M^*S)$, where j_p is the primary ion current density, z/t is the sputter rate, ρ is the density of the target (SiO_2), N_A is Avogadro's number, e is the charge of an electron, M is the molar mass of the target, and S is the sputter yield of the target.[53] The primary ion current density was thus calculated to be $\approx$ 40 nA/cm^2.

Both the Ar^+ and electron beams were defocused to ensure that the entire 1cm^2 surface was exposed to ions or electrons, respectively.

3.4.2 Results and Discussion

Upon $CpFe(CO)_2Re(CO)_5$ adsorption, Figure 3.7 shows that the C (1s) region consists of two main peaks: one corresponding to the cyclopentadienyl ligand (C_5H_5) at 285.3 eV, and one corresponding to the seven carbonyl ligands (CO) at 287.8 eV;[11] the higher energy peak (294.0 eV) is due to a π-to-π^* transition in the CO ligands.[11] The ratio between the cyclopentadienyl C (1s) signal and the carbonyl C (1s) signal is $\approx$ 0.7:1, equal to the ratio in $CpFe(CO)_2Re(CO)_5$. The O (1s) region shows one main peak at 534.2 eV, associated with the carbonyl oxygen (CO) and a small, higher-energy peak at 540.4 eV due to a π-to-π^* shakeup.[11] The intensity ratio between the C (1s) and O (1s) regions is 1.5 : 1.0, within experimental error of the 1.7 : 1.0 molecular ratio in $CpFe(CO)_2Re(CO)_5$. The Fe ($2p_{3/2}$) region consists of a single symmetric peak at 708.7 eV, while the Re (4f) region consists of
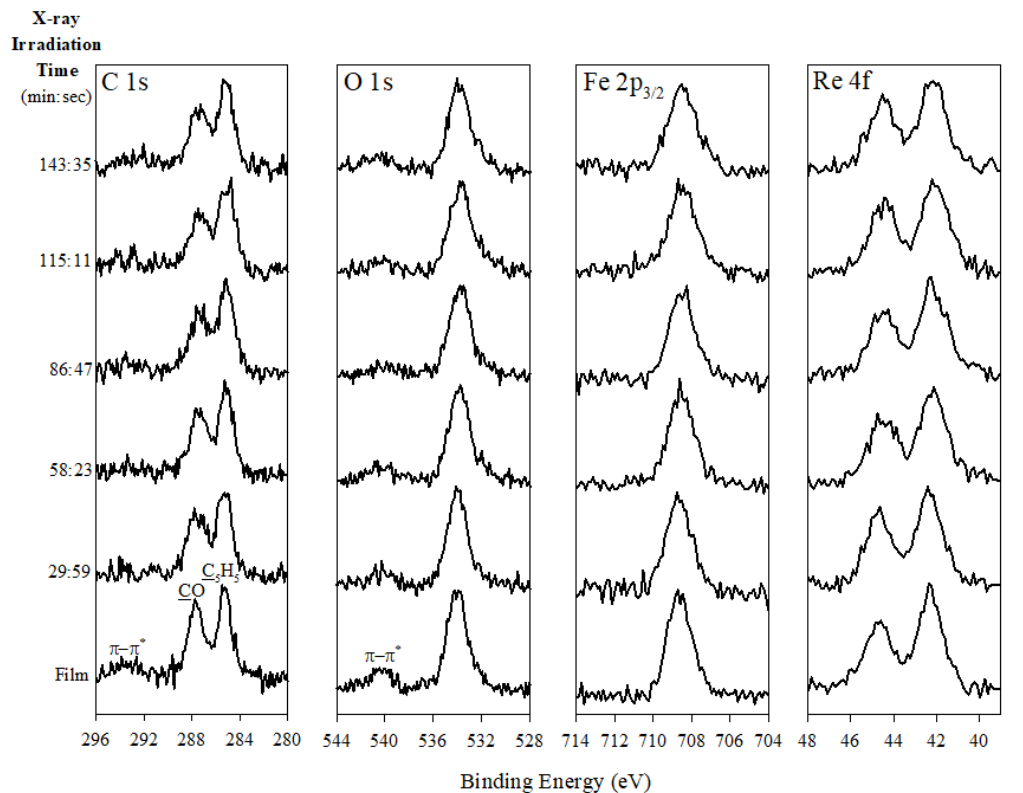
Figure 3.7: Evolution of C (1s), O (1s), Fe (2p$_{3/2}$), and Re (4f) XPS regions of a 2.1 nm CpFe(CO)$_2$Re(CO)$_5$ thin film upon X-ray irradiation with Mg Kα X-rays. The bottom set of spectra represents the adsorbed film prior to electron irradiation. Each set of spectra represents approximately 28.5 minutes of additional X-ray irradiation; total irradiation time is indicated on the left of each set of spectra.

a 4f$_{7/2}$/4f$_{5/2}$ doublet at 42.3 eV and 44.6 eV, respectively. Thus, the XPS data indicate that CpFe(CO)$_2$Re(CO)$_5$ adsorbs molecularly. Figure 3.7 also shows that the CpFe(CO)$_2$Re(CO)$_5$ films were unchanged by X-rays for the irradiation times needed to acquire XP spectra.

The mass spectra of volatile fragments ejected from the substrate upon electron irradiation (top) and argon ion irradiation (middle), are shown in Figure 3.8. The bottom panel shows the mass spectrum of CpFe(CO)$_2$Re(CO)$_5$
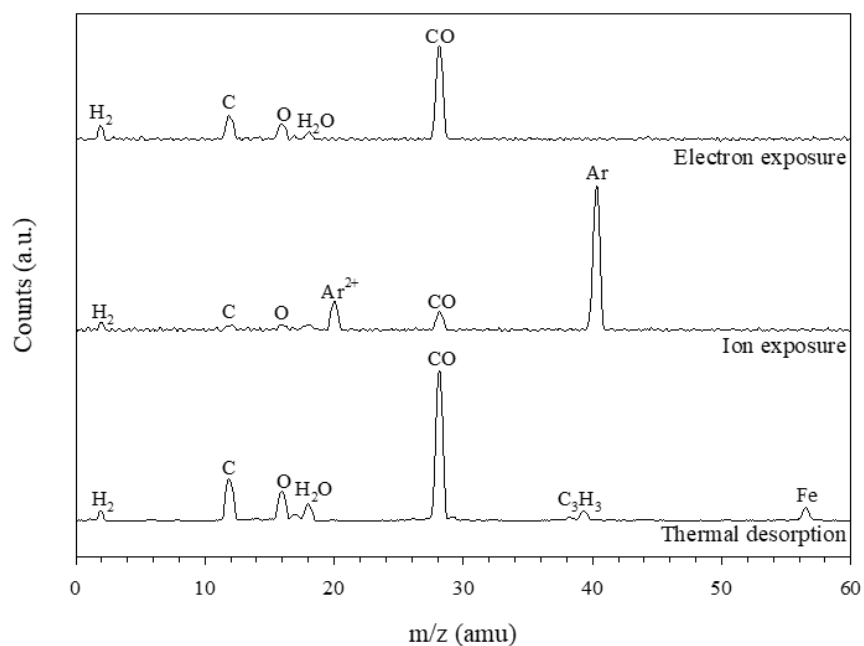
Figure 3.8: Representative mass spectra (0 - 60 amu) of volatile fragments desorbing from ≈ 1.5 - 2.0 nm thin films of adsorbed $CpFe(CO)_2Re(CO)_5$ as a result of exposure to 500 eV electron irradiation (top) and 800 eV Ar^+ bombardment (middle). These mass spectra presented here were taken during the first few seconds of exposure to electrons or ions, and the masses observed can be considered representative of all mass spectra taken during the initial regime of electron ($\approx$ 6 mC/cm^2) or argon ion ($\approx$ 0.048 mC/cm^2) exposure. For comparison, a mass spectrum showing thermal desorption of an adsorbed film of $CpFe(CO)_2Re(CO)_5$ is also shown (bottom).

molecules as they thermally desorb from the gold surface. In addition to residual hydrogen (m/z = 2) and water (m/z = 18) in the UHV chamber, which are present in all three mass spectra, the mass spectrum of the molecules as they thermally desorb exhibits a fragmentation pattern that is indicative of $CpFe(CO)_2Re(CO)_5$, with peaks at m/z = 12, 16, and 28 that can be associated with the CO ligands, as well as smaller peaks at m/z = 39 and 56 associated with the cyclopentadienyl ligand8 and iron, respectively. Under the influence

of electron irradiation (top), the mass spectrum consists of new peaks at m/z = 12, 16, and 28, indicative of CO. During argon ion irradiation, the mass spectrum (middle) is dominated by Ar^+ and Ar^{2+} peaks at m/z = 40 and 20, respectively, although peaks at m/z = 12, 16, and 28 associated with CO are also observed. It should be noted that the absolute intensities of the desorbing fragments during electron and Ar^+ ion irradiation cannot be directly compared due to different geometries and distances between the sample and mass spectrometer in the two experiments.
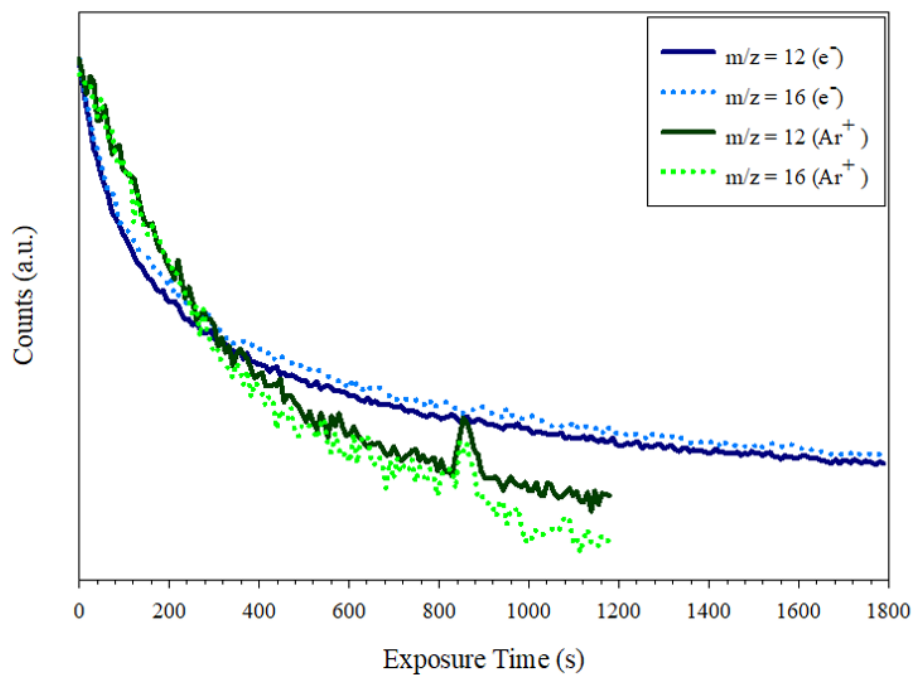
Figure 3.9: Normalized decay profiles of C (m/z = 12) and O (m/z = 16) during electron irradiation (dark blue solid line and light blue dotted line, respectively) and during argon ion bombardment (dark green solid line and light blue dotted line, respectively). The current density during electron irradiation was 5 $\mu A/cm^2$, while the current density during argon ion bombardment was found to be about 40 nA/cm^2.
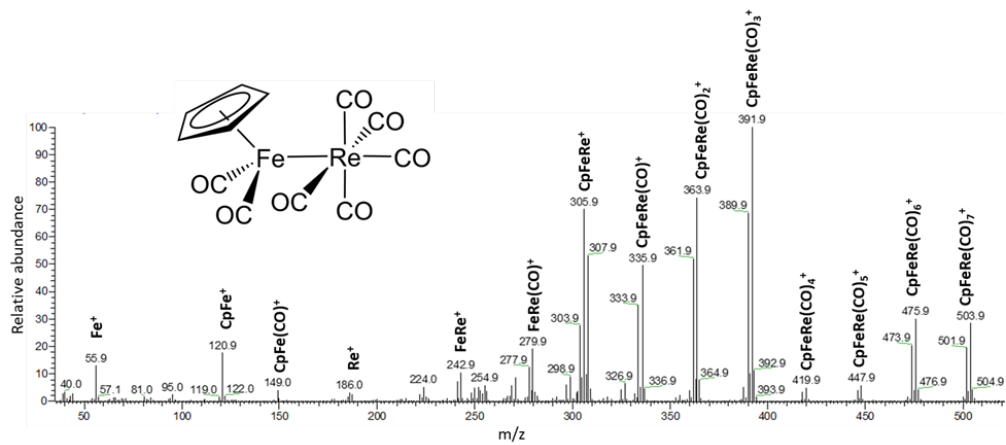
Figure 3.10: DIP/EI mass spectrum of $CpFe(CO)_2Re(CO)_5$ at 70 eV.
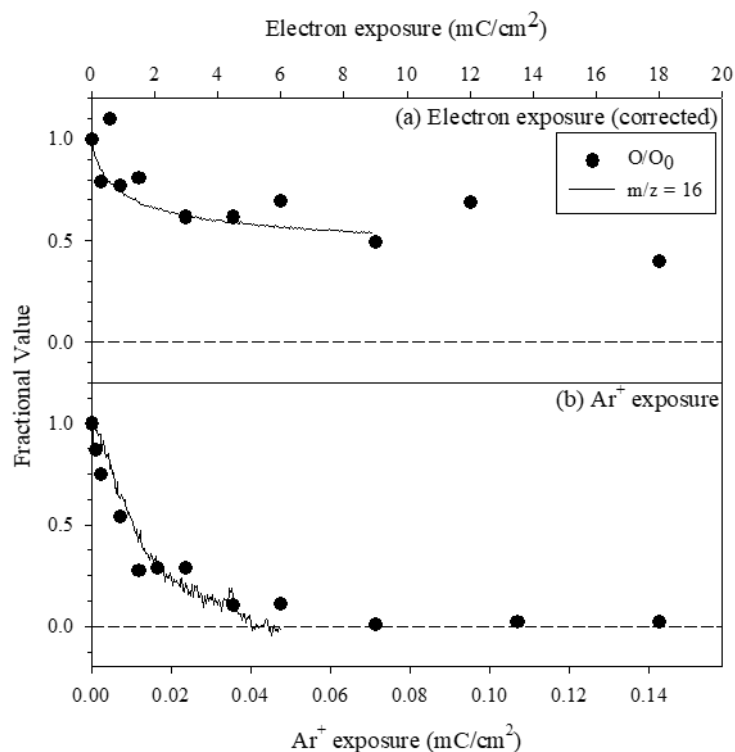
Figure 3.11: Kinetics of gas phase CO evolution from $\approx 1.5 - 2.0$ nm thin films of adsorbed CpFe(CO)$_2$Re(CO)$_5$ upon 500 eV electron irradiation (top) and 800 eV Ar$^+$ bombardment (middle) as measured by the O (m/z = 16) peak (solid black line). For both electron and ion exposure the normalized O signal observed by mass spectrometry is overlaid with the concurrent change in fractional oxygen coverage as measured by the O (1s) XPS region (solid black circles). For electron irradiation, the CO (O) signal observed by mass spectrometry has been corrected by an offset so that the desorption trace only represents those CO molecules which desorb (the latter determined by XPS).
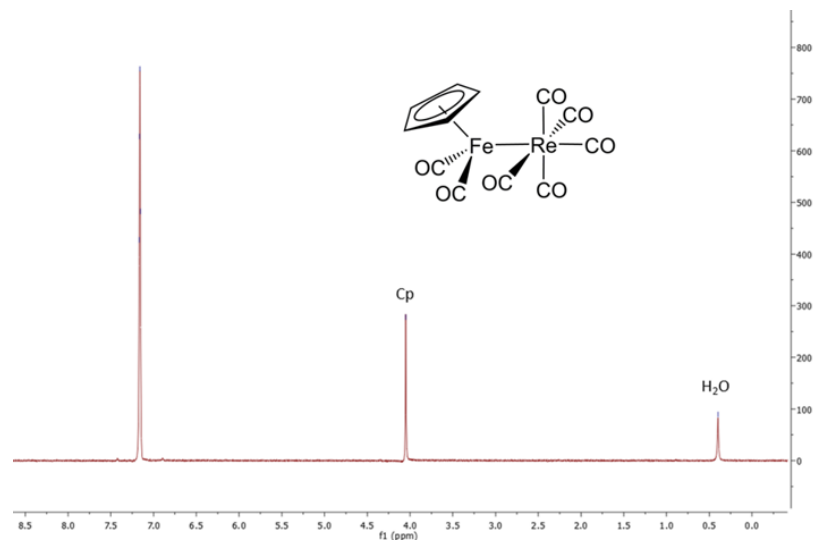
Figure 3.12: ^{1}H-NMR spectrum of CpFe(CO)$_2$Re(CO)$_5$ in benzene-d_6.
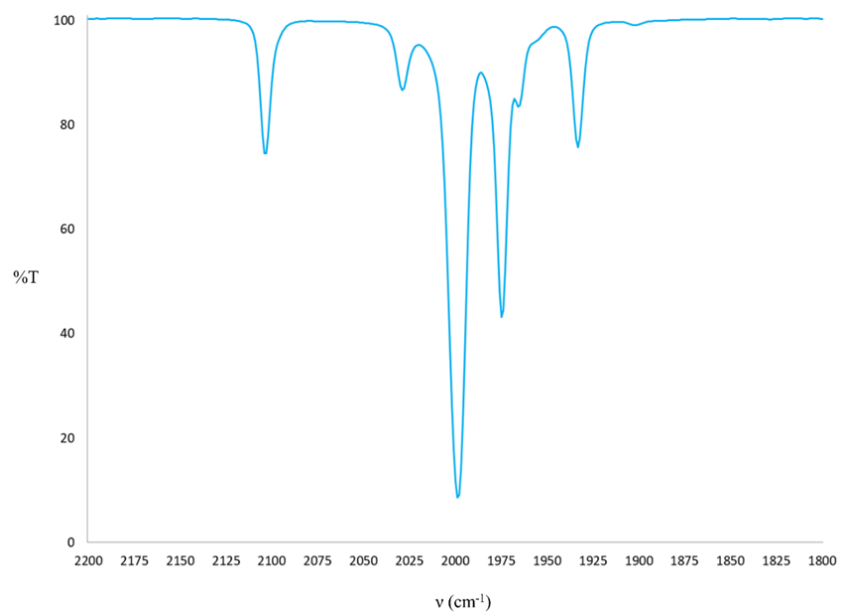
Figure 3.13: FT-IR spectrum of CpFe(CO)$_2$Re(CO)$_5$ in hexane.

References

[1] I. Utke, P. Hoffmann, J. Melngailis, *Journal of Vacuum Science & Technology B: Microelectronics and Nanometer Structures* **2008**, *26*, 1197.

[2] J. Melngailis, *Journal of Vacuum Science & Technology B: Microelectronics and Nanometer Structures* **1987**, *5*, 469.

[3] I. Utke, A. Gölzhäuser, *Angewandte Chemie International Edition* **2010**, *49*, 9328–9330.

[4] R. Córdoba, D. Mailly, R. O. Rezaev, E. I. Smirnova, O. G. Schmidt, V. M. Fomin, U. Zeitler, I. Guillamón, H. Suderow, J. M. De Teresa, *Nano Letters* **2019**, *19*, 8597–8604.

[5] R. Winkler, J. D. Fowlkes, P. D. Rack, H. Plank, *Journal of Applied Physics* **2019**, *125*, 210901.

[6] R. M. Thorman, R. K. T. P., D. H. Fairbrother, O. Ingólfsson, *Beilstein Journal of Nanotechnology* **2015**, *6*, 1904–1926.

[7] W. F. van Dorp, C. W. Hagen, *Journal of Applied Physics* **2008**, *104*, 081301.

[8] E. Böhler, J. Warneke, P. Swiderek, *Chemical Society Reviews* **2013**, *42*, 9219–9231.

[9] J. A. Spencer, J. A. Brannaka, M. Barclay, L. McElwee-White, D. H. Fairbrother, *The Journal of Physical Chemistry C* **2015**, *119*, 15349–15359.

[10] J. A. Spencer, Y.-C. Wu, L. McElwee-White, D. H. Fairbrother, *Journal of the American Chemical Society* **2016**, *138*, 9172–9182.

[11] I. Unlu, J. A. Spencer, K. R. Johnson, R. M. Thorman, O. Ingólfsson, L. McElwee-White, D. H. Fairbrother, *Physical Chemistry Chemical Physics* **2018**, *20*, 7862–7874.

[12] S. G. Rosenberg, M. Barclay, D. H. Fairbrother, *The Journal of Physical Chemistry C* **2013**, *117*, 16053–16064.

[13] S. G. Rosenberg, M. Barclay, D. H. Fairbrother, *Physical Chemistry Chemical Physics* **2013**, *15*, 4002–4015.

[14] K. Landheer, S. G. Rosenberg, L. Bernau, P. Swiderek, I. Utke, C. W. Hagen, D. H. Fairbrother, *The Journal of Physical Chemistry C* **2011**, *115*, 17452–17463.

[15] R. K. T. P., I. Unlu, S. Barth, O. Ingólfsson, D. H. Fairbrother, *The Journal of Physical Chemistry C* **2018**, *122*, 2648–2660.

[16] R. K. T. P., P. Weirich, L. Hrachowina, M. Hanefeld, R. Bjornsson, H. R. Hrodmarsson, S. Barth, D. H. Fairbrother, M. Huth, O. Ingólfsson, *Beilstein Journal of Nanotechnology* **2018**, *9*, 555–579.

[17] A. D. Dubner, A. Wagner, J. Melngailis, C. V. Thompson, *Journal of Applied Physics* **1991**, *70*, 665–673.

[18] P. Chen, H. W. M. Salemink, P. F. A. Alkemade, *Journal of Vacuum Science & Technology B: Microelectronics and Nanometer Structures* **2009**, *27*, 2718.

[19] R. Córdoba, P. Orús, S. Strohauer, T. E. Torres, J. M. De Teresa, *Scientific Reports* **2019**, *9*, 14076.

[20] J. De Teresa, P. Orús, R. Córdoba, P. Philipp, *Micromachines* **2019**, *10*, 799.

[21] A. N. Mansour, R. A. Brizzolara, *Surface Science Spectra* **1996**, *4*, 345–350.

[22] M. A. Huels, P.-C. Dugal, L. Sanche, *The Journal of Chemical Physics* **2003**, *118*, 11168–11178.

[23] C. Olsen, P. A. Rowntree, *The Journal of Chemical Physics* **1998**, *108*, 3750–3764.

[24] P. Rowntree, P.-C. Dugal, D. Hunting, L. Sanche, *The Journal of Physical Chemistry* **2002**, *100*, 4546–4550.

[25] P. A. Rowntree, *Surface Science* **1997**, *390*, 70–78.

[26] R. M. Thorman, I. Unlu, K. Johnson, R. Bjornsson, L. McElwee-White, D. H. Fairbrother, O. Ingólfsson, *Physical Chemistry Chemical Physics* **2018**, *20*, 5644–5656.

[27] S. Engmann, M. Stano, Š. Matejčík, O. Ingólfsson, *Journal of Physics: Conference Series* **2012**, *388*, 52019.

[28] F. Zaera, *Langmuir* **1991**, *7*, 1188–1191.

[29] J Okal, W Tylus, L Kępiński, *Journal of Catalysis* **2004**, *225*, 498–509.

[30] A. Cimino, B. A. De Angelis, D. Gazzoli, M. Valigi, *Z. Anorg. Allg. Chem.* **1980**, *460*, 86–98.

[31] J. A. Burroughs, L. Hanley, *Analytical Chemistry* **1994**, *66*, 3644–3650.

[32] D. Brown, H. Lyons, R. Sane, *Inorg. Chim. Acta* **1970**, *4*, 621–625.

[33] D. Brown, H. Lyons, A. Manning, J. Rowley, *Inorg. Chim. Acta* **1969**, *3*, 346–350.

[34] M. Bruce, *International Journal of Mass Spectrometry and Ion Physics* **1968**, *1*, 157–190.

[35] D. Jones, R. Mawby, *Inorg. Chimica Acta* **1972**, *6*, 157–160.

[36] L. S. Sunderlin, R. R. Squires, *International Journal of Mass Spectrometry* **1999**, *182-183*, 149–161.

[37] A. Diefenbach, F. M. Bickelhaupt, G. Frenking, *Journal of the American Chemical Society* **2000**, *122*, 6449–6458.

[38] J. A. Dean, *Lange's handbook of chemistry*, 15th ed., McGraw-Hill, New York, **1999**.

[39] K. E. Lewis, G. P. Smith, *Journal of the American Chemical Society* **1984**, *106*, 4650–4651.

[40] B. Speetzen, S. R. Kass, *The Journal of Physical Chemistry A* **2019**, *123*, 6016–6021.

[41] S. Fliszár, *Atomic Charges, Bond Properties, and Molecular Energies*, John Wiley & Sons, Inc., Hoboken, NJ, USA, **2008**.

[42] D.-H. Sun, B. E. Bent, J. G. Chen, *Journal of Vacuum Science & Technology A: Vacuum Surfaces and Films* **2002**, *15*, 1581–1585.

[43] E. T. Ada, L. Hanley, *International Journal of Mass Spectrometry and Ion Processes* **1998**, *174*, 231–244.

[44] E. R. Williams, G. C. Jones, L. Fang, R. N. Zare, B. J. Garrison, D. W. Brenner, *Journal of the American Chemical Society* **1992**, *114*, 3207–3210.

[45] J. A. Spencer, M. Barclay, M. J. Gallagher, R. Winkler, I. Unlu, Y.-C. Wu, H. Plank, L. McElwee-White, D. H. Fairbrother, *Beilstein Journal of Nanotechnology* **2017**, *8*, 2410–2424.

[46] F Porrati, R Sachser, M Huth, *Nanotechnology* **2009**, *20*, 195301.

[47] H Wu, L. A. Stern, D. Xia, D. Ferranti, B. Thompson, K. L. Klein, C. M. Gonzalez, P. D. Rack, *Journal of Materials Science: Materials in Electronics* **2014**, *25*, 587–595.

[48] R. D. Adams, M. Huang, *Organometallics* **1995**, *14*, 4535–4541.

[49] J. D. Wnuk, J. M. Gorham, S. G. Rosenberg, W. F. van Dorp, T. E. Madey, C. W. Hagen, D. H. Fairbrother, *The Journal of Physical Chemistry C* **2009**, *113*, 2487–2496.

[50] J. D. Wnuk, S. G. Rosenberg, J. M. Gorham, W. F. van Dorp, C. W. Hagen, D. H. Fairbrother, *Surface Science* **2011**, *605*, 257–266.

[51] S. G. Rosenberg, K. Landheer, C. W. Hagen, D. H. Fairbrother, *Journal of Vacuum Science & Technology B: Microelectronics and Nanometer Structures* **2012**, *30*, 051805.

[52] M. P. Seah, T. S. Nunney, *Journal of Physics D: Applied Physics* **2010**, *43*, 253001.

[53] W. Kern, J. L. Vossen, *Thin Film Processes II*, Academic Press, San Diego, **1991**, pp. 1–866.

Chapter 4

Electron and ion-induced reactions of Ru(CO)$_4$I$_2$

This work is adapted from the following submitted paper:

R. M. Thorman, P. A. Jensen, J.-C. Yu, S. J. Matsuda, L. McElwee-White, O. Ingólfsson, and D. Howard Fairbrother, Electron-induced reactions of Ru(CO)$_4$I$_2$: gas phase, surface, and FEBID, *submitted*, **2020**.

Sections 4.3.4 and 4.4.2 were additionally co-written with E. Bilgilisoy.

4.1   Introduction

Focused electron beam induced deposition (FEBID) is a maskless, direct-write nanofabrication technique, which can be used to make three dimensional nanoscale structures on nonplanar substrates.[1–4] Utilizing the narrow focus of a high energy (1-30 keV) electron beam to create nanostructures, a lateral resolution of 3 nm has been achieved.[5] FEBID takes a fairly simple approach to creating and modifying nanostructures on a surface, making it an important technique for prototyping nanostructures for applications in

nanoelectronics,[6] nanomagnetics,[7, 8] nanooptics, plasmonics,[9, 10] superconductors,[11, 12] and sensing devices.[13–15] FEBID has also been used commercially to fabricate tips for magnetic force microscopy[16] and in the repair of photolithographic masks.[17] Deposition of Ru with FEBID could also be of importance to extreme ultraviolet lithography (EUVL), where Ru is used as a capping layer in the EUVL masks.[18]

In FEBID, a gaseous organometallic precursor is introduced into a high vacuum chamber equipped with a high energy electron beam. The tightly focused electron beam, with typical energies between 1 and 30 keV, impacts the substrate, creating a plume of secondary electrons which react with adsorbed precursor molecules to form a deposit. In the ideal situation, the precursor compound fully dissociates under the area of the tightly focused electron beam, and the dissociated ligands are volatile enough to readily desorb from the surface, leaving a highly pure metallic deposit. However, current FEBID precursors are generally chosen from compounds developed for chemical vapor deposition (CVD), which is a thermally driven process rather than an electron-driven process. Due to being optimized for a different type of chemistry, some of the most common CVD precursors, e.g. $MeCpPtMe_3$,[19–21] lead to incomplete decomposition and low-metal purity deposits.

Much of the contamination of the deposit is derived from interactions between the precursor molecules and low energy secondary electrons (SEs) generated by inelastic scattering of the high energy electrons from the focused beam within the substrate and at its surface. The energy range of the secondary electrons is typically defined as $0 - 100$ eV.[2, 22–25] Furthermore,

interactions with low energy electrons (LEEs) are generally considered to be the driver for initial deposit formation and can lead to significant fragmentation but typically do not result in complete ligand loss, leading to organic contamination in the deposit.[19, 20, 26–28] Therefore, it is important to have a detailed understanding of how LEEs interact with potential FEBID precursors.

There are four distinct processes that can lead to fragmentation upon interaction between LEEs and molecules:[29]

Dissociative ionization (DI):
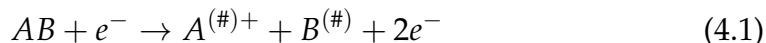
$$AB + e^- \rightarrow A^{(\#)+} + B^{(\#)} + 2e^- \tag{4.1}$$

Dissociative Electron Attachment (DEA):

$$AB + e^- \rightarrow [AB]^{(\#)-} \rightarrow A^{(\#)-} + B^{(\#)} \tag{4.2}$$

Neutral Dissociation (ND):

$$AB + e^-(\epsilon_1) \rightarrow [AB]^* + e^-(\epsilon_2 < \epsilon_1) \rightarrow A^{(\#)} + B^{(\#)} + e^-(\epsilon_2 < \epsilon_1) \tag{4.3}$$

Dipolar Dissociation (DD):

$$AB + e^-(\epsilon_1) \rightarrow [AB]^* + e^-(\epsilon_2 < \epsilon_1) \rightarrow A^{(\#)+} + B^{(\#)-} + e^-(\epsilon_2 < \epsilon_1) \tag{4.4}$$
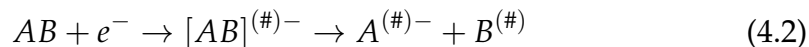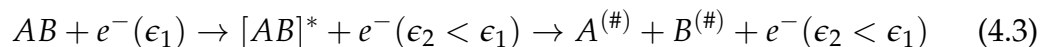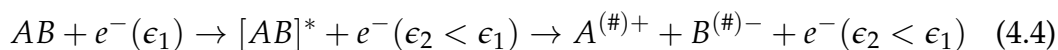
Here the hash (#) indicates that the molecule or fragment may be in an electronically and/or vibrationally excited state and the star (*) signifies that the molecule is in an electronically excited state. Dissociative ionization (Eq. 4.1) leads to a positively charged fragment and one or more neutral, generally radical fragments. It is a non-resonant process, generally with an onset slightly above the ionization threshold of the precursor molecule. The total cross section then increases with increasing incident electron energy

until reaching a maximum, usually between 50 and 100 eV, before leveling off. As the energy of the electrons increases, the branching ratio shifts in favor of multiple bond ruptures. Neutral dissociation (Eq. 4.3) exhibits a similar threshold behavior to DI, but the onset is defined by the lowest anti-bonding electronic excitation above the dissociation limits of the respective bonds. It leads to two or more neutral fragments, which are usually radicals. Dipolar dissociation (Eq. 4.4) proceeds in a similar manner to ND, but results in a negatively and a positively charged fragment. It is less efficient than both DI and DEA and is also expected to be less efficient that ND. This is attributed to the Coulomb interaction of the two oppositely charged fragments.

Dissociative electron attachment (Eq. 4.2) is, in contrast to the other processes discussed above, a resonant process. A transient negative ion is formed through electron attachment, which then relaxes through dissociation, forming a stable negative ion and one or more neutral (radical) fragments. The attachment proceeds in a narrow energy range defined by the Franck-Condon overlap between the neutral ground state and the negative potential energy surfaces of the respective anionic states formed in the process. Attachment is most efficient around 0 eV incident electron energy, and DEA is generally also most efficient at 0 eV as long as the respective processes are exothermic. Furthermore, DEA predominantly leads to specific bond breakage, forming a stable negative ion and a neutral radical. Each of the low energy electron processes described above (Eq. 4.1 – 4.4) may contribute to the reactions that occur in FEBID, where the efficiency of each channel is expected to reflect a convolution of the energy dependence of the cross sections for the individual

processes and the energy distribution of the available secondary LEEs.[23, 30]

Unfortunately, it is not possible to directly study the effects of the secondary LEEs *in situ* in FEBID because precursor molecules are subjected simultaneously to a range of secondary electrons with different energies. However, a combination of gas phase and surface science studies can provide insight into these processes. In current gas phase studies, an effusive beam of precursor molecules is crossed with a beam of LEEs of well-defined energy, under single collision conditions and the reaction products are monitored with a mass spectrometer.[29, 31–33] Such studies can provide well-resolved information on LEE-induced reactions with precursor molecules, including accurate assessments of the branching ratios for individual DEA and DI fragmentation pathways and absolute cross sections.[19]

However, the single collision conditions of gas phase experiments do not necessarily reflect the dissociation pathways of the same precursor molecules when interacting with a substrate. In order to gain more insight into the interactions of LEEs with precursors in FEBID, UHV surface studies are performed wherein a film of adsorbed precursor molecules is subjected to a beam of 500 eV electrons. The fragments desorbing from the surface during electron irradiation are monitored with a mass spectrometer, while changes in the deposit during electron irradiation have been studied using XPS, RAIRS, HREELS or a combination of the three.[34, 35] By comparing the gas phase and surface reactions of these precursor molecules, it is then possible to determine what type of interaction plays the largest role in the initial fragmentation of

the adsorbed molecule, and in what energy range the secondary LEEs contribute the most to contamination of the final deposit.[19] Comparative studies have been performed on a number of compounds, including MeCpPtMe$_3$,[19–21] Pt(PF$_3$)$_4$,[19, 27, 36–38] Co(CO)$_3$NO,[19, 34, 39] W(CO)$_6$,[19, 28, 40, 41] CpFe(CO)$_2$Mn(CO)$_5$,[42, 43] (η^3-C$_3$H$_5$)Ru(CO)$_3$Br,[44–46] Pt(CO)$_2$Cl$_2$,[47, 48] HFeCo$_3$(CO)$_{12}$,[49, 50] and HFeRu$_3$(CO)$_{13}$.[51] Through these comparative studies, it may be possible to identify the dominant initial dissociation mechanism. For example, for MeCpPtMe$_3$ adsorbed on a gold surface, the C:Pt ratio was observed to decrease from 9:1 to approximately 8:1, consistent with the single methyl loss observed in gas phase DEA measurements.[19–21] Conversely, for HFeRu$_3$(CO)$_{13}$, an average of 8-9 CO ligands were lost in the initial electron irradiation of the adsorbed compound. Gas phase measurements of this compound indicated an average CO-loss of 0.5 – 3 per incident for DEA and 3-9 per incident for DI, strongly suggesting that DI was the dominant initial dissociation mechanism.

Focused ion beam induced deposition (FIBID) is a similar charged particle beam-induced deposition technique that utilizes a tightly focused high energy ion beam, instead of an electron beam, to produce three dimensional nanostructures.[2, 52] In contrast to FEBID, there is relatively little present chemical understanding of the reactions underlying deposition in FIBID. Due to the significantly higher mass of ions as compared to electrons, there are many processes that may contribute to deposition in FIBID. This may include secondary electron-initiated processes similar to those that initiate deposition in FEBID, as well as collision-induced energy transfer between the primary

ions and the substrate, which produces energetic surface atoms that may decompose transiently adsorbed precursor molecules.[2, 53] Previous studies have correlated various parameters, such as secondary electron/sputtering yield and electronic/nuclear stopping power, with deposit growth rate as proxies for the secondary electron and collision-induced deposition models,[53–55] but this does not give insight into the chemistry that underlies the ion-induced deposition process. Thus, a study of low energy ion interactions with adsorbed organometallic precursor molecules similar to those previously performed with low energy electrons may allow the elucidation of the reactions that lead to deposition in FIBID. This sort of study has recently been used to compare the low energy electron- and ion-induced decomposition of adsorbed $CpFe(CO)_2Re(CO)_5$, demonstrating that low energy electrons and argon ions have markedly different reactions with that precursor.[56]

Here we present comparative DEA and DI gas phase and surface studies of a Ru-containing organometallic molecule, $Ru(CO)_4I_2$, and evaluate its potential as a FEBID precursor. Ruthenium has not previously been deposited at high purities,[46] possibly due to use of precursors with significant carbon content (e.g. $(CpEt)_2Ru$ and $(\eta^3\text{-}C_3H_5)Ru(CO)_3Br$).[46, 57] Previous studies of CO-containing precursors have shown that several CO ligands may desorb in the initial electron-mediated deposition step.[58] Further, surface science experiments have shown that while halide ligands do not desorb during the initial electron-induced event, it is sometimes possible to remove them from surface layers of deposits by sustained electron irradiation (e.g. Cl removal from $Pt(CO)_2Cl_2$).[47, 59] Halides can also be removed post-deposition,

e.g. through thermal processing,[58] by subsequent exposure to atomic hydrogen,[59] or by annealing under forming gas.[46] These results suggest that FEBID using $Ru(CO)_4X_2$ may be a route to produce pure ruthenium deposits. Additionally, complementary surface studies of the low energy (860 eV) Ar^+-induced decomposition of adsorbed $Ru(CO)_4I_2$ are compared to the electron-induced decomposition studies, showing that that the two processes are distinctly different. Finally, a kinetic study of the Ar^+-induced decomposition of adsorbed $Ru(CO)_4I_2$ is used to show that FIBID using $Ru(CO)_4I_2$ may also be a route to produce pure ruthenium deposits.

4.2   Experimental methods

Synthesis

General. Unless otherwise stated, all reactions were carried out under an inert atmosphere (N_2) using standard Schlenk techniques. Unless otherwise specified, all reagents were purchased from Sigma-Aldrich and used without further purification. $Ru_3(CO)_{12}$ was purchased from Acros Organics and iodine was purchased from Scientific. Solvents were purified using a MBraun MB-SP solvent purification system and stored over 4 Å molecular sieves.

^{1}H and ^{13}C NMR spectra were obtained on either a 300 MHz Mercury or 500 MHz Inova Varian instrument. Peaks were referenced to the residual protons of the deuterated solvents. IR spectra were obtained on a PerkinElmer Spectrum One FT-IR Spectrometer using a solution cell equipped with NaCl windows and a path length of 1.0 mm. Thermogravimetric analysis was performed on a TA Instrument Q5000. The samples were ramped from 20

°C to 600 °C at a rate of 10 °C/min under N_2. Mass spectra were obtained on either an Agilent 6220 TOF mass spectrometer using DART-TOF mode of operation or a ThermoScientific DSQ II mass spectrometer using DIP-NCI/EI-MS mode of operation.

Ru(CO)$_4$I$_2$. The compound was synthesized using modified literature procedures.[60–62] A solution of $Ru_3(CO)_{12}$ (178.2 mg, 0.2787 mmol) and hexanes (400 mL) was prepared in a 500 mL Schlenk flask. The solution was purged with hexanes saturated with CO for approximately 10 min. The reaction was subsequently irradiated with a blue LED light (450-455 nm, 15 W) while continuing to CO purge for approximately 20 min until the solution turned clear. The solution was then purged with N_2 to remove residual CO present in solution. The solution was cooled to -40 °C using an acetonitrile dry ice cooling bath. A cooled solution of iodine (246.8 mg, 0.9724 mmol) in hexanes (50 mL) was added in one lot to the reaction flask via a syringe. A yellowish-brown solid precipitated immediately. Solvent was removed under vacuum and a yellow-orange solid remained. The solid was sublimed at 65 °C at 125 mTorr. Crude yield: 208.7 mg, 53.4%. Yield after sublimation: 170.1 mg, 43.6%. The compound was characterized by comparison to literature data.[60, 61] IR (hexanes): 2158 (m), 2105 (vs), 2095 (s), 2066 (s) cm^{-1}.

Ru(CO)$_4$Br$_2$. The compound was synthesized by a modification of reported literature procedures.[60–62] A three-necked round bottom flask was equipped with a nitrogen-inlet adapter, a stopper and a septum. $Ru_3(CO)_{12}$ (300 mg, 0.47 mmol) was measured and added to the flask, then mixed with

anhydrous hexanes (500 mL) to create a 6×10^{-4} M $Ru_3(CO)_{12}$ hexanes solution. The solution was irradiated by blue LED light (450-455 nm, 15 W) in the presence of carbon monoxide gas, with a vent needle in the septum during this process. The $Ru(CO)_5$ colorless intermediate was formed during photoexcitation of $Ru_3(CO)_{12}$ with the blue LED light. After the reaction mixture had become colorless, the blue LED light was turned off and the CO gas input was stopped. The reaction mixture was purged with N_2 gas for 10 min to make sure no CO remained in the reaction flask, while the reaction mixture was cooled to -40 °C by using an acetonitrile/dry ice bath. Bromine (2.9 mL, 1.4 mmol) was dissolved in anhydrous hexanes to produce a dilute bromine solution with a concentration of 0.488 M. Under air free conditions, the Br_2 hexanes solution was injected into the cold $Ru(CO)_5$ solution. The colorless hexanes solution turned light yellow and *cis*-$Ru(CO)_4Br_2$ precipitated out as a pale yellow powder (380 mg, 72 %). Most of the hexanes were removed by cannula transfer, then the rest of the hexanes were removed under vacuum. IR (CCl$_4$): νCO 2176, 2123, 2105, 2072 cm^{-1}. The product sublimed as pale-yellow particles at 38 ± 0.5 °C under 125 mTorr with the chiller at 11 °C. The product was crystalized by dissolving the crude *cis*-$Ru(CO)_4Br_2$ in DCM, then slowly adding heptane in the same vial. Crystals formed overnight under room temperature.

Gas phase measurements

The gas phase DEA experiments were carried out at the University of Iceland using a crossed-beam instrument, which has been described in detail previously.[33] Here, only a brief description of the experiments will be given.

The instrument is under high vacuum, with a base pressure of roughly 7-8 x 10^{-9} Torr. $Ru(CO)_4I_2$ is heated to approximately 50-60 °C and sublimed into the chamber through a capillary to create an effusive molecular beam in the reaction zone. Details on the inlet systems have been published previously.[48] During experiments the pressure was kept constant at approximately 2-4 x 10^{-7} Torr as monitored with an ion gauge placed at some distance from the reaction zone. The molecular beam is crossed by a well-defined, monochromatic electron beam generated using a trochoidal electron monochromator (TEM). The electron energy was calibrated with reference to the well-established 0 eV resonance for SF_6^- from SF_6 and the energy resolution was estimated from the full width at half maximum (FWHM) of the SF_6^- ion yield.[63] The electron energy resolution in the present experiments was 110-120 meV. The temperature of the TEM was kept at 120 °C by two halogen lamps in order to prevent deposition of the target compound on the components of the electronic lens system. The ions generated in the reaction zone were analyzed with a commercial HIDEN Epic 1000 quadrupole mass spectrometer (QMS). Mass spectra were recorded by scanning through the relevant mass range at a fixed electron impact energy while ion yield curves were recorded by scanning through the electron energy at fixed mass.

Gas phase DI spectra were obtained at the University of Florida, using a ThermoScientific DSQ II with electron impact ionization (70 eV) with an ion source temperature of 100 °C. Samples were introduced using a direct insertion probe (DIP). The tip of a stainless-steel GC-style 10 μL syringe was used to transfer some of the dry sample to the DIP vial. The probe ran the

following temperature program: 30 – 300 °C at a ramp rate of 30 °C/min; hold 1 min at 300 °C.

Surface Science Studies

Surface science experiments were performed in an ultra-high vacuum (UHV) chamber equipped with an X-ray photoelectron spectrometer (XPS), quadrupole mass spectrometer (QMS), electron flood gun, and ion gun described in more detail elsewhere.[21, 64, 65] The UHV chamber has a base pressure below 4 x 10^{-9} Torr. The compound was placed in a reservoir, which was attached to the UHV chamber via a leak valve. The compound was heated to 35 – 40 °C and introduced into the UHV chamber, wherein it adsorbed onto a cooled gold substrate ($\approx$ -100 °C) and formed thin films of approximately 1.3 – 1.9 nm thickness, as measured by XPS.

X-ray photoelectron spectroscopy was performed *in situ* with a PHI 5400 XPS using a Mg Kα X-ray anode. Spectra were calibrated to the substrate Au $4f_{7/2}$ peak (BE = 84.0 eV)[66] and processed using commercially available software (CasaXPS). Mass spectrometry performed during surface science experiments used a Balzers Prisma QMS.

The electron source used during all surface science experiments was a commercial flood gun (Specs FG 15/40). The energy of the flood gun was +480 eV and a +20 V bias was applied to the substrate during electron irradiation, producing an incident electron energy throughout all surface science experiments of +500 eV. The bias was used to ensure that all secondary electrons generated during electron irradiation remained on the substrate. A target current of 5 μA was maintained throughout all electron irradiation experiments. Electron

dose is reported in terms of both mC/cm^2 and e$^-$/cm^2; 1 x 10^{16} e$^-$/cm^2 = 1.6 mC/cm^2.

Ion bombardment was performed using a Perkin-Elmer PHI model 04-303 differentially pumped ion gun. The primary Ar$^+$ beam energy was 880 V, and the substrate was biased at +20 V to prevent the escape of secondary electrons, giving a relative beam energy of 860 V. Ion dose is reported here in terms of bombardment time (s), however, this may be directly related to current density. The ion gun was oriented at approximately 45° from the surface normal, giving a beam energy of approximately 600 V along the surface normal. The primary ion current density was calculated as discussed previously to be $\approx$ 40 nA/cm^2.[56]

Deposition Studies

Deposits were made by performing electron beam induced deposition (EBID) using an Auger spectrometer (PHI 15-155) on silicon substrates with both Ru(CO)$_4$I$_2$ and its brominated analog Ru(CO)$_4$Br$_2$ as precursors. The Auger spectrometer is housed in a UHV chamber (base pressure $\approx$ 3 − 4 x 10^{-9} Torr) equipped with a QMS (Stanford Research Systems − 200). The compound was heated to about 78 °C and introduced into the chamber via a UHV-compatible leak valve equipped with a directional doser used to improve the partial pressure of Ru(CO)$_4$I$_2$ at the silicon substrate surface. The EBID experiments were performed under steady state conditions using the electron gun in the Auger spectrometer, operating at a primary beam energy of 3 kV and an emission current of 2 mA. The system pressure was maintained at approximately 1 − 2 x 10^{-7} Torr during deposition, which

proceeded for 5 hours. Imaging and analysis of deposits was performed *ex situ* using a JEOL JSM-IT100 secondary electron microscope (SEM) with a 10 kV primary electron beam (8 nm resolution) and a JEOL-made energy-dispersive X-ray spectroscopy (EDX) unit. Deposit thickness was not quantified, but samples were thick enough to have minimal silicon substrate signal during EDX measurements with up to a 20 kV primary electron beam.

4.3   Results

4.3.1   Gas phase low-energy electron interactions

Figure 4.2 shows the pressure-normalized negative ion yield curves from DEA to $Ru(CO)_4I_2$ in the electron energy range from about 0 to 7 eV. The negative ion yields were measured up to 15 eV, but since no resonances were observed above 7 eV, only the low energy range is shown.

Negative ion fragments are observed at m/z = 440, 412, 384, 356, and 127 (Fig. 4.1, bottom), corresponding to the formation of $[M - CO]^-$, $[M - 2CO]^-$, $[M - 3CO]^-$, $[M - 4CO]^-$, and I^-, respectively, where M is the parent molecule. The most intense signal is that of $[M - 2CO]^-$, the formation of which has a relative cross section that is more than an order of magnitude higher than for any of the other fragments (Fig. 4.2). From the negative ion yield curves shown in Fig. 4.2, it is apparent that the fragments $[M - CO]^-$, $[M - 2CO]^-$ and I^- all appear through a narrow contribution peaking at 0 eV. This requires that all of these DEA processes are exothermic. We attribute all of these contributions to the same low-lying resonance, which is likely associated with the anionic ground state. The $[M - 3CO]^-$ contribution, which peaks

88
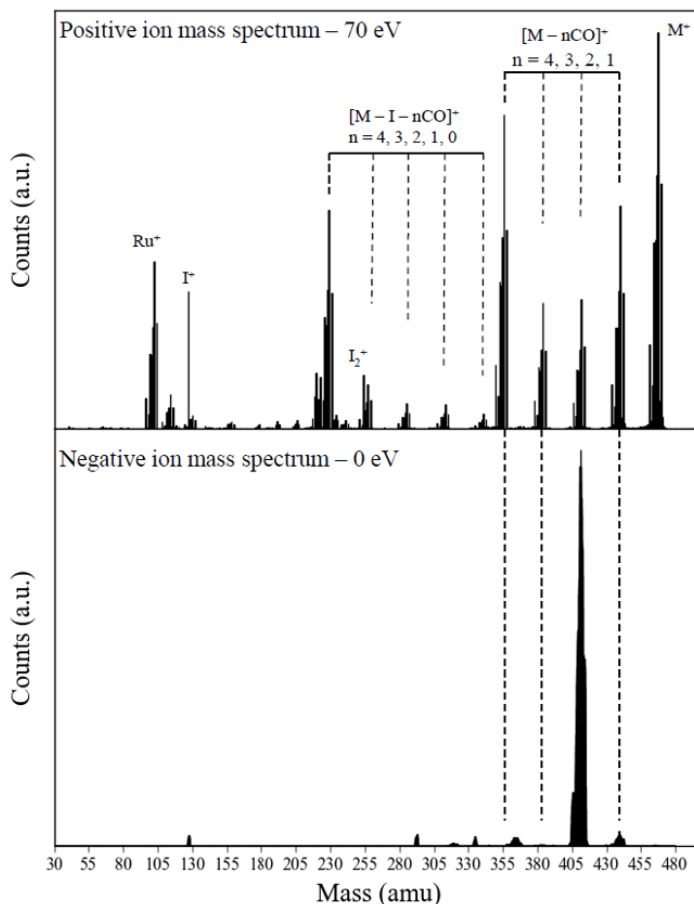
Figure 4.1: Mass spectra of Ru(CO)$_4$I$_2$: (Top) Positive ion fragments formed at 70 eV incident electron energy due to DI. There is a slight overlap between the I$_2^+$ (254 amu) peak and the [M - I - 3CO]$^+$ peak (257 amu), owing to the isotope distribution of ruthenium. (Bottom) Negative ion fragments formed at 0 eV incident electron energy due to DEA. The small peaks at roughly 292, 320, 334, and 364 amu are from impurities.

at about 0.5 eV, probably originates from the high energy tail of the same resonance, shifted due to the higher thermochemical threshold for this process. The DEA ion yield curve for the RuI$_2$ anion; [M - 4CO]$^-$, is also shown at the bottom of Fig. 4.2. The formation of this fragment is negligible through DEA, though a very small contribution may be anticipated around 4 to 5 eV.
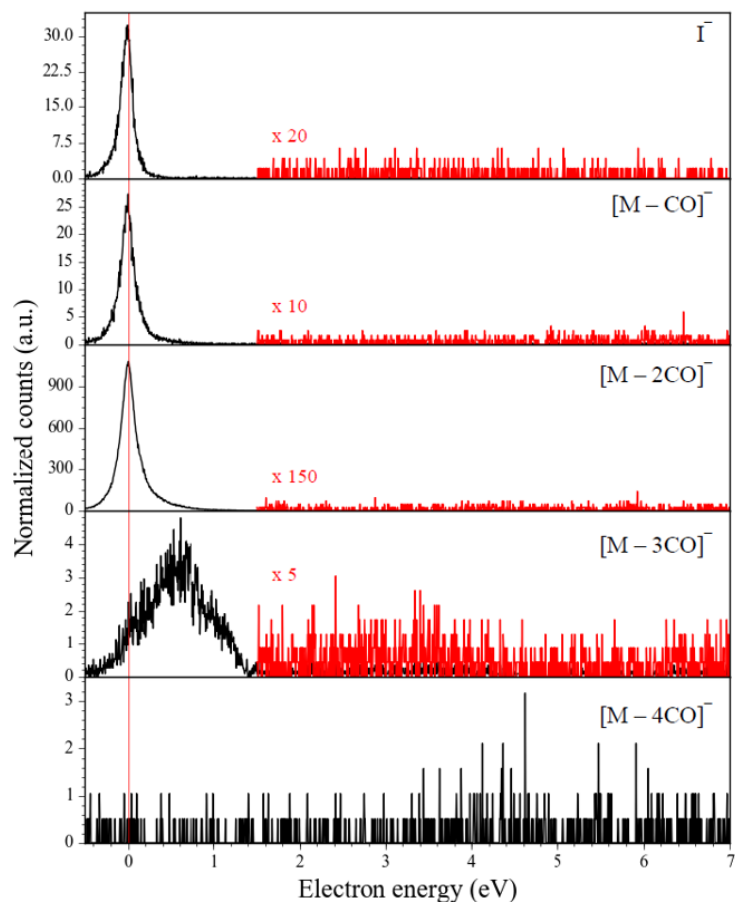
Figure 4.2: Pressure normalized negative ion yield for DEA to gas phase $Ru(CO)_4I_2$ from about 0 to 7 eV. The solid black line shows the yield of each fragment detected above the noise. The red line is a magnification of the high energy region.

The positive ion mass spectrum (Fig. 4.1, top panel) shows that DI produces much richer fragmentation than observed in DEA. Along with a significant contribution from the parent cation at m/z = 468, prominent fragments are observed at m/z = 440, 412, 384, 356, 254, 229, 127, and 101. These correspond to the carbonyl loss progression $[M - CO]^+$, $[M - 2CO]^+$, $[M - 3CO]^+$, and $[M - 4CO]^+$ and to the ions I_2^+, $[M - 4CO - I]^+$, I^+, and Ru^+, respectively.

Table 4.1: Relative yields of Ru-containing ions produced by gas phase DEA and DI of $Ru(CO)_4I_2$ and average CO and I loss per DEA and DI incident.

Fragment	Chemical Formula	m/z	Relative DEA Yield	Relative DI Yield
$[M - 4CO - 2I]^{+/-}$	Ru	101		202.8
$[M - 4CO - I]^{+/-}$	RuI	229		266.4
$[M - 4CO]^{+/-}$	RuI_2	356	0.4	351.8
$[M - 3CO]^{+/-}$	$Ru(CO)I_2$	384	1.2	89.7
$[M - 2CO]^{+/-}$	$Ru(CO)_2I_2$	412	100	100
$[M - CO]^{+/-}$	$Ru(CO)_3I_2$	440	2.2	133.1
$M^{+/-}$	$Ru(CO)_4I_2$	468		248.9
Average CO loss			1.99	2.79
Average I loss			0	0.48

Minor contributions from m/z = 341, 313, 285, and 257 are also observed, corresponding to loss of one I ligand along with sequential carbonyl loss ($[M - nCO - I]^+$; n = 0-3).

Table 4.1 lists the relative contributions of individual fragments obtained through DEA and DI to $Ru(CO)_4I_2$ and the average CO and I loss per DEA and DI incident, respectively. The relative DEA contributions were found by integrating the negative ion yield from -0.5 to 7.0 eV for each fragment (Fig. 4.2) and dividing that by the total negative ion yield within that energy range. For DI, the relative contributions of the observed fragments were found by integrating over the isotope distribution for each Ru-containing fragment in the positive ion mass spectrum and dividing that by the total positive ion yield of Ru-containing fragments. The relative contributions of each observed fragment listed in Table 4.1 are normalized to the $[Ru(CO)_2I_2]^{+/-}$ peak intensity, which is set at 100 for both the negative and positive ions.

The average CO and I loss per incident for each process was calculated by taking the sum of the relative contribution for each Ru-containing fragment multiplied by the number of CO or I ligands lost, and dividing that by the sum of the relative contributions of all Ru-containing fragments. Based on this analysis, DEA produces an average CO loss per ionization incident of 1.99 and DI produces an average CO loss of 2.79. The average I loss is negligible in DEA (corresponding only to I^- formation), but is close to 0.5 in DI.

4.3.2   Electron irradiation of Ru(CO)$_4$I$_2$ thin films

Figure 4.3 shows the evolution of the Ru(3d)/C(1s), O(1s), and I(3d$_{5/2}$) XPS regions of 1.3 – 1.9 nm thin films of adsorbed Ru(CO)$_4$I$_2$ upon irradiation with 500 eV electrons. X-ray sensitivity control studies (Figure 4.14) were performed in order to determine the impact of X-ray exposure on the adsorbed Ru(CO)$_4$I$_2$ thin films. The effect of X-ray irradiation was found to be similar to that of electron irradiation (albeit at a much slower rate), likely due to the secondary electrons generated by the interactions between the X-ray beam and the surface. Based on a comparison of Figs. 4.3 and 4.14, we estimate each set of XPS scans deliver an equivalent electron dose of 0.12 mC/cm^2 (0.78 x 10^{15} e$^-$/cm^2); all XPS figures and data have been adjusted to reflect this comparatively small "additional" electron dose imparted by X-ray irradiation.

The bottom spectra in Fig. 4.3 show the as-deposited Ru(CO)$_4$I$_2$ film prior to electron irradiation. Upon adsorption, the Ru(3d)/C(1s) region is characterized by three peaks: a doublet with peaks at approximately 283.1 and 287.2 eV, respectively corresponding to the Ru(3d$_{5/2}$) and Ru(3d$_{3/2}$) transitions,[45, 67]
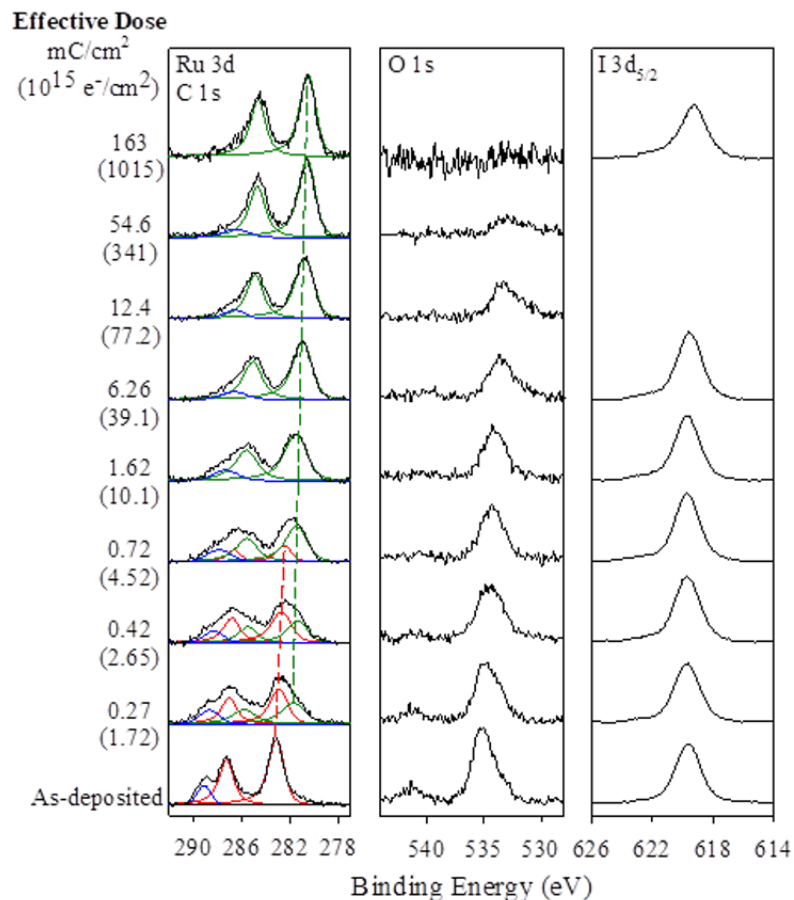
Figure 4.3: Evolution of the C(1s),/Ru(3d), O(1s), and I(3d$_{5/2}$) XPS regions of $\approx$ 1.3 - 1.9 nm Ru(CO)$_4$I$_2$ films upon irradiation with 500 eV electrons. The bottom spectrum represents the as-deposited, un-irradiated film. Speciation is shown in the C(1s)/Ru(3d) region, where the blue line represents C(1s), the red lines represent the Ru(3d) peaks associated with the Ru(CO)$_4$I$_2$ compound, and the green lines represent the Ru(3d) peaks associated with the species produced by electron irradiation. The dashed red and green lines in this region show the change in binding energy of these peaks during electron irradiation. Electron dose is shown on the left-hand side in units of mC/Cm^2 and, in parentheses, 10^{15} e$^-$/cm^2.

and a peak at approximately 289.1 eV corresponding to the CO C(1s).[45, 67]

A low intensity peak centered at approximately 294.3 eV corresponding to the

CO C(1s) π-π* transition is observed but not shown due to its low intensity.

93

The Ru($3d_{5/2}$) and Ru($3d_{3/2}$) transitions are fit as solid red curves, while the CO C(1s) peak is fit by a solid blue curve. The Ru($3d_{5/2}$) peak position at 283.1 eV is similar to previously reported ruthenium halide species.[45, 68] The O(1s) region is initially characterized by a main peak at approximately 535.2 eV and a lower intensity peak centered at 541.3 eV corresponding to the CO O(1s) π-π* transition, which is typical for adsorbed CO species.[45, 67] Finally, the unirradiated I($3d_{5/2}$) region is characterized by a single, symmetric peak at approximately 619.6 eV.

Upon electron irradiation, the C(1s)/Ru(3d) region broadens considerably to lower binding energies. The resultant spectral envelope can be fit by a combination of a C(1s) peak along with two sets of Ru($3d_{5/2}$)/($3d_{3/2}$) doublets. One of these doublets has peak positions corresponding to those of the parent compound (solid red curves) while the other doublet, associated with a species produced by electron irradiation, has Ru($3d_{5/2}$)/($3d_{3/2}$) peaks at approximately 281.5 and 285.7 eV, respectively (solid green curves). As the electron dose increases, the contribution of the Ru($3d_{5/2}$)/($3d_{3/2}$) doublet associated with the parent compound decreases steadily. After an electron dose of 1.6 mC/cm^2 (10.1 x 10^{15} e$^-$/cm^2), none of the parent Ru(CO)$_4$I$_2$ species remains. Over this same range of electron doses, the intensity of the Ru($3d_{5/2}$)/($3d_{3/2}$) doublet associated with the electron-irradiated species increases in intensity, while its peak binding energies decrease slightly with increasing electron dose. After an electron dose of 1.6 mC/cm^2 (10.1 x 10^{15} e$^-$/cm^2), the Ru(3d)/C(1s) region can be well-fit by a single Ru($3d_{5/2}$)/Ru($3d_{3/2}$) doublet with peaks at approximately 280.4 and 284.6 eV along with a C(1s) peak. For electron
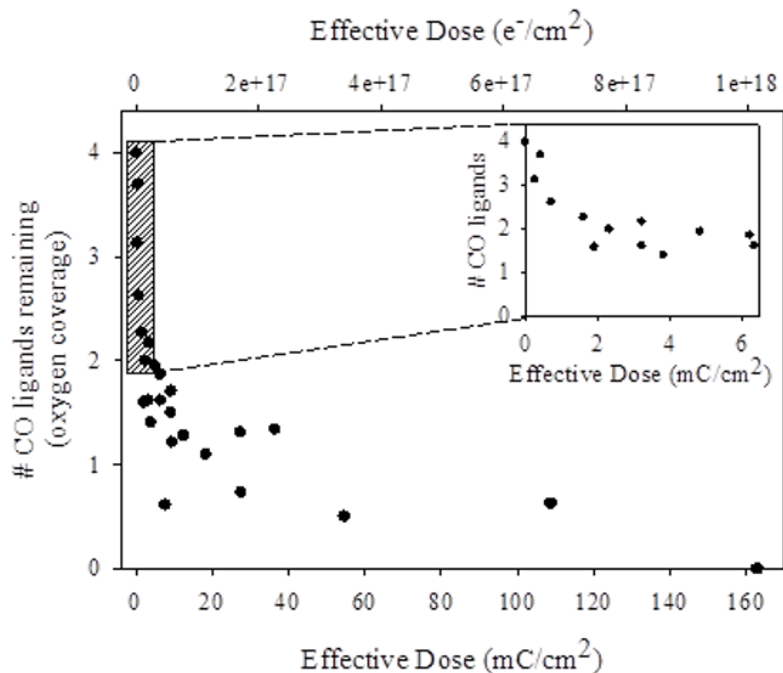
Figure 4.4: Number of CO ligands remaining (measured by the oxygen coverage) as a function of electron dose, for $Ru(CO)_4I_2$ films exposed to 500 eV electrons. Effective electron dose is expressed in units of mC/Cm^2 (main axis) and e^-/cm^2 (top axis). The highlighted region shows the CO ligand loss for electron doses < 6 mC/cm^2 (4×10^{16} e^-/cm^2).

doses > 1.6 mC/cm^2 (10.1×10^{15} e^-/cm^2), the Ru(3d) peak profile remains unchanged. Despite the change in Ru speciation, there is no change in the coverage of ruthenium atoms as a result of electron irradiation. In contrast, electron irradiation produces a steady decrease in the intensity of the C(1s) peak over the entire sequence of electron doses, with peak fitting suggesting that no carbon remains after an electron dose of 163 mC/cm^2 (1015×10^{15} e^-/cm^2).

Electron irradiation also causes the O(1s) peak to decrease in intensity, as well as broaden and shift to lower binding energy. After an electron dose

of 6.2 mC/cm^2 (39.1 x 10^{15} e$^-$/cm^2), the O(1s) region is characterized by a single broadened peak centered at 533.6 eV, a decrease in binding energy of about 1.6 eV compared to the parent compound. At greater electron doses (> 6.2 mC/cm^2, 39.1 x 10^{15} e$^-$/cm^2), the O(1s) peak continues to decrease in intensity, broaden, and shift to lower binding energy, as can be seen in Fig. 4.3. Ultimately, no oxygen is observed after an electron dose of 163 mC/cm^2 (1015 x 10^{15} e$^-$/cm^2). In contrast to the behavior in the Ru(3d)/C(1s) and O(1s) regions the I(3d$_{5/2}$) region does not change significantly during electron irradiation, indicating an absence of iodine desorption. However, determination of the fate of the Ru-I bond through detailed analysis of the I(3d$_{5/2}$), Ru(3d) and Au(4f) XPS regions is complicated by the similar electronegativities of iodine, ruthenium, and gold (2.66, 2.2 and 2.4, respectively). Consequently, dissociation of the Ru–I bond would not produce any changes in the I(3d$_{5/2}$) or Ru(3d) peak positions; subsequent formation of a gold iodide also would not change the I(3d$_{5/2}$) or Au(4f) peak positions. However, a previous study of electron-induced decomposition of Pt(CO)$_2$Cl$_2$, revealed that the chloride ligand did not dissociate from the platinum during the initial stage of electron-induced dissociation;[47] thus, we conclude that the Ru–I bond likely remains intact.

Figure 4.4 shows the change in the number of carbonyl ligands remaining on the surface, as measured by the O(1s) area, as a function of electron dose. Initially, 4 CO ligands are present in the adsorbed molecular Ru(CO)$_4$I$_2$ species. Upon electron irradiation, this quickly decreases to 50% of its initial value (i.e. loss of an average of 2 CO ligands/per parent molecule) after an electron

dose of about 6 mC/cm^2 (4 x 10^{16} e$^-$/cm^2). This initial CO loss regime is highlighted in the inset in Fig. 4.4. Larger electron doses lead to the loss of the remaining 2 CO ligands at a much slower rate, with no CO ligands remaining after an electron dose of about 160 mC/cm^2 (1 x 10^{18} e$^-$/cm^2).

The kinetics of electron-stimulated CO desorption during the initial regime of electron exposure (< 6 mC/cm^2, 4 x 10^{16} e$^-$/cm^2) of adsorbed Ru(CO)$_4$I$_2$ are shown in Figure 4.5. The inset shows a representative mass spectrum taken during electron exposure, with visible peaks at m/z = 12, 16, and 28 corresponding to C, O, and CO, respectively. The top graph shows the normalized evolution of gas phase CO, as observed by mass spectrometry using the C (m/z = 12) peak (solid black line). The bottom graph shows the concurrent change in fractional coverage of Ru(CO)$_4$I$_2$ (dark blue filled circles, left axis) determined by analysis of the Ru(3d) XPS region, overlaid with the number of CO ligands remaining on the surface (inverted light blue triangles, right axis), the latter determined by the change in the fractional oxygen coverage as measured by the O(1s) peak. Analysis of the top and bottom panels in Figure 4.5 reveals that the rates of CO desorption and loss of the parent Ru(CO)$_4$I$_2$, as well as the change in the number of CO ligands in the adsorbate, all follow the same kinetic profile as a function of the electron dose.

4.3.3 Electron beam induced deposition

Figure 4.6 shows representative EDX spectra from deposits made by exposing a silicon substrate to a high energy (3kV) electron beam in the presence of gas
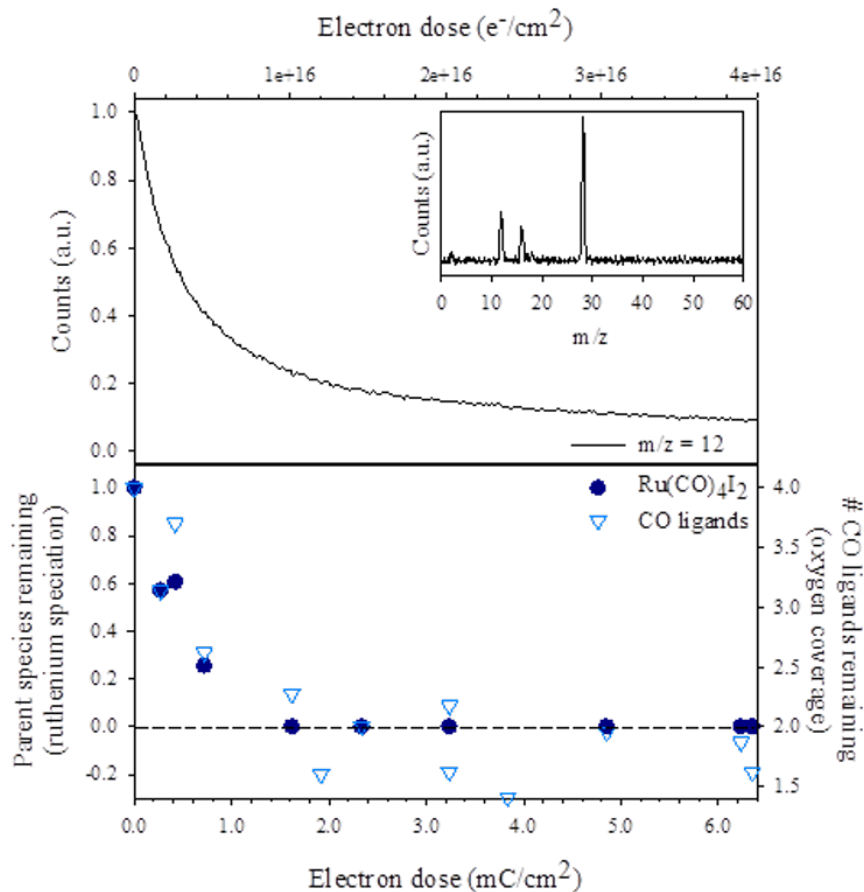
Figure 4.5: (Top) Kinetics of electron-stimulated gas phase CO desorption from $Ru(CO)_4I_2$ films upon irradiation with 500 eV electrons as measured via mass spectrometry by the normalized C (m/z = 12) peak intensity (solid black line). The inset shows a representative mass spectrum of volatile species during electron irradiation. (Bottom) The fractional concentration of the parent species, $Ru(CO)_4I_2$ (dark blue filled circles, left axis), as measured by the Ru (3d) XPS speaks (see Fig. 4.3) and the number of CO ligands remaining on the surface (light blue inverted triangles, right axis) as measured by the O(1s) XPS peak area (see Fig.4.3). Electron dose is expressed in units of mC/Cm^2 (main axis) and e^-/cm^2 (top axis).

phase $Ru(CO)_4I_2$ (top) and its brominated analog $Ru(CO)_4Br_2$ (bottom). The images to the right of each spectrum are SEM images of the respective deposits. The EDX analysis demonstrates that the $Ru(CO)_4I_2$ deposit (top) is composed
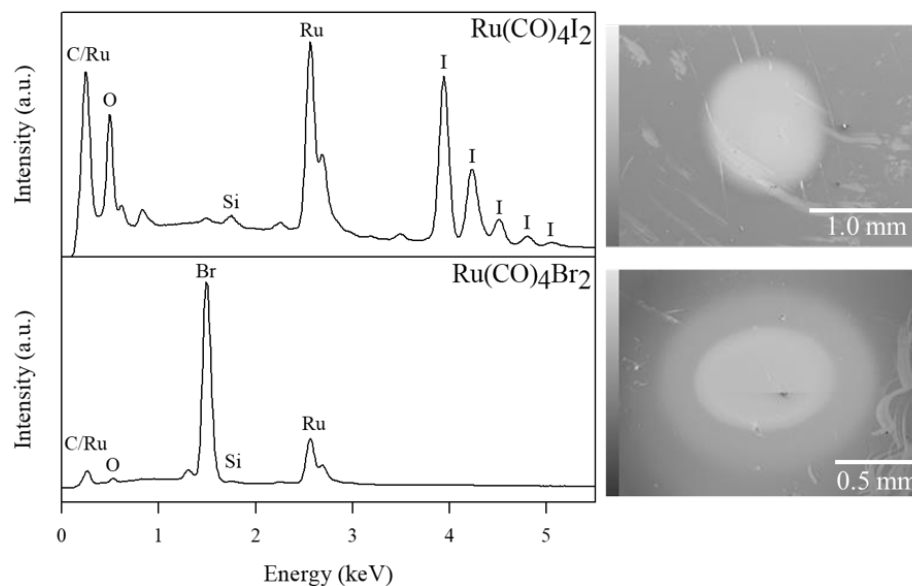
Figure 4.6: EDX spectra of a deposit made by EBID from (top) $Ru(CO)_4I_2$ and (bottom) $Ru(CO)_4Br_2$ under UHV conditions. To the right of each spectrum are SEM images of the respective deposits. Both the EDX spectra and the SEM images were taken using a primary electron beam energy of 10 kV.

of Ru (31 at. %), I (56 at. %), C (8 at. %), and O (5 at. %). Analysis of the EDX spectra from the Ru(CO)4Br2 deposit (bottom) shows a similar composition of 27 at. % Ru, 54 at. % Br, 15 at. % C, and 4 at. % O. In both deposits, Ru:X (x = Br, I) is close to the 1:2 ratio found in the precursor molecules. Due to overlap between the C EDX peak and some Ru EDX peaks, it is likely that the estimated at. % C is slightly high, and that the true carbon-to-oxygen ratio in the deposit is close to 1:1. The average CO:Ru ratio in the deposits is therefore approximately 1:6 – significantly lower than that found in the precursor (4:1). This indicates that the majority of CO ligands associated with the precursor molecule are not incorporated into the deposit. Elemental maps of the Ru L, I L, C K, O K, and Si K X-rays (shown in Supporting Information, Fig. 4.15)

show that all elements associated with the precursor molecule are localized within the deposit.

4.3.4 Argon ion irradiation of Ru(CO)$_4$I$_2$ thin films

Figure 4.7 depicts the XPS spectra for the C(1s), Ru(3d), O(1s) and I(3d$_{5/2}$) regions of the adsorbed Ru(CO)$_4$I$_2$ films in terms of increasing ion beam exposure time. The corresponding spectra belonging to the nanometer-thick Ru(CO)$_4$I$_2$ molecular film before ion beam exposure are depicted in each region (labeled "As-deposited" in Fig. 4.7). Before the ion beam exposure, there are four main peaks in C(1s)/Ru(3d) region. The two higher binding energy peaks at 289.2 and 294.4 eV (depicted in blue in Fig. 4.7) can be attributed to the C(1s) peak of the CO ligand and the π-π* transition (barely visible in Fig. 4.7) associated with metal carbonyls, respectively.[66, 69] The two lower binding energy peaks at 283.2 and 287.4 eV (depicted in red) are associated with the Ru(3d$_{5/2}$/3d$_{3/2}$) doublet and can also be described as the initial Ru species associated with molecular Ru(CO)$_4$I$_2$.[68, 70] The O(1s) region initially has two main peaks, a large one centered at 535.2 eV attributed to the CO ligand and a smaller one centered at 541.5 eV attributed to a π-π* shake up feature, which is observed in XPS due to the symmetric environment of the CO ligands.[67, 71] Prior to ion beam exposure, the I(3d$_{5/2}$) region consists of one peak, centered at 619.8 eV as shown in Fig. 4.7.[72, 73]

As a consequence of ion beam exposure, there is a significant decrease in the intensities of the initial Ru species (shown in red in Fig. 4.7) and the C(1s) peak associated with the CO ligand (blue in Fig. 4.7). There is
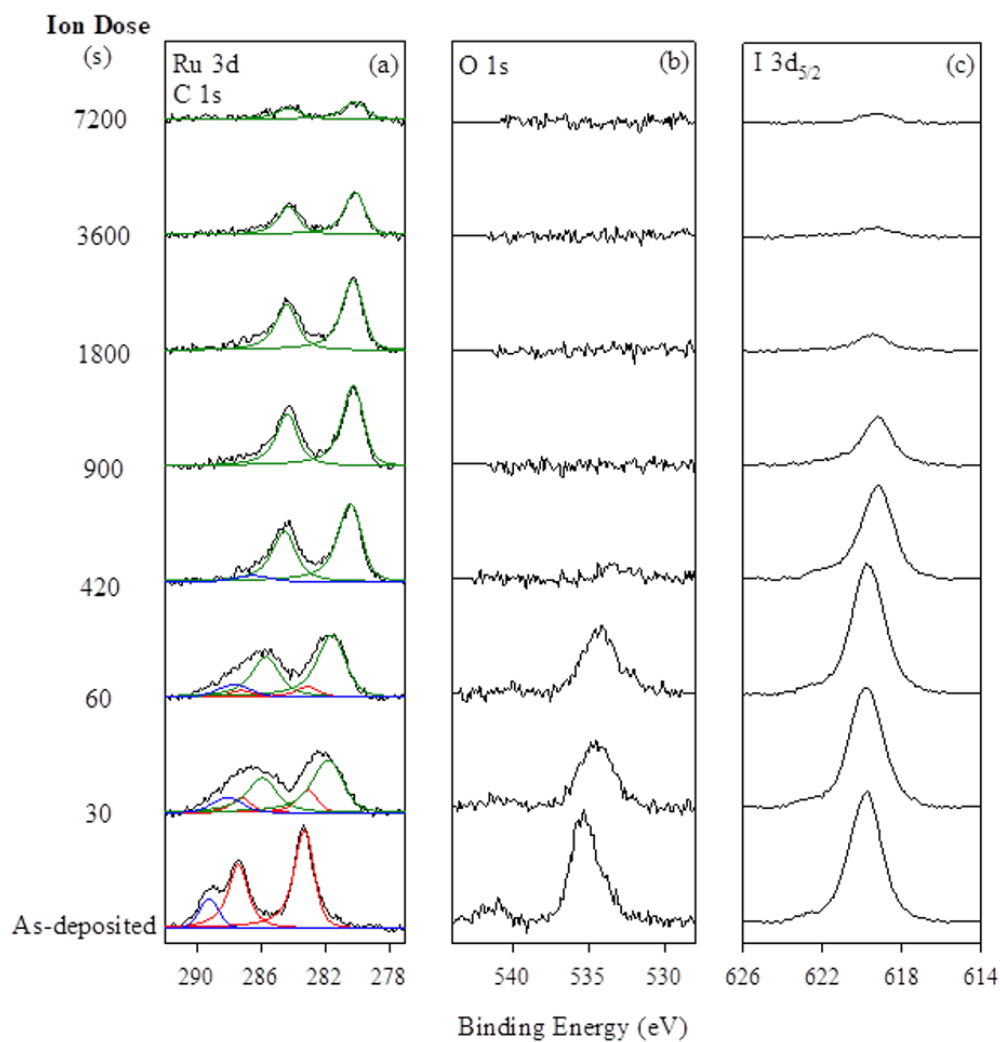
Figure 4.7: Evolution of the C(1s)/Ru(3d), O(1s), and I($3d_{5/2}$) XPS regions of ≈ 1.6 - 1.7 nm films of adsorbed Ru(CO)$_4$I$_2$ exposed to 860 eV Ar$^+$ ions. Speciation is shown in the C(1s)/Ru(3d) region, where the blue line represents C(1s), the red lines represent the Ru(3d) peaks associated with the Ru(CO)4I2 compound, and the green lines represent the Ru(3d) peaks associated with the species produced by Ar$^+$ irradiation.

a concurrent growth in two peaks centered at 281.7 and 285.9 eV, shown in green in Fig. 4.7, which are assigned as Ru($3d_{5/2}$) and Ru($3d_{3/2}$) peaks, respectively, and are associated with the Ru species of the ion-bombarded product. After 900 s of Ar$^+$ bombardment (0.036 mC/cm^2), the C(1s) peak is no longer visible. The intensities of the peaks associated with the product Ru species remains relatively constant up to 1800 s (0.072 mC/cm^2), after which the peak intensities decrease systematically. Previous XPS studies and theoretical studies of oxidized ruthenium under UHV conditions have reported a Ru(3d) region consisting of two components, labeled "screened" and "unscreened" peaks.[74, 75] The screened peaks are located about 2 eV higher in binding energy than the unscreened peaks and XPS studies of ruthenium oxides and metallic ruthenium found that the unscreened peaks increase in intensity as the system becomes more metallic, while the screened peaks concurrently decrease in intensity.[75–77] Thus, in the present study, the peaks associated with the initial and final Ru species may be also called "screened" and "unscreened" peaks, respectively.

In the O(1s) region, ion beam exposure produces a dramatic decrease in oxygen species. For exposure times higher than 900 s (0.036 mC/cm^2), there is no observable oxygen remaining on the surface. In the I($3d_{5/2}$) region, the first 60 s (0.0924 mC/cm^2) of Ar$^+$ exposure does not appear to have significant effect; however, after 420 s (0.017 mC/cm^2) of Ar$^+$ exposure, the intensity of the iodine peak decreases systematically. Minimal iodine is observed at Ar$^+$ exposure times above 1800 s (0.072 mC/cm^2).

Figure 4.8 presents the variation in the integrated spectral intensity within
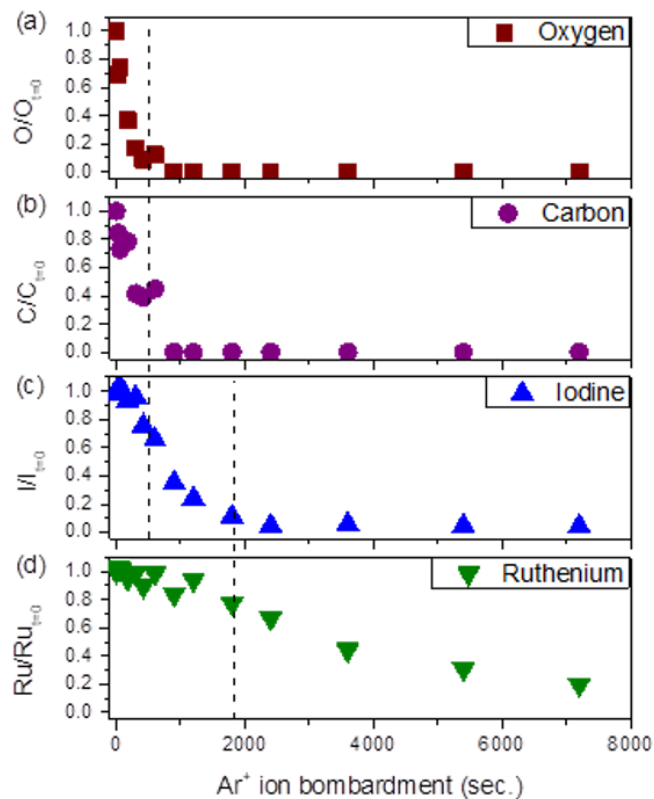
Figure 4.8: Change in fractional coverage of O, C, I and Ru atoms in $\approx$ 1.6 - 1.7 nm films of adsorbed $Ru(CO)_4I_2$ exposed to 860 eV Ar^+ ions.

the C(1s), Ru(3d), O(1s) and I($3d_{5/2}$) regions as a function of Ar^+ exposure time. Each data point represents the integrated XPS spectra for the respective element after a period of Ar^+ bombardment, normalized to the value measured for the unexposed $Ru(CO)_4I_2$ film. Fractional changes in $C/C_{t=0}$ and $O/O_{t=0}$ show a sharp exponential decrease until no C or O remains after an exposure time of 900 s (0.036 mC/cm^2). Hereafter, there is no traceable carbonyl ligand, consistent with carbonyl desorption. The $I/I_{t=0}$ fractional
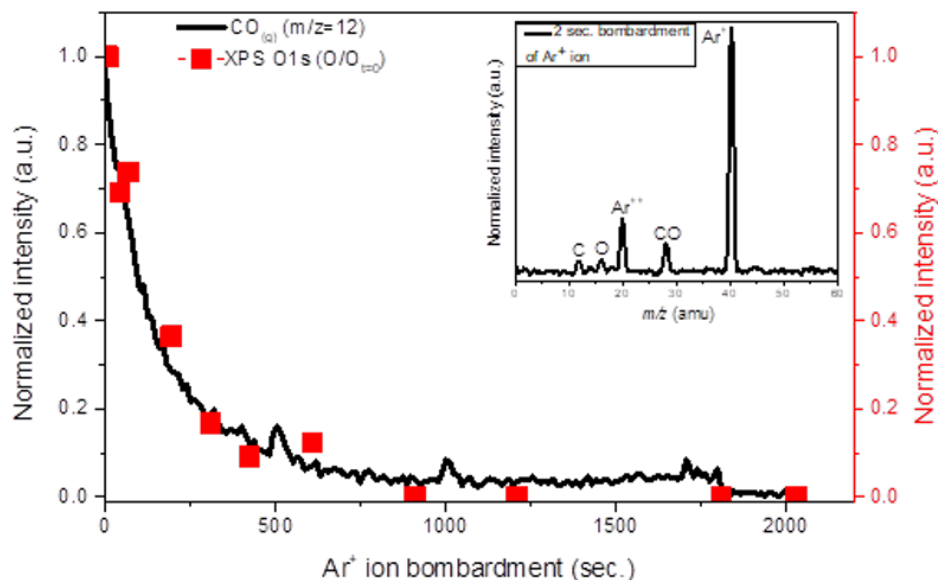
Figure 4.9: Kinetics of CO (m/z = 12 amu) desorption from an adsorbed $Ru(CO)_4I_2$ film exposed to 860 eV Ar^+ ions overlaid with the fractional coverage of O atoms as observed by XPS. The inset shows the mass spectrum of fragments desorbing from the $Ru(CO)_4I_2$ film after 2 s of ion beam bombardment.

value does not show a substantial change over the first 100 s (0.004 mC/cm^2) of Ar^+ bombardment, but then exhibits a similar exponential decrease to 5% of its initial value for ion beam exposure times ≤ 1800 s, remaining relatively constant thereafter. For low Ar^+ exposure times (< 900 s, 0.036 mC/cm^2), there is no concurrent change in the total intensity of ruthenium species ($Ru/Ru_{t=0}$), demonstrating there is no molecular desorption of $Ru(CO)_4I_2$. Once all of the carbonyl ligands have desorbed, as well as most of the iodine (≤ 1800 s, 0.072 mC/cm^2), continued ion beam exposure leads primarily to sputtering of the ruthenium species.

Figure 4.9 demonstrates the normalized kinetics of CO desorption from the surface characterized by the MS signal at 12 amu (C^+, black solid line) overlaid with the fractional coverage of carbonyl ligands in O(1s) XPS region (red boxes). Here, the atomic mass of carbon (m/z = 12) was used to follow the kinetics instead of CO (m/z = 28) in order to avoid contamination from nitrogen during the ion bombardment on the adsorbed thin $Ru(CO)_4I_2$ film. There is good agreement between the ion-stimulated desorption of CO and the fractional change in O(1s) coverage ($O/O_{t=0}$). The inset in Fig. 4.9 shows the mass spectrum of desorbing species during the ion beam bombardment. At an ion exposure time of 2 s (8 x 10^{-5} mC/cm^2), the only significant MS peaks detected are those associated with Ar^+ (m/z = 40), Ar^{2+} (m/z = 20) and CO (m/z = 28, 16, and 12, corresponding to CO, O, and C, respectively). Due to the considerable background pressure of argon, I^+ (m/z = 127) was not expected to be observed via MS during ion bombardment and consequently was not observed.

4.4 Discussion

4.4.1 Electron-induced reactions of $Ru(CO)_4I_2$

As can be seen in Figs. 4.1 and 4.2, DEA to gas phase $Ru(CO)_4I_2$ molecules overwhelmingly leads to the loss of two CO ligands. The loss of a single CO ligand is also observed, but with about 40 times less intensity. While significant loss of two CO units is a common observation in DEA to metal carbonyl compounds at low incident energy, it is uncommon for the loss of two CO ligands to be dominant over the loss of a single CO.[26, 40, 44, 78]

105

For this process to proceed at 0 eV incident energy, the electron affinity of the charge-retaining fragment (here, $[Ru(CO)_2I_2]^-$) must exceed the bond dissociation energy (BDE) needed to cleave the two Ru-CO bonds. We note that the extraction time from the ionization region of the instrument used for the DEA measurements is on the order of 10 μs, while the flight time through the QMS is about 50 μs. Therefore, if significant excess energy is retained by the fragment after the first CO loss, loss of a second CO ligand within 10 μs is more likely than the survival of this metastable anion over the approximately 50 μs flight through the QMS. Ru-I bond dissociation is also observed, producing I^-; this pathway is about 30 times less significant than the 2 CO loss pathway (Figs. 4.1 and 4.2), making it a comparably minor product. Finally, the loss of 3 CO units is observed through the high-energy side of the 0 eV resonance, but with relatively low intensity.

This is further rationalized by the well-known *trans* effect in inorganic chemistry. Assuming that the relative bond energies in the anion formed during DEA reflect the relative bond energies in the neutral precursor, the two carbonyl ligands *trans* to one another will be more weakly bound to the metal center than the two *trans* to the iodide ligands due to backbonding, which dominates metal-CO bond strengths. For the carbonyl ligands *trans* to iodide, the iodide lone pairs donate electron density into the metal d orbitals that participate in backbonding with the carbonyl π^* orbitals, strengthening the Ru-CO bonds through increased backbonding. Conversely, for the carbonyl ligands *trans* to each other, both carbonyl ligands are π-acids that compete for the same electron density in the same d orbitals, weakening both Ru-CO

bonds through the decrease in backbonding. Hence, the sum of the BDEs for the two Ru-CO bonds that are *trans* to one another are likeliest to be lower than the electron affinity of the corresponding fragment anion ([Ru(CO)$_2$I$_2$]$^-$), fueling the dominance of this pathway at 0 eV incident electron energy.

Conversely, DI of Ru(CO)$_4$I$_2$ produces much more extensive fragmentation, with appreciable intensities from the parent cation, fragments resulting from the loss of 1 - 4 CO ligands, and fragments associated with the loss of both CO and I. Based on the intensity averaged fragmentation pattern, an average of three CO ligands and 0.5 iodide ligands are lost per DI incident at 70 eV, as seen in Table 4.1. This can be compared to DEA, where the average CO loss per incident is close to two and the iodide loss is negligible.

Analysis of Figs. 4.3, 4.4, and 4.5 indicate that during the initial stage of electron-stimulated decomposition of adsorbed Ru(CO)$_4$I$_2$ molecules (electron doses < 1.6 mC/cm^2, 10.1 x 10^{15} e$^-$/cm^2), an average of about 2 CO ligands per parent molecule desorb from the substrate. The initial step in electron-induced deposition of Ru(CO)$_4$I$_2$ can thus be described as:

$$Ru(CO)_4I_{2(ads)} + e^- \rightarrow Ru(CO)_2I_{2(ads)} + 2CO_{(g)} \uparrow \qquad (4.5)$$
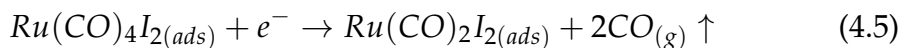
Here the adsorbed product (Ru(CO)$_2$I$_{2(ads)}$) is best viewed as a partially decarbonylated intermediate; the molecular formula is intended to be stoichiometric rather than to denote a specific bonding structure. This initial step is illustrated in Figure 4.10.

Since this initial step corresponds to the decomposition of the parent molecule, it can be compared to the gas phase electron-induced fragmentation
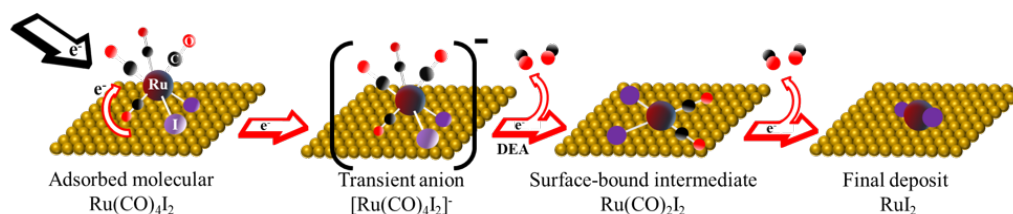
Figure 4.10: Schematic representation of the electron-induced surface reactions underlying electron beam induced deposition from $Ru(CO)_4I_2$. In the first step, electron attachment to $Ru(CO)_4I_2$ produces a transient negative ion that decomposes through the loss of two carbonyl ligands, labeled "DEA". In the second slower step, the residual two carbonyl ligands desorb from the surface under extended electron irradiation.

of $Ru(CO)_4I_2$ via DEA (Figs. 4.1 and 4.2) and DI (Fig. 4.1). Similarly to DEA-induced decomposition of $Ru(CO)_4I_2$, the initial electron-induced ligand loss step in electron-induced deposition of $Ru(CO)_4I_2$ proceeds via loss of two CO ligands and no iodide loss from the surface is observed. This is in marked contrast with DI-induced fragmentation, which is a statistical process that leads to an average loss of 3 CO ligands and 0.5 iodide ligands per DI-initiated event. This comparison shows that the extent of the initial fragmentation in the surface experiments is much closer to what is observed in the gas phase for DEA, rather than via DI.

The initial electron-induced decomposition step is determined by the energy distribution of secondary electrons and the cross sections for the various possible electron-induced decomposition processes (i.e., DEA, DI, ND, and DD) as a function of the electron energy, i.e., the effective damage yield.[19, 26, 48] The observation that the extent of the electron-induced decomposition of adsorbed $Ru(CO)_4I_2$ matches that which is observed for DEA in the gas

phase and is much less extensive than what is observed for DI suggests three possibilities: (i) the secondary electron energy distribution is not significant above the ionization energy (IE) of $Ru(CO)_4I_2$, (ii) DI of $Ru(CO)_4I_2$ is more efficiently quenched on the surface, or (iii) the absolute cross sections for DI of $Ru(CO)_4I_2$ are lower than those for DEA. Regarding (i), the secondary electron energy distribution from Au surfaces exposed to 300 eV has indeed been shown to be narrow, with the majority of secondary electrons having energies below 10 eV.[79] However, this energy distribution is sensitive to surface contamination and topography.[79] In this regard, previous studies have shown no significant difference in the products formed when organometallic precursors adsorbed on different surfaces likely to have different secondary electron distributions (principally Au and HOPG) have undergone electron-stimulated reactions/decomposition.[34, 41, 45, 80] The second possibility (ii) has been recently discussed in the context of $Pt(CO)_2Cl_2$,[48] wherein the metastable nature of DI may cause it to be effectively quenched at surfaces after the initial loss of the most loosely bound ligands.[47] This may also be the case for $Ru(CO)_4I_2$, where the two CO ligands trans to the iodide ligands may be more strongly bound than the other CO ligands. However, the gas phase DI spectrum of $Ru(CO)_4I_2$ shows no suggestion of any particular stability associated with $[Ru(CO)_2I_2]^+$, making this explanation unlikely. With regard to (iii), we find the sum of the count rates for all DEA fragments and all DI fragments to be similar when the DEA count rates are normalized with respect to SF_6^- from SF_6 at 0 eV and the DI count rates with respect to Ar^+ from Ar at 70 eV. However, DEA is a resonant process and proceeds within a narrow energy range, while DI is non-resonant and thus is efficient over a

109

very broad energy range above its threshold. The secondary electron energy distribution (i) will therefore also have a determinative effect on the integral damage yield.[19, 26, 48] Finally, we note that ND was not studied here, and recent studies have suggested that it may play an important role in FEBID.[78, 81, 82]

Nonetheless, our experimental evidence shows a clear correlation between the predictions from gas phase DEA and the initial electron-induced decomposition of adsorbed $Ru(CO)_4I_2$, consistent with DEA, rather than DI, as the primary route for the initial electron-induced decomposition step of this molecule. Further, independent of the potential contribution from ND, it is clear from the current data that DI is significantly less efficient for electron-induced decomposition of $Ru(CO)_4I_2$ on the surface than in the gas phase, while this is not evident for DEA.

The second electron-induced reaction stage of adsorbed $Ru(CO)_4I_2$ proceeds at higher electron doses (> 1.6 mC/cm^2, 10.1 x 10^{15} e$^-$/cm^2). In this regime, the remaining carbon and oxygen are removed from the surface, seen most clearly by the absence of any oxygen after an electron dose of 163 mC/cm^2 (1015 x 10^{15} e$^-$/cm^2, Figs. 4.3 and 4.4). This second step can therefore be described as:

$$Ru(CO)_2I_{2(ads)} + e^- \rightarrow RuI_{2(ads)} + 2CO_{(g)} \uparrow \qquad (4.6)$$
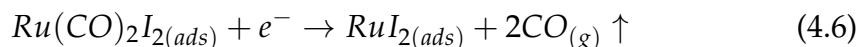
This second step shown schematically in Fig. 4.10 differs from several previous studies of electron-induced deposition of adsorbed carbonyl-containing organometallic precursor molecules, which include $Co(CO)_3NO$, $W(CO)_6$,

CpFe(CO)$_2$Mn(CO)$_5$, and CpFe(CO)$_2$Re(CO)$_5$.[34, 41, 43, 56] For these com-
pounds, the initial electron-initiated precursor decomposition step leads to
multiple CO ligand loss, analogous to Ru(CO)$_4$I$_2$ (Eq. 4.5, Fig. 4.10), but contin-
ued electron irradiation decomposed the remaining CO ligands into graphitic
carbon and reactive oxygen species, which then oxidized the metal atoms. Con-
versely, in electron-induced deposition studies of adsorbed H$_2$FeRu$_3$(CO)$_{12}$,
(η^3-C$_3$H$_5$)Ru(CO)$_3$Br, and Pt(CO)$_2$Cl$_2$, no CO decomposition is observed.[45,
47, 50] Since the fate of the CO ligands (i.e. desorption or decomposition)
plays an important role in determining the ultimate metal content of FEBID
nanostructures, it is useful to consider the potential underlying causes of
electron-induced CO decomposition (CO$_{(ads)}$ + e$^-$ $\rightarrow$ C$_{(ads)}$ + ROS) vs. des-
orption (CO$_{(ads)}$ + e$^-$ $\rightarrow$ CO$_{(g)}$) in the partially decarbonylated intermediates,
which are common intermediates in FEBID of metal carbonyls.

Several factors may influence electron-induced CO decomposition vs. des-
orption in these partially decarbonylated organometallic intermediates, in-
cluding the oxophilicities of the various metal centers (Co, W, Fe, Mn, Re,
Ru, and Pt) and the nature of the ancillary ligands ((η^3-C$_3$H$_5$), NO, Cl, Br,
I). Analysis of the oxophilicities of the oxidized metal centers in the com-
pounds that undergo electron-induced CO decomposition (Co, W, Mn, Fe,
and Re) vs. desorption (Fe, Ru, and Pt) does not show a strong connection
between oxophilicity and decomposition vs. desorption (the aforementioned
metals have oxophilicities of 0.4, 0.8, 0.4, 0.4, and 0.5, respectively, vs. 0.4,
0.4, and 0.1, respectively).[83] However, it is evident that metal-halide bonds

are present in most of the precursors that undergo electron-induced CO desorption rather than decomposition, and none of the precursors that undergo electron-induced CO decomposition contain halide ligands. This suggests that the presence of halides promotes electron-induced CO desorption from partially decarbonylated intermediates.

Electron beam-induced deposits created from $Ru(CO)_4I_2$ under a constant partial pressure of precursor molecules and a constant electron emission current (Fig. 4.6) are composed primarily of ruthenium and iodine, with a $\approx$ 2:1 iodine-to-ruthenium ratio and minimal (< 10 at. %) carbon and oxygen contamination. In related studies we have shown that the CO ligands in the partially decarbonylated $Ru(CO)_2I_2$ intermediate are stable at room temperature (see Figure 4.16). As a result, all of the elementary reaction steps responsible for the formation of the deposit in FEBID should be electron-induced rather than thermal processes. Under these conditions, the observation that the composition of the EBID structures in Fig. 4.6 coincides with the prediction of the low temperature UHV electron irradiation studies in the limit of larger electron doses supports the relevance of the two deposition steps identified by gas phase and surface studies (Eq. 4.5 and 4.6) to FEBID. Deposits formed from $Ru(CO)_4Br_2$ show similar results, suggesting that these electron-induced processes are independent of the nature of the halogen, as was previously found for $Pt(CO)_2X_2$ and $(\eta^3\text{-}C_3H_5)Ru(CO)_3X$ (X = Br, Cl).[45, 47] Although the persistence of the iodide ligand in the deposit presents a limitation to the metal purity of deposits made from this precursor, previous studies have shown that residual halide ligands may be removable by exposure to atomic hydrogen

(e.g. $Pt(NH_3)_2Cl_2$, $Pt(CO)_2Cl_2$)[59, 84] while residual carbon contamination is much harder to remove.

The presence of small quantities of carbon and oxygen in these deposits in roughly equal concentrations may be due to the relatively slow rate of the second deposition step (Eq. 6), causing some residual CO ligands to be trapped in the growing deposit. A comparison of the relative rates of the two electron-induced ligand dissociation steps shows that the first step (Eq. 4.5) requires an electron dose of approximately 1.6 mC/cm^2 (10.1 x 10^{15} e$^-$/cm^2), while the second step (Eq. 4.6) is a slower process requiring an electron dose of about 163 mC/cm^2 (1015 x 10^{15} e$^-$/cm^2). Electron-induced M-CO bond dissociation of the partially decarbonylated intermediate ($Ru(CO)_2I_2$, Eq. 4.6) is therefore about two orders of magnitude slower than the initial electron-induced carbonyl loss step (Eq. 4.5). Under these circumstances, some residual CO ligands in the partially decarbonylated intermediate may be unable to desorb (Eq. 4.6) before the steady state film growth causes the electron intensity experienced by the partially decarbonylated intermediates to fall to zero, thus preventing further CO desorption and producing this contamination. Another potential source of carbon and oxygen contamination may be the trapping of desorbing CO within the growing deposit lattice such that it recombines before escaping.

4.4.2   Ion-induced reactions of $Ru(CO)_4I_2$

In order to understand the ion-induced fragmentation mechanism of the adsorbed precursor molecule, it is crucial to thoroughly examine the desorption

of the ligands during ion beam exposure. To this end, Fig. 4.9 shows MS data taken during ion beam exposure compared with the fractional coverage of oxygen remaining on the surface as observed by XPS. The strongest evidence of intact CO desorption is contributed by mass spectrometry (Fig. 4.9 inset, Figure 4.18), allowing the use of the C signal ($m/z = 12$ amu) to observe the kinetics of CO desorption, as depicted in Fig. 4.9. Fractional coverage of oxygen was used instead of fractional coverage of carbon due to the overlap of the Ru(3d) and C(1s) XPS regions, potentially increasing the chance for error in the analysis of carbon signal, as well as the higher relative sensitivity of the O(1s) signal as compared to the C(1s) signal. This causes the results from the O(1s) region to be more reliable than those from the C(1s) region. It is evident from examining Fig. 4.9 that the decay rates of the carbon signal from MS and the fractional oxygen coverage from XPS have good agreement, indicating that the carbonyl ligands desorb intact from the surface without decomposing. The reaction step for the initial faster reaction under low ion exposure time (< 900 s, 0.036 mC/cm^2) can therefore be shown as:

$$Ru(CO)_4I_{2(ads)} + 860eV\ Ar^+_{(g)} \xrightarrow{k_1} RuI_{2(ads)} + 4(CO)_{(g)} \uparrow \qquad (4.7)$$
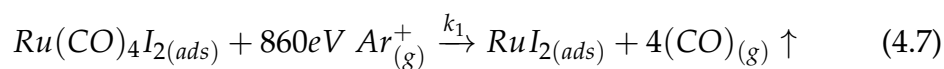
Here, k_1 is the rate constant of this reaction (4.7). Interestingly, the complete desorption of all CO ligands was observed under very low ion beam exposure times in the absence of any molecular sputtering.

This is a substantially different initial step than is observed for the electron-induced decomposition of adsorbed thin films of Ru(CO)$_4$I$_2$, where only two CO ligands are lost in the initial step (Eq. 4.5) and the remaining two CO

114

ligands are lost in a slower second step (Eq. 4.6). Additionally, this reaction proceeds much faster than the initial electron-induced CO loss step (Eq. 4.5), which is complete after an electron dose of 1.6 mC/cm^2, while the initial ion-induced CO loss step (Eq. 4.7) is complete after an ion dose of 0.036 mC/cm^2. Thus, it is likely that the secondary electrons do not play a strong role in the Ar$^+$-induced decomposition of adsorbed Ru(CO)$_4$I$_2$; instead, these reactions are governed by collision-induced energy transfer, as was found previously for CpFe(CO)$_2$Re(CO)$_5$.[56]

To study the kinetics of ion-induced decomposition of adsorbed Ru(CO)$_4$I$_2$, a step by step analysis of the sequence of chemical reactions forming the general reaction mechanism is required. The rate constants of each of these chemical reactions can be determined by thorough examination of the fractional loss of each element associated with the precursor molecule. As all carbonyl ligands are lost through the reaction described by Eq. 4.7, the associated rate constant (k$_1$) can thus be determined by fitting the fractional loss of either carbon or oxygen to a first order decay profile. The fractional coverage of oxygen was thus plotted as a function of time and fit using the differential first order rate equation (Eq. 4.8), as shown in Figure 4.11:

$$\frac{O_t}{O_0} = e^{-k_1 t} \tag{4.8}$$

Here, k$_1$ is the rate constant for Eq. 4.8, t is the Ar$^+$ exposure time, O$_t$ is the oxygen coverage at time t, and O$_0$ is the oxygen coverage at t=0. The rate constant (k$_1$) was found to be 0.006 s^{-1} (using the primary ion current density of $\approx$ 40 nA/cm^2, k$_1$ = 150 cm^2/mC), with a correlation (R^2) between the data
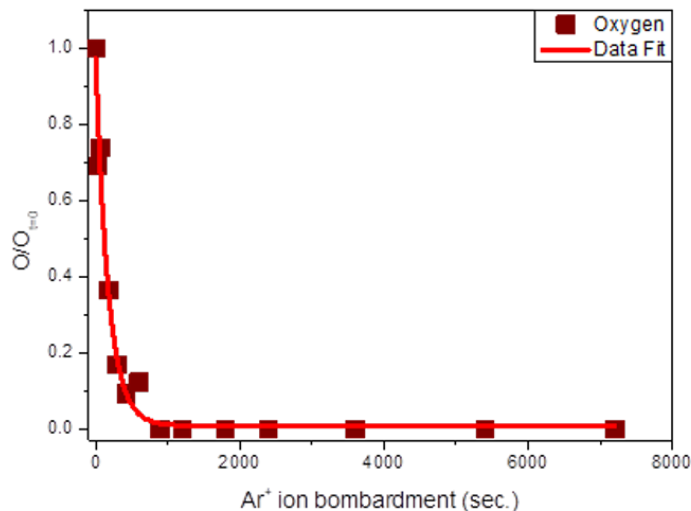
Figure 4.11: Change in fractional coverage of adsorbed O atoms in a Ru(CO)$_4$I$_2$ film exposed to 860 eV Ar$^+$ ions. The graph has been fit by a first order exponential decay function (Eq. 4.8, depicted in text).

and fit of 0.99.

For Ar$^+$ ion exposures from $\approx$ 900 to 1800 s (0.036 - 0.072 mC/cm^2), the most significant changes are observed in the I(3d$_{5/2}$) region (Figs. 7c and 8c). Under low Ar$^+$ exposure times (< 420 s, 0.017 mC/cm^2), the fractional coverage of iodine remains largely unchanged; however, once the carbonyl ligands desorb from the surface (Eq. 4.7), the iodine sputtering is the dominant reaction that can be observed. Although iodine could not be detected using MS due to the background intensity of argon during ion bombardment, the reaction path can be estimated from the XPS data as:

$$RuI_{2(ads)} + 860eV \; Ar^+_{(g)} \xrightarrow{k_2} Ru_{(ads)} + 2I_{(g)} \uparrow \qquad (4.9)$$
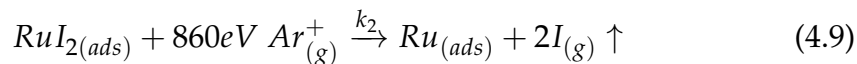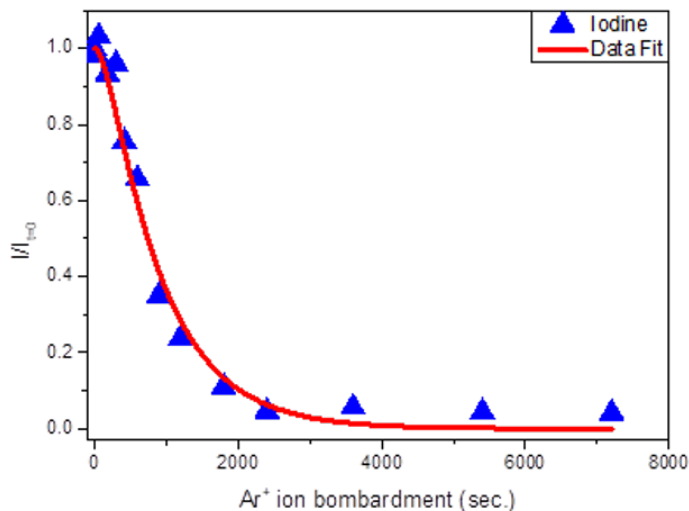
Figure 4.12: Change in fractional coverage of adsorbed I atoms in a $Ru(CO)_4I_2$ film exposed to 860 eV Ar^+ ions. The graph has been fit by the sum of two first order decay functions, as shown in Eq. 4.10.

Here, k_2 is the rate constant for this reaction. This reaction is not intended to imply chemical bonding or lack thereof in either the adsorbed RuI_2 or the sputtered iodine species, but is rather intended to be stoichiometric.

The decrease in the fractional coverage of iodine seems to be triggered by CO ligand loss from the surface, as evidenced by its initial delay. Therefore, one might deduce a consecutive reaction for the desorption mechanism of the ligands wherein the product of CO ligand desorption (RuI_2) further decays under continued ion bombardment, producing the iodine desorption (Eq. 4.9). In such a reaction scheme, the total decay rate of iodine (I_t/I_0) would be able to be fit to the sum of the differential rate equations of the two reactions that, in sum, produce the iodine loss, which are given in Equations 4.7 and 4.9.

117

Thus, the fractional loss of iodine must be fit to a function that is the sum of the two first order decay equations:

$$\frac{I_t}{I_0} = \frac{k_2 e^{-k_1 t} - k_1 e^{-k_2 t}}{k_2 - k_1} \tag{4.10}$$

Here, I_t is the iodine coverage at time t, I_0 is the iodine coverage at t=0, k_1 is the rate constant for Eq. 4.7 (0.006 s^{-1}), k_2 is the rate constant for Eq. 4.9, and t is the Ar^+ bombardment time. From the fit shown in Figure 4.12, the rate constant for Eq. 4.9 was found to be 0.001 s^{-1} (25 cm^2/mC) with an R^2 value of 0.99.

For higher ion exposure times ($\geq$ 1800 s, 0.072 mC/cm^2), significant ruthenium sputtering is observed (Figs. 4.7a and 4.8d), occurring at an increased rate after the CO ligands are fully desorbed and iodine has been largely sputtered. One potential explanation is the CO and I ligands form a protective matrix around the Ru atoms, preventing them from being sputtered. Hence, the sputtering of Ru can be considered the third ion-induced reaction that occurs on the surface:

$$Ru_{(ads)} + 860eV \ Ar^+_{(g)} \xrightarrow{k_3} Ru_{(g)} \uparrow \tag{4.11}$$
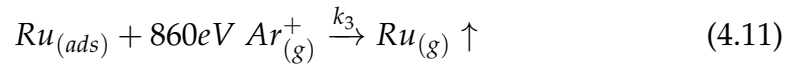
Here, k_3 is the rate constant associated with Eq. 4.11. The integrated rate function for this reaction can thus be written as:
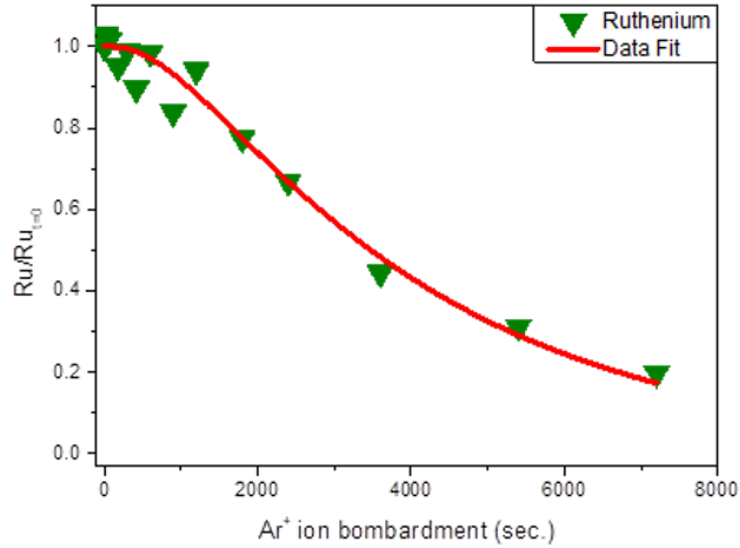
Figure 4.13: Change in fractional coverage of adsorbed Ru atoms. The graph has been fit by the integrated rate function shown in Eq. 4.12.

$$\frac{Ru_t}{Ru_0} = \left(\frac{k_1 k_2}{(k_2 - k_1)(k_3 - k_1)}\right) e^{-k_1 t} + \left(\frac{k_1 k_2}{(k_1 - k_2)(k_3 - k_2)}\right) e^{-k_2 t} \quad (4.12)$$

$$+ \left(\frac{k_1 k_2}{(k_1 - k_3)(k_2 - k_3)}\right) e^{-k_3 t} + \left(\frac{k_2 e^{-k_1 t} - k_1 e^{-k_2 t}}{k_2 - k_1}\right)$$

Here, Ru_t is the ruthenium coverage at time t, Ru_0 is the ruthenium coverage at t=0, k_1 is the rate constant for Eq. 4.7 (0.006), k_2 is the rate constant for Eq. 4.9 (0.001), k_3 is the rate constant for Eq. 4.11 and t is the Ar^+ bombardment time. This function was fit to the data, as can be seen in Figure 4.13, and the value for the rate constant (k_3) was found to be 0.0003 s^{-1} (7.5 cm^2/mC) with an R^2 value of 0.98.

119

As can be seen in the above kinetic study, the rate of CO loss (Eq. 4.7, k_1 = 0.006 s^{-1}) and I loss (Eq. 4.9, k_2 = 0.001 s^{-1}) are both an order of magnitude faster than the rate of Ru sputtering (Eq. 4.11, k_3 = 0.0003 s^{-1}). The loss in intensity of CO and I is also concurrent with the loss of the initial Ru species (screened) and the increase in intensity of the final Ru species (unscreened) for the comparatively small ion beam exposure times ($\leq$ 180 s, 0.072 mC/cm^2). In Figure 4.19, it is explicitly shown that the concurrent increase in final ruthenium species strongly suggests that the ruthenium is metallic.[85] Under appropriate ion beam-induced deposition conditions with precise parameters, $Ru(CO)_4I_2$ compound could thus likely produce pure, metallic Ru deposits.

4.5 Conclusions

A comprehensive study has been performed on the electron-induced reactions of $Ru(CO)_4I_2$ in the gas phase, adsorbed on surfaces, and in EBID. In the gas phase, DEA to $Ru(CO)_4I_2$ was found to overwhelmingly lead to loss of two carbonyl ligands via a resonance centered close to 0 eV, while DI of $Ru(CO)_4I_2$ was found to produce much more extensive fragmentation. Surface science studies of thin films of $Ru(CO)_4I_2$ under UHV conditions found that 500 eV electron irradiation caused an initial deposition step characterized by loss of two carbonyl ligands, forming a partially decarbonylated intermediate, followed by a two orders of magnitude slower second step characterized by the loss of the remaining two carbonyl ligands. A comparison of the gas phase and surface science data shows that the extent of the initial electron-induced reaction of adsorbed $Ru(CO)_4I_2$ matches the ligand loss observed for DEA

in the gas phase, while it is much less extensive than is the fragmentation observed for DI in the gas phase. This may be due to the overlap of the secondary electron energy distribution with the energy dependence of the DEA and DI cross sections or due to more effective quenching of DI as compared to DEA on the surface. Interestingly, the residual carbonyl ligands in the partially decarbonylated intermediate desorb from the surface under sustained electron irradiation, rather than decomposing and being incorporated into the deposit as has been observed for other metal carbonyls. Consistent with the predictions of the surface science studies, deposition of $Ru(CO)_4I_2$ and its bromide derivative $Ru(CO)_4Br_2$ with a 3 kV focused electron beam produced deposits with a $\approx$ 1:2 ruthenium-to-halide ratio and minimal carbon and oxygen contamination. Coupled with previous studies of similar halogenated metal carbonyl precursors (i.e. $Pt(CO)_2Cl_2$ and $Pt(CO)_2Br_2$), these results support the idea that organometallic precursors with carbonyl and halide ligands can produce nanostructures using FEBID free of carbon or oxygen contamination.

Additionally, low energy (860 eV) electron- and Ar^+-induced reactions of adsorbed $Ru(CO)_4I_2$ were compared and found to proceed via markedly different reactions. Ion exposure caused an initial deposition step characterized by the loss of all four carbonyl ligands, followed by a somewhat slower second step characterized by the removal of the iodide ligands and a much slower third step characterized by sputtering of the remaining ruthenium. Additionally, all ion-induced reactions were found to proceed much more rapidly than the electron-induced reactions. Ion-induced deposition of adsorbed $Ru(CO)_4I_2$

is thus hypothesized to proceed via collision-induced energy transfer between the incident Ar^+ and physisorbed $Ru(CO)_4I_2$. These findings suggest that ion-induced deposition under appropriate conditions using $Ru(CO)_4I_2$ could produce high purity metallic ruthenium nanostructures.

4.6   Supporting Information
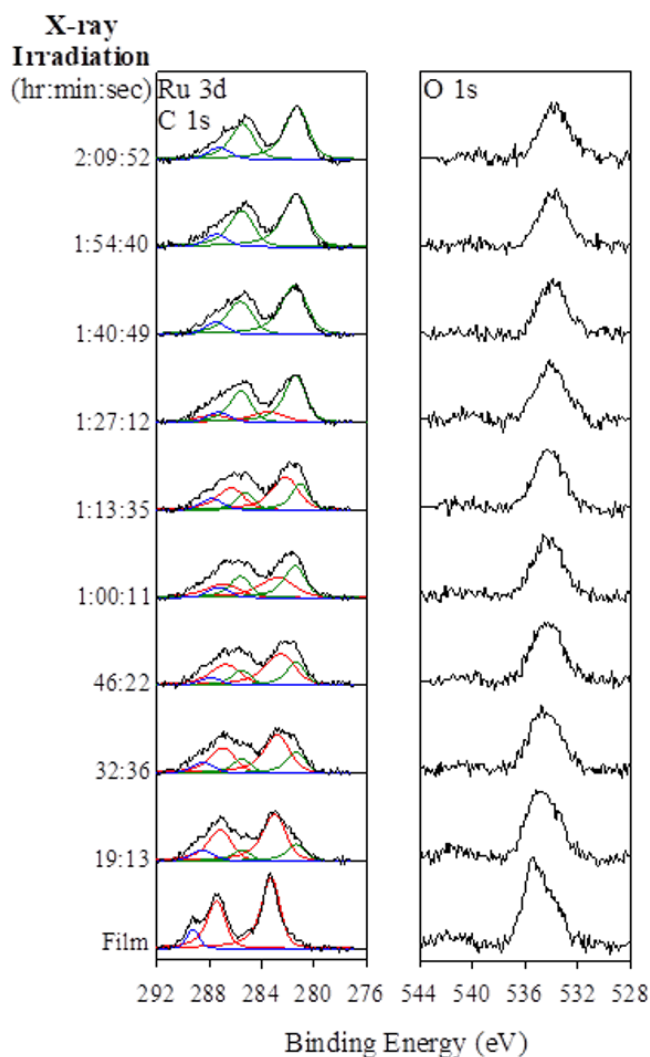
Figure 4.14: Evolution of the C(1s)/Ru(3d) and O(1s) XPS regions of a 1.3 nm Ru(CO)$_4$I$_2$ film upon irradiation with Mg Kα X-rays. The bottom spectrum represents the as-deposited film. The average time to take each full set of spectra (C(1s),/Ru(3d), O(1s), and I(3d$_{5/2}$) XPS regions) was 19 minutes and 13 seconds. Speciation is shown in the C(1s)/Ru(3d) region as in Figs. 4.3 and 4.7: C(1s) is represented in blue, the Ru(3d) peaks associated with the compound are represented in red, and the Ru(3d) peaks associated with the species produced by electron irradiation and X-ray irradiation are represented in green. X-ray irradiation dose is shown on the left-hand side in units of hours, minutes, and seconds.
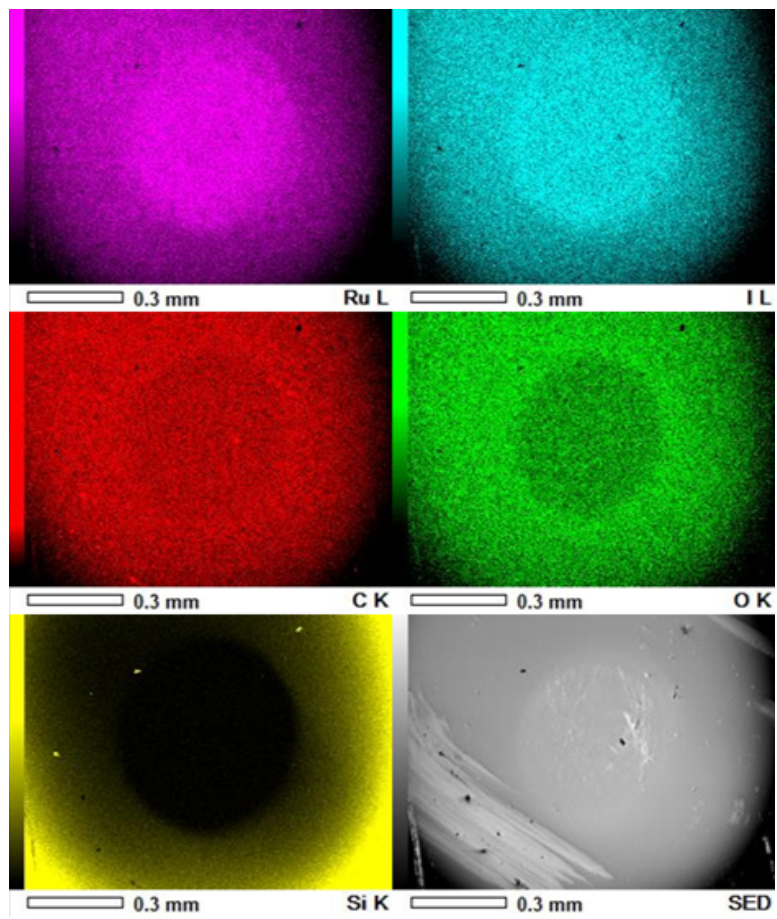
Figure 4.15: Elemental maps of the Ru L, I L, C K, O K, and Si K X-rays taken with SEM/EDX.
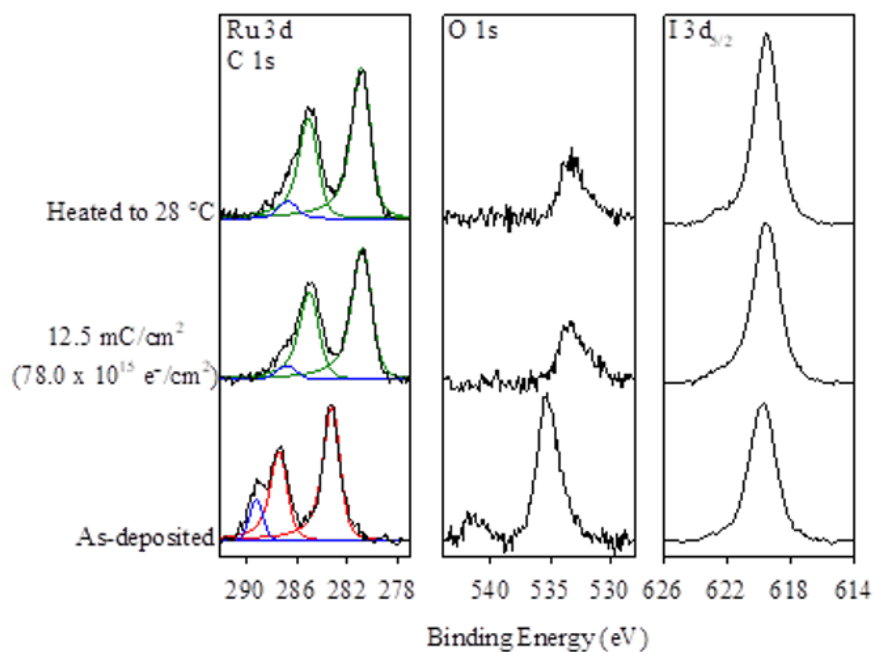
Figure 4.16: Evolution of the C(1s),/Ru(3d), O(1s), and I($3d_{5/2}$) XPS regions of a 1.8 nm Ru(CO)$_4$I$_2$ film upon irradiation with 500 eV electrons at an electron dose of 12.5 mC/cm^2 (78.0 x 10^{15} e$^-$/cm^2) and subsequent heating to room temperature (28 °C). The bottom spectrum represents the as-deposited, un-irradiated film. Speciation is shown in the C(1s)/Ru(3d) region as in Figs. 4.3 and 4.7, where C(1s) is shown in blue, the Ru(3d) peaks associated with the compound are shown in red, and the the Ru(3d) peaks associated with the species produced by electron irradiation are shown in green.
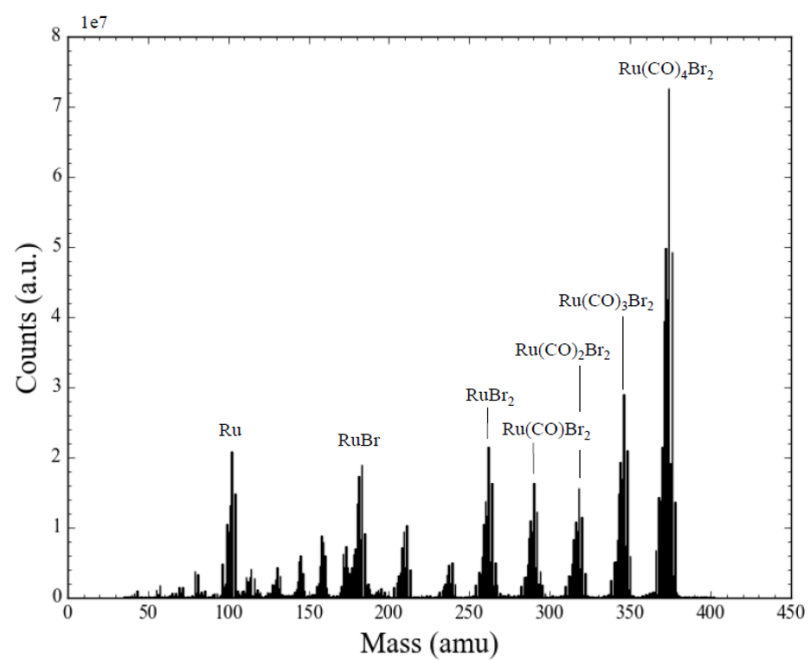
Figure 4.17: Mass spectrum of $Ru(CO)_4Br_2$ formed at 70 eV incident electron energy due to DI.
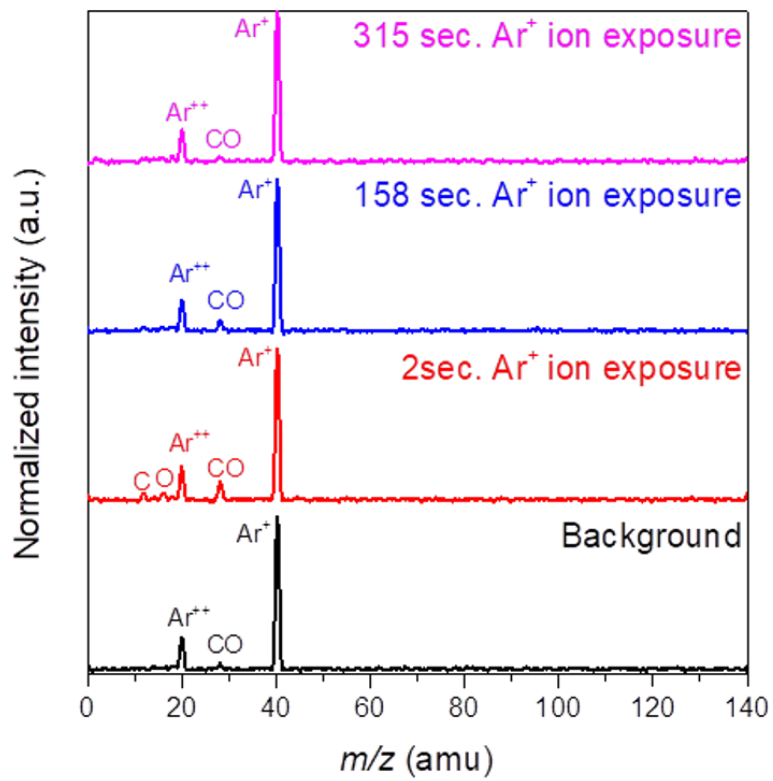
Figure 4.18: Mass spectra showing the carbonyl (CO) desorption during Ar^+ ion bombardment under different exposure times.
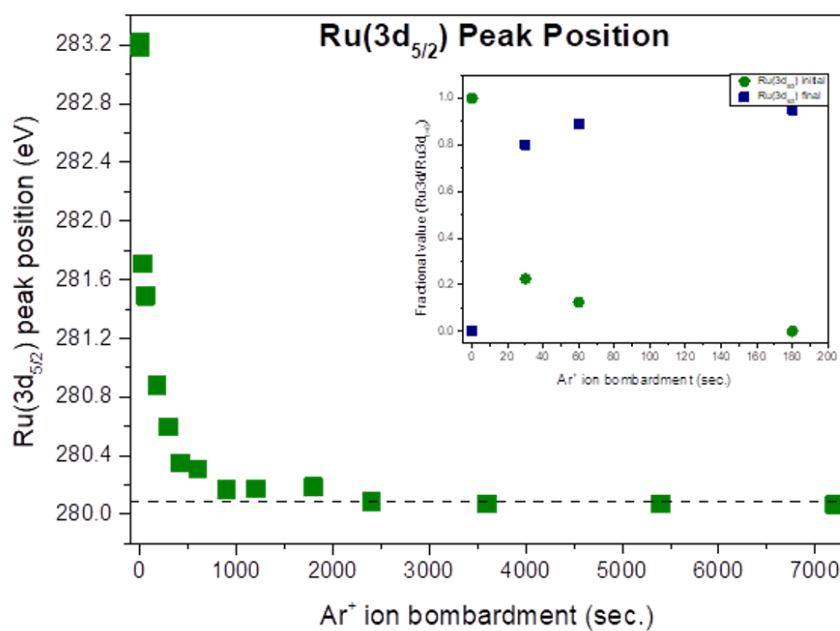
Figure 4.19: Change in binding energy of the Ru(3d5/2) peak (initial data point from molecular Ru, others from the deposit Ru state) during Ar^+ ion bombardment. Inset: comparison of the fractional coverage of molecular Ru(3d$_{5/2}$) and deposit Ru(3d5/2) peaks as a function of ion bombardment time.

References

[1] S. Chattopadhyay, L.-C. Chen, K.-H. Chen, *Critical Reviews in Solid State and Materials Sciences* **2006**, *31*, 15–53.

[2] I. Utke, P. Hoffmann, J. Melngailis, *Journal of Vacuum Science & Technology B: Microelectronics and Nanometer Structures* **2008**, *26*, 1197.

[3] W. F. van Dorp, C. W. Hagen, *Journal of Applied Physics* **2008**, *104*, 081301.

[4] M. Huth, F. Porrati, C. Schwalb, M. Winhold, R. Sachser, M. Dukic, J. Adams, G. Fantner, *Beilstein Journal of Nanotechnology* **2012**, *3*, 597–619.

[5] W. F. van Dorp, B. van Someren, C. W. Hagen, P. Kruit, P. A. Crozier, *Nano Letters* **2005**, *5*, 1303–1307.

[6] H. C. George, T. A. Orlova, A. O. Orlov, G. L. Snider, *Journal of Vacuum Science & Technology B Nanotechnology and Microelectronics: Materials Processing Measurement and Phenomena* **2011**, *29*, 06FB01.

[7] J. Pablo-Navarro, D. Sanz-Hernández, C. Magén, A. Fernández-Pacheco, J. M. de Teresa, *Journal of Physics D: Applied Physics* **2017**, *50*, 18LT01.

[8] L. Keller, M. K. I. Al Mamoori, J. Pieper, C. Gspan, I. Stockem, C. Schröder, S. Barth, R. Winkler, H. Plank, M. Pohlit, J. Müller, M. Huth, *Scientific Reports* **2018**, *8*, 6160.

[9] R. Winkler, F.-P. Schmidt, U. Haselmann, J. D. Fowlkes, B. B. Lewis, G. Kothleitner, P. D. Rack, H. Plank, *ACS Applied Materials & Interfaces* **2017**, *9*, 8233–8240.

[10] K. Höflich, R. B. Yang, A. Berger, G. Leuchs, S. Christiansen, *Advanced Materials* **2011**, *23*, 2657–2661.

[11] S. Sengupta, C. Li, C. Baumier, A. Kasumov, S. Guéron, H. Bouchiat, F. Fortuna, *Applied Physics Letters* **2015**, *106*, 042601.

[12] R. Córdoba, A. Ibarra, D. Mailly, J. M. De Teresa, *Nano Letters* **2018**, *18*, 1379–1386.

[13] M. Gabureac, L. Bernau, I. Utke, G. Boero, *Nanotechnology* **2010**, *21*, 115503.

[14] G. Arnold, R. Winkler, M. Stermitz, A. Orthacker, J. Noh, J. D. Fowlkes, G. Kothleitner, M. Huth, P. D. Rack, H. Plank, *Advanced Functional Materials* **2018**, *28*, 1707387.

[15] C. H. Schwalb, C. Grimm, M. Baranowski, R. Sachser, F. Porrati, H. Reith, P. Das, J. Müller, F. Völklein, A. Kaya, M. Huth, *Sensors* **2010**, *10*, 9847–9856.

[16] I. Utke, P. Hoffmann, R. Berger, L. Scandella, *Applied Physics Letters* **2002**, *80*, 4792–4794.

[17] K. Edinger, H. Becht, R. Becker, V. Bert, V. A. Boegli, M. Budach, S. Göhde, J. Guyot, T. Hofmann, O. Hoinkis, A. Kaya, H. W. Koops, P. Spies, B. Weyrauch, J. Bihr in 23rd Annual BACUS Symposium on Photomask Technology, *Vol. 5256*, (Eds.: K. R. Kimmel, W. Staud), International Society for Optics and Photonics, **2003**, p. 1222.

[18] T. Bret, T. Hofmann, K. Edinger, *Applied Physics A* **2014**, *117*, 1607–1614.

[19] R. M. Thorman, R. K. T. P., D. H. Fairbrother, O. Ingólfsson, *Beilstein Journal of Nanotechnology* **2015**, *6*, 1904–1926.

[20] S. Engmann, M. Stano, S. Matejčík, O. Ingólfsson, *Physical chemistry chemical physics : PCCP* **2012**, *14*, 14611–8.

[21] J. D. Wnuk, J. M. Gorham, S. G. Rosenberg, W. F. van Dorp, T. E. Madey, C. W. Hagen, D. H. Fairbrother, *The Journal of Physical Chemistry C* **2009**, *113*, 2487–2496.

[22] S. J. Randolph, J. D. Fowlkes, P. D. Rack, *Critical Reviews in Solid State and Materials Sciences* **2006**, *31*, 55–89.

[23] J. Schaefer, J. Hoelzl, *Thin Solid Films* **1972**, *13*, 81–86.

[24] A. Botman, D. A. M. de Winter, J. J. L. Mulders, *Journal of Vacuum Science & Technology B: Microelectronics and Nanometer Structures* **2008**, *26*, 2460–2463.

[25] P. C. Hoyle, J. R. A. Cleaver, H. Ahmed, *Applied Physics Letters* **1994**, *64*, 1448–1450.

[26] S. Engmann, M. Stano, P. Papp, M. J. Brunger, Š. Matejčík, O. Ingólfsson, *The Journal of Chemical Physics* **2013**, *138*, 044305.

[27] O. May, D. Kubala, M. Allan, A. A. Viggiano, G. K. Rekha, A. E. Stevens, G. A. Tolstikov, *Phys. Chem. Chem. Phys.* **2012**, *14*, 2979–2982.

[28] K. Wnorowski, M. Stano, C. Matias, S. Denifl, W. Barszczewska, Š. Matejčík, *Rapid Communications in Mass Spectrometry* **2012**, *26*, 2093–2098.

[29] O. Ingólfsson in *Low-Energy Electrons: Fundamentals and Applications*, (Ed.: O. Ingólfsson), Pan Stanford Publishing Pte. Ltd., Singapore, **2019**, Chapter Low Energy, pp. 47–120.

[30] A. Knights, P. Coleman, *Applied Surface Science* **1995**, *85*, 43–48.

[31] Š Matejčík, V Foltin, M Stano, J. Skalný, *International Journal of Mass Spectrometry* **2003**, *223-224*, 9–19.

[32] R. Dressler, M. Allan, *Chemical Physics* **1985**, *92*, 449–455.

[33] E. H. Bjarnason, B. Ómarsson, S. Engmann, F. H. Ómarsson, O. Ingólfsson, *European Physical Journal D* **2014**, *68*, 121.

[34] S. G. Rosenberg, M. Barclay, D. H. Fairbrother, *The Journal of Physical Chemistry C* **2013**, *117*, 16053–16064.

[35] I. Ipolyi, W. Michaelis, P. Swiderek, *Phys. Chem. Chem. Phys.* **2007**, *9*, 180–191.

[36] J. F. Friedman, T. M. Miller, J. K. Friedman-Schaffer, A. A. Viggiano, G. K. Rekha, A. E. Stevens, *The Journal of Chemical Physics* **2008**, *128*, 104303.

[37] M Allan, *The Journal of chemical physics* **2011**, *134*, 204309.

[38] K. Landheer, S. G. Rosenberg, L. Bernau, P. Swiderek, I. Utke, C. W. Hagen, D. H. Fairbrother, *The Journal of Physical Chemistry C* **2011**, *115*, 17452–17463.

[39] S. Engmann, M. Stano, Š. Matejčík, O. Ingólfsson, *Journal of Physics: Conference Series* **2012**, *388*, 52019.

[40] K. Wnorowski, M. Stano, W. Barszczewska, A. Jówko, Š. Matejčík, *International Journal of Mass Spectrometry* **2012**, *314*, 42–48.

[41] S. G. Rosenberg, M. Barclay, D. H. Fairbrother, *Physical Chemistry Chemical Physics* **2013**, *15*, 4002–4015.

[42] R. M. Thorman, I. Unlu, K. Johnson, R. Bjornsson, L. McElwee-White, D. H. Fairbrother, O. Ingólfsson, *Physical Chemistry Chemical Physics* **2018**, *20*, 5644–5656.

[43] I. Unlu, J. A. Spencer, K. R. Johnson, R. M. Thorman, O. Ingólfsson, L. McElwee-White, D. H. Fairbrother, *Physical Chemistry Chemical Physics* **2018**, *20*, 7862–7874.

[44] R. M. Thorman, J. A. Brannaka, L. McElwee-White, O. Ingólfsson, *Phys. Chem. Chem. Phys.* **2017**, *19*, 13264–13271.

[45] J. A. Spencer, J. A. Brannaka, M. Barclay, L. McElwee-White, D. H. Fairbrother, *The Journal of Physical Chemistry C* **2015**, *119*, 15349–15359.

[46] J. Jurczyk, C. R. Brewer, O. M. Hawkins, M. N. Polyakov, C. Kapusta, L. McElwee-White, I. Utke, *ACS Applied Materials & Interfaces* **2019**, *11*, 28164–28171.

[47] J. A. Spencer, Y.-C. Wu, L. McElwee-White, D. H. Fairbrother, *Journal of the American Chemical Society* **2016**, *138*, 9172–9182.

[48] F. Ferreira da Silva, R. M. Thorman, R. Bjornsson, H. Lu, L. McElwee-White, O. Ingólfsson, *Physical Chemistry Chemical Physics* **2020**, *22*, 6100–6108.

[49] R. K. T P, S. Barth, R. Bjornsson, O. Ingólfsson, *European Physical Journal D* **2016**, *70*, 163.

[50] R. K. T. P., I. Unlu, S. Barth, O. Ingólfsson, D. H. Fairbrother, *The Journal of Physical Chemistry C* **2018**, *122*, 2648–2660.

[51] R. K. T. P., P. Weirich, L. Hrachowina, M. Hanefeld, R. Bjornsson, H. R. Hrodmarsson, S. Barth, D. H. Fairbrother, M. Huth, O. Ingólfsson, *Beilstein Journal of Nanotechnology* **2018**, *9*, 555–579.

[52] J. Melngailis, *Journal of Vacuum Science & Technology B: Microelectronics and Nanometer Structures* **1987**, *5*, 469.

[53] A. D. Dubner, A. Wagner, J. Melngailis, C. V. Thompson, *Journal of Applied Physics* **1991**, *70*, 665–673.

[54] J. S. Ro, C. V. Thompson, J. Melngailis, *Journal of Vacuum Science & Technology B: Microelectronics and Nanometer Structures* **1994**, *12*, 73.

[55] S. Lipp, L. Frey, C. Lehrer, E. Demm, S. Pauthner, H. Ryssel, *Microelectronics Reliability* **1996**, *36*, 1779–1782.

[56] R. M. Thorman, S. J. Matsuda, L. McElwee-White, D. H. Fairbrother, *The Journal of Physical Chemistry Letters* **2020**, *11*, 2006–2013.

[57] J. H. Noh, M. G. Stanford, B. B. Lewis, J. D. Fowlkes, H. Plank, P. D. Rack, *Applied Physics A* **2014**, *117*, 1705–1713.

[58] J. A. Spencer, S. G. Rosenberg, M. Barclay, Y.-C. Wu, L. McElwee-White, D. Howard Fairbrother, *Applied Physics A* **2014**, *117*, 1631–1644.

[59] J. A. Spencer, M. Barclay, M. J. Gallagher, R. Winkler, I. Unlu, Y.-C. Wu, H. Plank, L. McElwee-White, D. H. Fairbrother, *Beilstein Journal of Nanotechnology* **2017**, *8*, 2410–2424.

[60] F. Calderazzo, F. L. Eplattenier, *Inorganic Chemistry* **1967**, *6*, 1220–1224.

[61] B. F. G. Johnson, R. D. Johnston, J. Lewis, *Journal of the Chemical Society A: Inorganic Physical Theoretical* **1969**, 792.

[62] S. Saha, B. Captain, *Inorganic Chemistry* **2014**, *53*, 1210–1216.

[63] M Braun, S Marienfeld, M.-W. Ruf, H Hotop, *Journal of Physics B: Atomic Molecular and Optical Physics* **2009**, *42*, 125202.

[64] J. D. Wnuk, S. G. Rosenberg, J. M. Gorham, W. F. van Dorp, C. W. Hagen, D. H. Fairbrother, *Surface Science* **2011**, *605*, 257–266.

[65] S. G. Rosenberg, K. Landheer, C. W. Hagen, D. H. Fairbrother, *Journal of Vacuum Science & Technology B: Microelectronics and Nanometer Structures* **2012**, *30*, 051805.

[66] J. F. Moulder, J. Chastain, *Handbook of x-ray photoelectron spectroscopy : a reference book of standard spectra for identification and interpretation of XPS data*, Physical Electronics Division, Perkin-Elmer Corp, **1992**, p. 259.

[67] E. W. Plummer, W. R. Salaneck, J. S. Miller, *Physical Review B* **1978**, *18*, 1673–1701.

[68] D. J. Morgan, *Surface and Interface Analysis* **2015**, *47*, 1072–1079.

[69] H. Estrade-Szwarckopf, *Carbon* **2004**, *42*, 1713–1721.

[70] C. Bianchi, V. Ragaini, M. Cattania, *Materials Chemistry and Physics* **1991**, *29*, 297–306.

[71] H. W. Chen, W. L. Jolly, *Inorganic Chemistry* **1979**, *18*, 2548–2551.

[72] P. M. A. Sherwood, *Journal of the Chemical Society Faraday Transactions 2* **1976**, *72*, 1805.

[73] K. Li, Y. Zhao, P. Zhang, C. He, J. Deng, S. Ding, W. Shi, *Applied Surface Science* **2016**, *390*, 412–421.

[74] H.-D. Kim, H.-J. Noh, K. H. Kim, S.-J. Oh, *Physical Review Letters* **2004**, *93*, 126404.

[75] P. Cox, J. Goodenough, P. Tavener, D. Telles, R. Egdell, *Journal of Solid State Chemistry* **1986**, *62*, 360–370.

[76] M. Zhang, W. Chen, S.-J. Ding, Z.-Y. Liu, Y. Huang, Z.-W. Liao, D. W. Zhang, *Journal of Physics D: Applied Physics* **2008**, *41*, 032007.

[77]   D. Rochefort, P. Dabo, D. Guay, P. Sherwood, *Electrochimica Acta* **2003**, *48*, 4245–4252.

[78]   M. Allan, M. Lacko, P. Papp, Š. Matejčík, M. Zlatar, I. I. Fabrikant, J. Kočišek, J. Fedor, *Physical Chemistry Chemical Physics* **2018**, *20*, 11692–11701.

[79]   J. Yang, W. Cui, Y. Li, G. Xie, N. Zhang, R. Wang, T. Hu, H. Zhang, *Applied Surface Science* **2016**, *382*, 88–92.

[80]   S. G. Rosenberg, M. Barclay, D. H. Fairbrother, *ACS applied materials & interfaces* **2014**, *6*, 8590–601.

[81]   M. Zlatar, M. Allan, J. Fedor, *The Journal of Physical Chemistry C* **2016**, *120*, 10667–10674.

[82]   M. Mendes, K. Regeta, F. Ferreira da Silva, N. C. Jones, S. V. Hoffmann, G. García, C. Daniel, P. Limão-Vieira, *Beilstein Journal of Nanotechnology* **2017**, *8*, 2208–2218.

[83]   K. P. Kepp, *Inorganic Chemistry* **2016**, *55*, 9461–9470.

[84]   M. Rohdenburg, P. Martinović, K. Ahlenhoff, S. Koch, D. Emmrich, A. Gölzhäuser, P. Swiderek, *The Journal of Physical Chemistry C* **2019**, *123*, 21774–21787.

[85]   Y. Kaga, Y. Abe, H. Yanagisawa, M. Kawamura, K. Sasaki, *Surface Science Spectra* **1999**, *6*, 68–74.

Chapter 5

Electron and ion-induced surface reactions of Fe(CO)$_5$

This work was co-written with the following authors:

R. M. Thorman, M.S. Barclay, E. Bilgilisoy, and D. Howard Fairbrother

5.1   Introduction

The fabrication of ferromagnetic nanostructures is fundamental to both conventional and emerging fields,[1, 2] such as magnetic information storage,[3] spintronics,[4] and racetrack memory.[5] Currently, conventional optical and electron beam lithography techniques are the most common approaches used to produce ferromagnetic nanostructures, with electron beam lithography in particular being popular below the micron scale;[1] however, there are several drawbacks to the use of such techniques. Conventional lithography involves the use of masks and resists, and typically many steps are required in order to produce a three-dimensional nanostructure. Because of this, the resulting structure may be contaminated by undissolved resist or have a poorly defined

structure due to propagation of error from masks.

Focused electron beam induced deposition (FEBID) and focused ion beam induced deposition (FIBID) are potential alternatives to conventional lithographic techniques in the fabrication of such nanostructures.[1, 6, 7] Both of these techniques utilize the tight focus achievable with a high energy charged particle (electron or ion) beam in order to directly write three-dimensional nanostructures onto surfaces of any dimensionality (i.e., planar or nonplanar). In FEBID and FIBID, an organometallic precursor is introduced into a high vacuum (HV) chamber equipped with a high energy primary charged particle beam via a gas injection system that delivers the precursor molecules in close proximity to a substrate and the area of the impinging charged particle beam. The charged particle beam decomposes the transiently adsorbed precursor molecule and involatile fragments form a deposit on the substrate, while volatile fragments desorb into the vacuum. The lateral geometry of the deposit may be controlled by rastering the charged particle beam around the surface, while the vertical dimension may be controlled by variation of the dwell time. Both FEBID and FIBID have been used to produce a variety of three-dimensional ferromagnetic nanostructures composed of iron and cobalt from organometallic precursors such as $Fe(CO)_5$, $Co_2(CO)_8$, and $Co(CO)_3NO$.[1, 6]

In FEBID, fabrication of iron nanostructures has been performed using $Fe(CO)_5$,[1, 6, 8, 9] $Fe_3(CO)_{12}$,[10] $Fe_2(CO)_9$,[11] and $Fe(C_5H_5)_2$ (ferrocene).[12] Of these precursors, $Fe(CO)_5$ and $Fe_2(CO)_9$ have produced deposits with the highest iron purities (> 80 at. % Fe),[8, 9, 12] with carbon and oxygen as contaminants; $Fe(CO)_5$ is by far the most popular precursor used to deposit

iron in FEBID.[1, 6] By varying many deposition parameters, Gavagnin et al. were able to produce deposits with an iron-to-oxygen ratio of 11.8:1; assuming similar concentrations of carbon to oxygen, the purity of these deposits was about 85 at. % Fe.[8] To achieve pure iron deposition from $Fe(CO)_5$, Lukascyk et al. made deposits under ultra-high vacuum (UHV) conditions with purities of > 95 at. % Fe.[9] Conversely, although FIBID has been used to fabricate ferromagnetic cobalt nanostructures,[13] it has not been used extensively to deposit iron.[6] To our knowledge, the only iron deposits made with FIBID were micron-scale lines printed with a 50 kV Ga^+ focused ion beam using $Fe(CO)_5$ as a precursor, which achieved a maximum purity of 85 at. % Fe as measured by Auger electron spectroscopy.[14]

In order to improve the quality of FEBID and FIBID deposits, it is important to understand the electron- and ion-induced reactions that lead to deposition in FEBID and FIBID. In FEBID, low energy secondary electrons produced by interactions between the high energy primary electron beam and the surface are understood to initiate the precursor decomposition reactions that lead to deposition.[6, 15] Studies of the low energy electron-induced decomposition of adsorbed FEBID precursor molecules have typically found that the first deposition step in FEBID involves low energy electron-induced dissociation of one or more ligands from the precursor molecule, which desorb from the substrate. Two low energy electron-induced ligand dissociation reactions have been found to be especially important in FEBID: dissociative electron attachment (DEA) and dissociative ionization (DI).[15] In DEA, a low energy electron attaches to a precursor, forming a transient negative ion

137

which then dissociates into an anionic fragment and one or more neutral fragments. In DI, electron impact ionizes a precursor molecule, forming a cation which then dissociates into a cationic fragment and one or more neutral fragment. By comparing studies of the low energy electron-induced decomposition of adsorbed precursor molecules with those of gas phase precursor molecules, DEA and DI have both been found to initiate deposition in FEBID of precursor molecules such as $MeCpPtMe_3$ and $W(CO)_6$, respectively.[15–20] Other low energy electron-induced ligand dissociation reactions, neutral dissociation and dipolar dissociation, begin with electronic excitation of the parent molecule and may also be important in FEBID. After the initial electron-induced ligand loss step, continued electron exposure commonly causes ligand decomposition, rather than dissociation and desorption from the surface. Thus, any ligands that remain on the surface after the initial ligand loss step are incorporated into the deposit.

The reactions that lead to deposition in FIBID, however, are less well-understood. Secondary electrons produced by interactions between the high energy primary ion beam and the substrate may induce precursor decomposition that leads to deposition, as in FEBID; however, due to the significantly larger mass of ions compared to that of electrons, energy transfer from the primary beam to the substrate and precursor molecules is much more significant in FIBID than in FIBID. Thus, surface-mediated energy transfer between the primary ion beam and the precursor molecules, known as the collision cascade model, may also be responsible for deposition in FIBID.[7, 21] Previous FIBID experiments have correlated measurements of growth rate with

different parameters, such as nuclear and electronic stopping power[21, 22] and secondary electron and sputtering yields,[23–25] in order to determine whether the secondary electron model or the collision cascade model is the likely mechanism for deposition in FIBID. These studies have given evidence for both models of deposition and, taken together, are not conclusive. In order to better understand the reactions underlying deposition in FIBID, a recent paper published by several authors of the current study compared the low energy (< 1 kV) electron- and argon ion-induced decomposition reactions of thin films of adsorbed $CpFe(CO)_2Re(CO)_5$ on a cooled gold substrate.[26] This study found that the electron and argon ion-induced decomposition of adsorbed $CpFe(CO)_2Re(CO)_5$ were extremely different, giving support to the collision cascade model dominating deposition in the ion-limited regime of FIBID. In order to determine whether this is more generally applicable, more precursors must be examined using this approach and the surface experiments must be compared to gas phase and *in situ* FIBID experiments, as has been done for FEBID precursors.

In this regard, $Fe(CO)_5$ is a particularly well-studied precursor. Gas phase studies of the electron-induced reactions of $Fe(CO)_5$ include DEA, DI, and electronic excitation of $Fe(CO)_5$ molecules,[27, 28] as well as DEA and DI studies of $Fe(CO)_5$ clusters and $Fe(CO)_5$ clusters with Ar.[29, 30] Additionally, Indrajith et al. has recently studied the gas phase reactions of singly and multiply charged noble gas projectile ions (He, Ne, Ar, and Kr) at various incident energies with $Fe(CO)_5$.[31] On the surface, Hauchard et al. has used grazing incidence infrared (IR) spectroscopy to examine the kinetics of the

139

electron-induced decomposition of thin films of $Fe(CO)_5$ adsorbed on cooled (45 K) Au(111)/mica and exposed to 1 - 20 eV electrons,[32] while Massey et al. has used mass spectrometry (MS) to study the desorption of charged fragments from thin films of $Fe(CO)_5$ adsorbed on cooled (40 K) condensed Xe or Pt foil and exposed to 4 - 33 eV electrons.[33] Taken together, such studies may be used to bridge the gap between the single-collision electron or ion-induced decomposition of $Fe(CO)_5$ in the gas phase and the complex multitude of electron- and ion-induced reactions that occur in FEBID and FIBID.

With this aim, the low energy electron- (500 eV) and argon ion- (1200 - 3000 eV) induced decomposition of thin films of adsorbed $Fe(CO)_5$ on a cooled (143 K) Au substrate were studied and compared to previous gas phase and surface studies in order to elucidate the molecular-level reactions that lead to deposition in FEBID and FIBID using $Fe(CO)_5$. The kinetics of low energy electron-induced deposition of adsorbed $Fe(CO)_5$ were also studied, showing the fundamental reactions that lead to iron oxide deposition from $Fe(CO)_5$ in FEBID. Additionally, deposits were made from $Fe(CO)_5$ using ion beam induced deposition (IBID) in a UHV chamber with three different incident beam energies (800, 1200, and 1600 eV), showing that pure iron deposits may be made with low energy IBID using $Fe(CO)_5$.

5.2 Experimental Methods

5.2.1 Surface studies

Surface studies were performed in a UHV chamber with a base pressure below 4×10^{-9} Torr and equipped with X-ray photoelectron spectroscopy (XPS), mass spectrometry (MS), a flood electron gun, and an ion gun. Iron pentacarbonyl (> 99.99 %, Sigma Aldrich), which is a brown, transparent liquid at room temperature, was introduced into the UHV chamber via a leak valve and dosed for 5 - 7 minutes in order to form 1.8 – 2.6 nm thin films on a gold substrate cooled to 143 ± 5 K. Film thickness was measured by XPS.

X-ray photoelectron spectroscopy was performed using a PHI 5400 XPS with a Mg Kα (hν = 1254 eV) anode. Spectra were calibrated using the Au 4f$_{7/2}$ peak associated with the substrate (BE = 84.0 eV)[34] and processed using CasaXPS, a commercially available software. The electron source used during the electron irradiation studies was a Specs FG 15/40. The ion gun used in argon ion irradiation studies was a Perkin-Elmer PHI model 04-303 differentially pumped ion gun.

During both the electron and argon ion irradiation studies, the substrate was biased by +20 V in order to ensure that all secondary electrons generated by electron or argon ion irradiation remained on the substrate, and the respective beams were defocused to ensure that the entire 1 cm^2 surface was exposed to ions or electrons. In the electron irradiation studies, a primary electron beam energy of +480 eV was used, producing an incident electron energy of +500 eV, and the target current was maintained at 30 μA. The electron beam

was oriented along the surface normal of the sample. Electron irradiation is reported in terms of electron dose (e^-/cm^2) and current density (mC/cm^2). In the argon ion irradiation studies, primary beam energies of +1.2 kV and +3 kV were used, producing an incident argon ion energy of +1.18 kV and +2.98 kV. The argon ion beam was oriented at approximately $45°$ from the surface normal. Argon ion irradiation is reported in terms of irradiation time (s).

5.2.2   Ion beam deposition studies

Ion beam induced deposition (IBID) was performed at room temperature in a UHV chamber (base pressure $\cong$ 1 - 2 x 10^{-8} Torr) equipped with a PHI model 04-303 differentially pumped ion gun. Argon gas was introduced into the chamber at a partial pressure of 2 - 3 x 10^{-8} Torr (P_{total} = 4 x 10^{-8} Torr) with an ion gun emission current of 25 mA. Three different beam energies were used during deposition: 800, 1200, and 1600 eV. The precursor was introduced into the chamber using a UHV-compatible leak valve attached to a small capillary used as a directional doser intended to increase the partial pressure of $Fe(CO)_5$ close to the substrate surface. During all IBID experiments, the total system pressure was maintained at 5 x 10^{-7} Torr during deposition, which lasted for 18 hours. The substrate used for all IBID studies was Si <100> with a native oxide layer. Substrates were rotated during deposition such that the argon ion beam was approximately normal to the substrate surface.

5.3 Results and discussion

5.3.1 Electron beam studies

Figure 5.1 shows the evolution of the C (1s), O (1s), and Fe (2p) XPS regions of adsorbed thin films (1.8 - 2.6 nm) of $Fe(CO)_5$ upon irradiation with 500 eV electrons. Previous control studies have shown that adsorbed $Fe(CO)_5$ thin films were unaltered by X-rays over the irradiation times required to acquire XPS spectra. The C (1s) region is initially characterized by 2 peaks: a high intensity peak at 287.5 eV and a lower intensity, higher binding energy peak at 293.1 eV. The C (1s) peaks associated with the unirradiated precursor are shown as solid red curves. The high intensity peak at 287.5 eV is assigned to the CO ligand, while the lower intensity peak at 293.1 eV constitutes a π-π* shakeup peak, which is typical for adsorbed metal carbonyls.[35] Before electron irradiation, the O (1s) region is characterized by three peaks, which have not been deconvoluted in this figure. Two of these peaks overlap significantly, forming a larger, asymmetrical peak centered at approximately 533.6 eV. These are assigned to the CO ligands,[36] and the asymmetry is similar to that previously been observed in CO adsorbed on Fe(100).[37] The third, higher binding energy peak at 539.6 eV is the CO π-π* shakeup peak.[35] The Fe (2p) region is initially characterized by two peaks at approximately 708.8 and 721.7 eV, corresponding to the Fe ($2p_{3/2}$) and Fe ($2p_{1/2}$) transitions, respectively.[36, 38] The spectra shown in the C (1s) and O (1s) regions have had their respective backgrounds removed; due to the complexity of background subtraction in the Fe (2p) region, the background is shown as a green curve in these spectra.
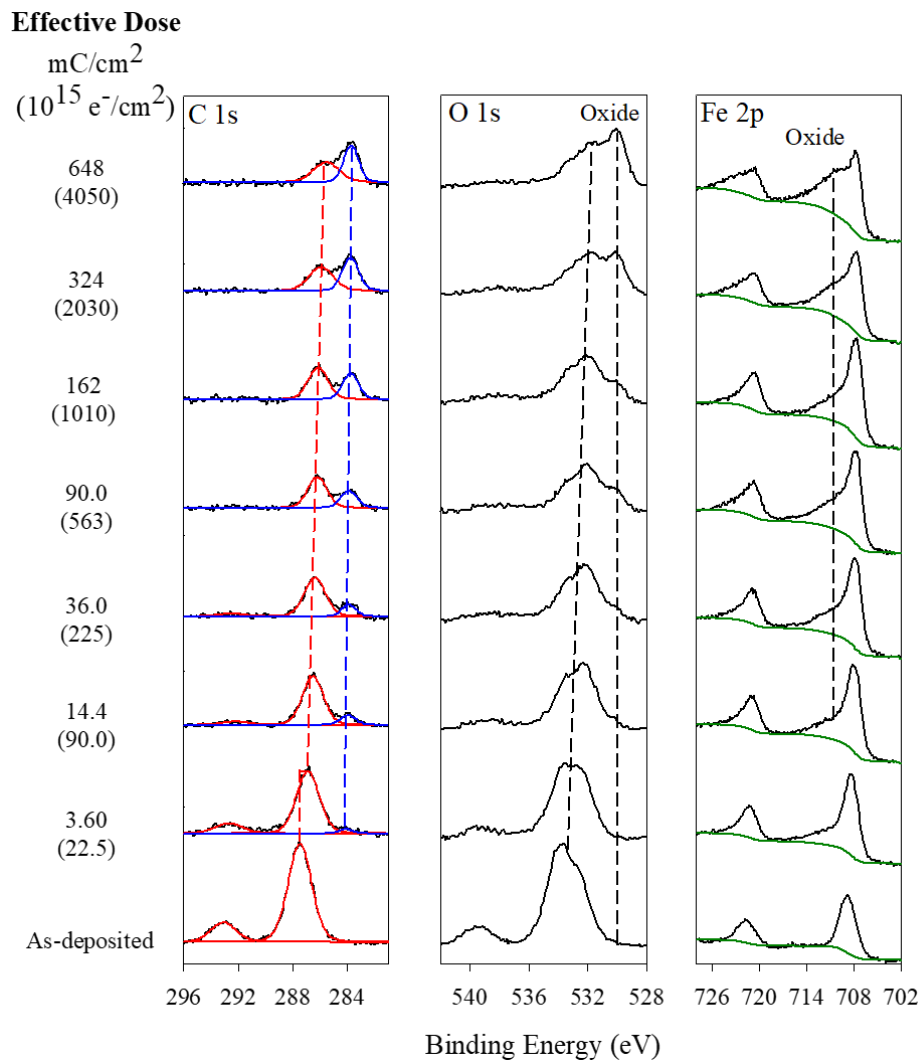
Figure 5.1: Evolution of the C(1s), O(1s), and Fe(2p) XPS regions of ≈ 1.8 - 2.6 nm thin films of adsorbed Fe(CO)$_5$ upon irradiation with 500 eV electrons. The bottom spectra represent the as-deposited, un-irradiated film. Speciation is shown in the C(1s) region, where the red line represents the C(1s) peak associated with the precursor carbonyl ligands while the blue lines represent the C(1s) peak associated with the graphitic carbon species in the deposit. The dashed red and blue lines in this region show the change in binding energy of these peaks during electron irradiation. The black dashed lines in the O(1s) and Fe(2p) regions indicate oxide growth. The green curves in the Fe(2p) region show the background. Electron dose is shown on the left-hand side in units of mC/Cm^2 and, in parentheses, 10^{15} e$^-$/cm^2.

Upon irradiation with 500 eV electrons, both peaks in the C (1s) region decrease in intensity; after an electron dose of 3.60 mC/cm^2, the CO peak at 287.5 eV has shifted to a lower binding energy of 286.8 eV. Concurrently, a new lower binding energy peak appears at approximately 284.1 eV; this peak is shown in Fig. 1 as a blue curve. The binding energy of this peak suggests that it is associated with graphitic carbon species. Continued electron irradiation causes the peaks associated with the carbonyl ligands to continue to decrease in intensity and shift to lower binding energy, while the lower binding energy graphitic carbon peak simultaneously increases in intensity and shifts to slightly lower binding energy. After an effective dose of 648 mC/cm^2, the C (1s) region is characterized by two peaks of similar intensity: one at 285.5 eV associated with the remaining CO species and a second at 283.7 eV associated with the graphitic carbon species.[20]

Electron irradiation similarly causes the asymmetrical main O (1s) peak associated with the CO oxygen species to decrease in intensity and shift to slightly lower binding energy. At the same time, a lower binding energy peak grows in at approximately 530.2 eV, which is likely associated with oxide species. This peak, shown in Fig. 5.1 with a black dashed line labelled 'oxide', becomes evident after an electron dose of about 14.4 mC/cm^2; similar to the graphitic carbon species seen in the C (1s) region. Continued electron irradiation causes the oxide O (1s) peak to increase in intensity, as the main O (1s) peak associated with the CO oxygen species simultaneously decreases in intensity and shifts to lower binding energy. After an effective electron dose of 640 mC/cm^2, the O (1s) region is characterized by a relatively narrow oxide

peak at 529.9 eV,[39] as well as a broader peak centered at approximately 531.7 eV associated with the remaining CO species.

In the Fe (2p) region, electron irradiation causes the Fe (2p) peaks to shift to slightly lower binding energy and broaden significantly. As the lower binding energy oxide peak grows in the O (1s) region, a higher binding energy shoulder grows in the Fe (2p) region. This shoulder initially appears after about 14.4 mC/cm^2 of electron irradiation and becomes increasingly intense with increased electron irradiation. After an electron dose of 640 mC/cm^2, the Fe (2p) region is characterized by two peaks at 707.8 and 720.7 eV, which again correspond to the Fe ($2p_{3/2}$) and Fe ($2p_{1/2}$) peaks, respectively. This is close in binding energy to metallic iron XPS peaks.[38] The higher binding energy shoulder on the Fe ($2p_{3/2}$) peak has a maximum intensity at approximately 710.3 eV, associated with iron oxide species.[39, 40] No loss of iron from the surface is observed upon electron irradiation.

Figure 5.2 shows the number of CO ligands remaining on the substrate as measured by total carbon coverage (light green filled circles) and total oxygen coverage (dark green open circles) as a function of electron dose in mC/cm^2 (bottom axis) and e$^-$/cm^2 (top axis). Initially, 5 CO ligands are present in the adsorbed Fe(CO)$_5$ species; upon electron irradiation, this quickly decreases. After an electron dose of about 20 mC/cm^2, only about 2 - 3 CO ligands remain on the surface and further electron irradiation does not change the number of remaining CO ligands. As can be seen in Fig. 5.2, the number of CO ligands remaining on the surface as measured by total oxygen coverage (about 3) is slightly higher than the number measured by total carbon coverage (about

Figure 5.2: Number of CO ligands remaining as a function of electron dose, for Fe(CO)$_5$ films exposed to 500 eV electrons. The number of CO ligands remaining is measured both as by the total carbon coverage (light green filled circles) and total oxygen coverage (dark green open circles). Effective electron dose is expressed in units of mC/Cm^2 (main axis) and e$^-$/cm^2 (top axis).

2). It is possible that, due to the higher relative sensitivity factor of the O (1s) signal compared to the C (1s) signal, the total oxygen coverage may be a more reliable indicator of the remaining CO; however, it is also possible that the O (1s) signal from the precursor molecule is obscured by the presence of adventitious adsorbed water. We thus consider these two measures (total carbon and total oxygen) to be the boundaries for the number of CO ligands removed from the surface during electron irradiation.

Examining Figs. 5.1 and 5.2 together, it is evident that the electron-induced decomposition of adsorbed thin films of Fe(CO)$_5$ proceeds in two regimes,

similarly to other carbonyl-containing organometallic species. The first regime, taking place at electron doses $< 14.4 \text{ mC/cm}^2$, is characterized primarily by the loss of 2 - 3 CO ligands and can be described as:

$$Fe(CO)_{5(ads)} + e^- (500eV) \xrightarrow{k_1} Fe(CO)_{5-x(ads)} + xCO_{(g)} \uparrow \qquad (5.1)$$
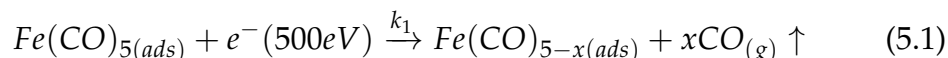
Here, k_1 is the rate constant of the reaction described in Equation 5.1, and x is the number of CO ligands lost (x = 2 - 3) in this initial reaction step. The formula of the adsorbed product ($Fe(CO)_{5-x(ads)}$) represents a stoichiometric average of a range of different $Fe_y(CO)_z$ species produced in Eq. 5.1, rather than denoting a specific bonding structure, and $Fe(CO)_{5-x(ads)}$ is best viewed as a partially decarbonylated intermediate. As denoted by Hauchard et al, some of these complexes may by produced by electron interaction with aggregates of $Fe(CO)_5$,[32] rather than the single adsorbed $Fe(CO)_5$ molecule shown in Eq. 5.1.

Gas phase studies of the low energy electron-induced decomposition of molecular $Fe(CO)_5$ and $Fe(CO)_5$ clusters can be used to understand the mechanism underlying this initial reaction step. For molecular $Fe(CO)_5$, DEA has been found to lead primarily to single CO loss (producing $[Fe(CO)_4]^-$),[27] while DI has been found to produce significantly more fragmentation, with $[Fe(CO)]^+$ and Fe^+ being the most intense fragments observed at 70 eV incident electron energy.[28] In pure $Fe(CO)_5$ clusters, $Fe(CO)_5$ aggregates on Ar clusters, and $Fe(CO)_5$ films on condensed xenon on platinum foil, DEA at the lowest incident energies (close to 0 eV) has been found to be suppressed,[30, 33] while DI with significant ligand loss is still observed.[29, 33] Thus, it is

148

likely that DI is responsible for this initial reaction step, which as a statistical process likely produces a range of $Fe_y(CO)_z$ species.

The second electron-induced decomposition step takes place at electron doses $> 14.4 \, mC/cm^2$ and is characterized by decomposition of the CO ligands that remain after the initial ligand loss step. In this regime, as can be seen in Fig. 5.2, no carbon or oxygen is removed from the surface. Instead, as can be seen in Fig. 5.1, the remaining CO ligands are decomposed into a graphitic carbon species and a reactive oxygen species, which oxidizes the iron. This set of reactions can be described as:

$$Fe(CO)_{5-x(ads)} + e^- (500eV) \xrightarrow{k_2} FeO_{5-x(ads)} + (5-x)C_{(graphitic)} \qquad (5.2)$$
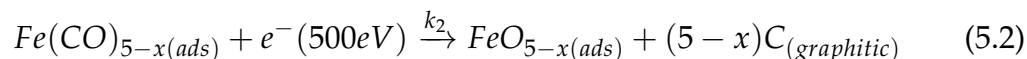
Here, k_2 is the rate constant of the reaction described in Equation 5.2. The formula of the oxidized iron product ($FeO_{5-x(ads)}$) is meant to be stoichiometric and represents a mix of iron oxides and unoxidized iron species that remain on the surface.

The proposed mechanism for the electron-induced decomposition of adsorbed $Fe(CO)_5$ - i.e., a two step process consisting of an initial CO loss followed by decomposition of the remaining CO ligands - is common to many metal carbonyls and carbonyl-containing organometallic precursors, including $Co(CO)_3NO$, $W(CO)_6$, $HFeCo_3(CO)_{12}$, $CpFe(CO)_2Mn(CO)_5$, and $CpFe(CO)_2Re(CO)_5$.[20, 26, 41–43] Because $Fe(CO)_5$ has only a single type of ligand (CO) and none of the relevant XPS regions overlap, the C (1s) and O (1s) regions for these reactions are relatively simple to deconvolute (Fig. 5.1).

This allows the rate constants (k_1 and k_2) for these reactions to be determined.

In order to derive k_1 from Eq. 5.1, we can write:

$$\frac{d[Fe(CO)_5]}{dt} = -k_1[Fe(CO)_5] \tag{5.3}$$

$$\int_0^t \frac{d[Fe(CO)_5]}{[Fe(CO)_5]} = -k_1 \int_0^t dt$$

$$\ln\left(\frac{[Fe(CO)_5]_t}{[Fe(CO)_5]_0}\right) = -k_1 t$$

$$\frac{[Fe(CO)_5]_t}{[Fe(CO)_5]_0} = e^{-k_1 t} \tag{5.4}$$

Here, t is the electron dose, which may be given in mC/cm^2, $e\text{-}/cm^2$, or irradiation time (s).

Since both carbon and oxygen are lost from the surface during the initial step (Eq. 5.1), but not during the second step (Eq. 5.2), total carbon and total oxygen coverage can each be used to determine the rate of $Fe(CO)_5$ loss from the surface. The equations used to determine k_1 from the total carbon coverage will be given here as an illustrative example; however, the equations used with total oxygen will be the same.

As iron is not lost from the surface during electron irradiation (Fig. 5.1), conservation of mass requires that:

$$[Fe(CO)_5]_0 = [Fe(CO)_5]_t + [Fe(CO)_{5-x}]_t + [FeO_{5-x}]_t \tag{5.5}$$

As the initial carbon coverage is equal to five times the iron coverage and

150

carbon is not lost from the surface in the second step (Eq. 5.2):

$$[C_{total}]_t = 5[Fe(CO)_5]_t + (5 - x)\left([Fe(CO)_{5-x}]_t + [FeO_{5-x}]_t\right) \tag{5.6}$$

$$[C_{total}]_0 = 5[Fe(CO)_5]_0 \tag{5.7}$$

Taking Eq. 5.3, 5.6, and 5.7 together, we can thus write:

$$\frac{[C_{total}]_t}{[C_{total}]_0} = \frac{x}{5}e^{-k_1 t} + \frac{5 - x}{5} \tag{5.8}$$

Using this equation, we can plot the total carbon loss as a function of electron dose and fit a first order exponential decay function of the form y = $y_0 + ae^{-bx}$ in order to determine k_1 and x. This plot found a k_1 value of 0.2821 cm^2/mC (0.0085 s^{-1}, 4.5 x 10^{-17} cm^2, 0.45 Å^2) and an x value of 3.033.

In order to determine k_2, we can either plot the loss of the CO C (1s) peak (red curves in Fig. 5.1) or the growth of the graphitic C (1s) peak (blue curves in Fig. 5.1) and solve for k_2 based on the known quantities of k_1 and x. Both approaches begin by writing from Eq. 5.1 and 5.2:

$$\frac{d[Fe(CO)_5 - x]}{dt} = k_1[Fe(CO)_5] - k_2[Fe(CO)_{5-x}] \tag{5.9}$$

We can then substitute in our solution from Eq. 5.8 and rearrange to find:

$$\frac{d[Fe(CO)_{5-x}]}{dt} = k_1[Fe(CO)_5]_0 e^{-k_1 t} - k_2[Fe(CO)_{5-x}]$$

$$\frac{d[Fe(CO)_{5-x}]}{dt} + k_2[Fe(CO)_{5-x}] = k_1[Fe(CO)_5]_0 e^{-k_1 t}$$

Each side of the equation can then be multiplied by an integration factor and rearranged, to get:

$$\left(\frac{d[Fe(CO)_{5-x}]}{dt} + k_2[Fe(CO)_{5-x}]\right) e^{k_2 t} = k_1[Fe(CO)_5]_0 e^{-k_1 t} e^{k_2 t}$$

$$e^{k_2 t}\frac{d[Fe(CO)_{5-x}]}{dt} + [Fe(CO)_{5-x}]k_2 e^{k_2 t} = k_1[Fe(CO)_5]_0 e^{(k_2 - k_1)t}$$

$$e^{k_2 t}d[Fe(CO)_{5-x}] + [Fe(CO)_{5-x}]k_2 e^{k_2 t}dt = k_1[Fe(CO)_5]_0 e^{(k_2 - k_1)t}dt$$

The left-hand side of the above equation can be written as:

$$e^{k_2 t}d[Fe(CO)_{5-x}] + [Fe(CO)_{5-x}]k_2 e^{k_2 t}dt = xdy + ydx$$

$$= d(xy) = d([Fe(CO)_{5-x}]e^{k_2 t})$$

Where:

$$x = e^{k_2 t}; y = [Fe(CO)_{5-x}]$$

Thus:

$$\int_0^t d([Fe(CO)_{5-x}]e^{k_2 t}) = k_1[Fe(CO)_5]_0 \int_0^t e^{(k_2-k_1)t}dt$$

$$[Fe(CO)_{5-x}]_t e^{k_2 t} = [Fe(CO)_5]_0 \frac{k_1}{k_2-k_1}\left(e^{(k_2-k_1)t}-1\right)$$

$$[Fe(CO)_{5-x}]_t = [Fe(CO)_5]_0 \frac{k_1}{k_2-k_1}\left(e^{(k_2-k_1)t}-1\right)e^{-k_2 t}$$

$$[Fe(CO)_{5-x}]_t = [Fe(CO)_5]_0 \frac{k_1}{k_2-k_1}\left(e^{-k_1 t}-e^{-k_2 t}\right) \qquad (5.10)$$

In order to determine k_2 from the loss of the CO C (1s) peak, we can then relate the remaining CO carbon on the surface to the quantity of $Fe(CO)_5$ and $Fe(CO)_{5-x}$ remaining on the surface using Eq. 5.1 and 5.2:

$$[C_{CO}]_t = 5[Fe(CO)_5]_t + (5-x)[Fe(CO)_{5-x}]_t \qquad (5.11)$$

Then, we can substitute in Eq. 5.3 and 5.10 to obtain:

$$[C_{CO}]_t = 5[Fe(CO)_5]_0 e^{-k_1 t} + (5-x)[Fe(CO)_5]_0 \frac{k_1}{k_2-k_1}\left(e^{-k_1 t}-e^{-k_2 t}\right)$$

$$(5.12)$$

From here, we can substitute in Eq. 5.7 and rearrange to determine that:

$$[C_{CO}]_t = [C_{total}]_0 e^{-k_1 t} - \frac{5-x}{5}[C_{total}]_0 \frac{k_1}{k_2 - k_1}\left(e^{-k_1 t} - e^{-k_2 t}\right)$$

$$\frac{[C_{CO}]_t}{[C_{total}]_0} = e^{-k_1 t} - \frac{5-x}{5}\left(\frac{k_1}{k_2 - k_1}\right)\left(e^{-k_1 t} - e^{-k_2 t}\right)$$

$$\frac{[C_{CO}]_t}{[C_{total}]_0} = \left(\frac{5-x}{5}\left(\frac{k_1}{k_2 - k_1}\right) + 1\right)e^{-k_1 t} - \frac{5-x}{5}\left(\frac{k_1}{k_2 - k_1}\right)e^{-k_2 t} \qquad (5.13)$$

Thus, we can plot the carbonyl carbon loss as a function of electron dose and fit an exponential decay function of the form y = ae^{-bx} + ce^{-dx} in order to determine k_2. Using the previously-determined k_1 value of 0.2821 cm^2/mC (0.0085 s^{-1}, 4.5 x 10^{-17} cm^2, 0.45 Å^2) and x value of 3.033, the carbonyl carbon loss data was fit to find a k_2 value of 0.002006 cm^2/mC (0.000060 s^{-1}, 3.2 x 10^{-19} cm^2, 0.0032 Å^2).

If we instead wish to determine k_2 from the growth of the graphitic C (1s) peak, we can return to our branching point at Eq. 5.10 and write an equation for the rate of iron oxide formation. First, we can rewrite Eq. 5.5 as:

$$[FeO_{5-x}]_t = [Fe(CO)_5]_0 - [Fe(CO)_5]_t - [Fe(CO)_{5-x}]_t \qquad (5.14)$$

Then, we can substitute in Eq. 5.3 and 5.10:

$$[FeO_{5-x}]_t = [Fe(CO)_5]_0 - [Fe(CO)_5]_0 e^{-k_1 t} \qquad (5.15)$$

$$- [Fe(CO)_5]_0 \frac{k_1}{k_2 - k_1}\left(e^{-k_1 t} - e^{-k_2 t}\right)$$

From here, we can rearrange to determine that:

$$[FeO_{5-x}]_t = [Fe(CO)_5]_0 \left(1 - e^{-k_1 t} - \frac{k_1}{k_2 - k_1} \left(e^{-k_1 t} - e^{-k_2 t}\right)\right)$$

$$[FeO_{5-x}]_t = [Fe(CO)_5]_0 \left(1 - \left(\frac{k_1}{k_2 - k_1} + 1\right) e^{-k_1 t} + \left(\frac{k_1}{k_2 - k_1}\right) e^{-k_2 t}\right)$$

(5.16)

As no carbon is lost from the surface in Eq. 5.2, we can rewrite Eq. 5.16 as a function of graphitic carbon using:

$$[C_{graphitic}]_t = (5 - x)[FeO_{5-x}]_t$$

(5.17)

Substituting Eq. 5.7 and 5.17 into Eq. 5.16, we find:

$$\frac{[C_{graphitic}]_t}{5 - x} = \frac{[C_{total}]_0}{5} \left(1 - \left(\frac{k_1}{k_2 - k_1} + 1\right) e^{-k_1 t} + \left(\frac{k_1}{k_2 - k_1}\right) e^{-k_2 t}\right)$$

$$\frac{[C_{graphitic}]_t}{[C_{total}]_0} = \frac{5 - x}{5} \left(1 - \left(\frac{k_1}{k_2 - k_1} + 1\right) e^{-k_1 t} + \left(\frac{k_1}{k_2 - k_1}\right) e^{-k_2 t}\right)$$

$$\frac{[C_{graphitic}]_t}{[C_{total}]_0} = \frac{5 - x}{5} - \frac{5 - x}{5} \left(\frac{k_1}{k_2 - k_1} + 1\right) e^{-k_1 t} + \frac{5 - x}{5} \left(\frac{k_1}{k_2 - k_1}\right) e^{-k_2 t}$$

(5.18)

Thus, we can plot the graphitic carbon loss as a function of electron dose and fit an exponential decay function of the form $y = y_0 + ae^{-bx} + ce^{-dx}$ in order to determine k_2. Using the previously-determined k_1 and x values, the graphitic carbon growth data was fit to find a k_2 value of 0.001925 cm^2/mC (0.000058 s^{-1}, 3.1 x 10^{-19} cm^2, 0.0034 Å^2).
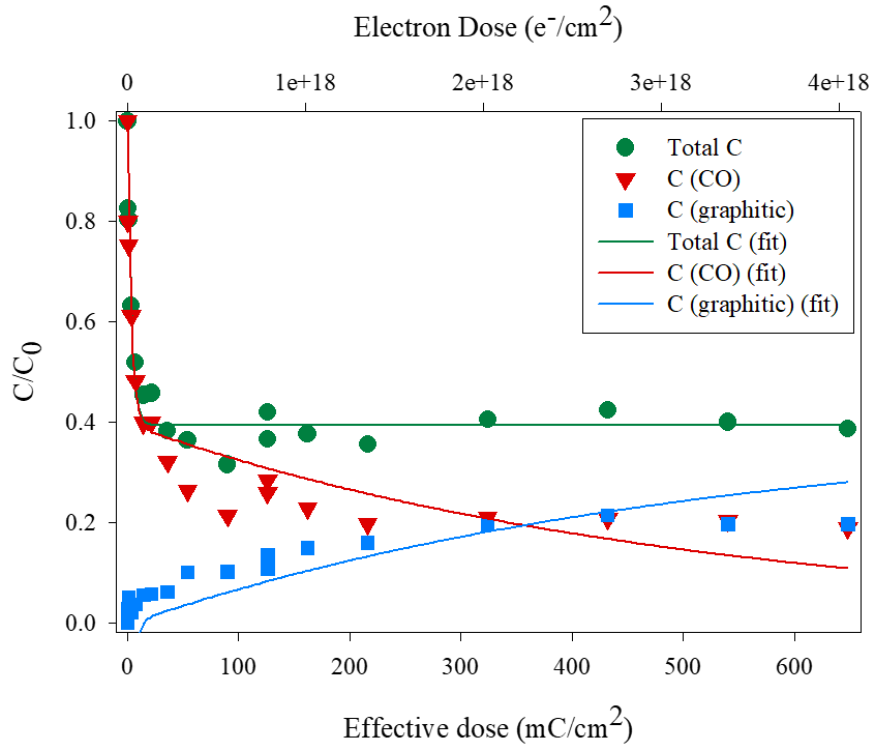
Figure 5.3: Kinetics of total carbon loss (green filled circles), carbonyl carbon loss (red filled triangles), and graphitic carbon growth (blue filled squares) fitted with Eq. 5.8 (green line), 5.13 (red line), and 5.18 (blue line), respectively. Effective electron dose is expressed in units of mC/Cm^2 (main axis) and e^-/cm^2 (top axis).

Figure 3 shows plots of total carbon loss (green filled circles), carbonyl carbon loss (red filled triangles), and graphitic carbon growth (blue filled squares) fitted with Eq. 5.8 (green line), 5.13 (red line), and 5.18 (blue line), respectively. The total carbon loss data was used to find a k_1 value of 0.2821 cm^2/mC (0.0085 s^{-1}, 4.5 x 10^{-17} cm^2, 0.45 $Å^2$) and an x value of 3.033. The carbonyl carbon loss data was fit to find a k_2 value of 0.002006 cm^2/mC (0.000060 s^{-1}, 3.2 x 10^{-19} cm^2, 0.0032 $Å^2$), while the graphitic carbon growth data was fit to find a k_2 value of 0.001925 cm^2/mC (0.000058 s^{-1}, 3.1 x 10^{-19}

156

cm^2, 0.0034 Å^2). There is thus fairly good agreement between the k_2 values found using the total carbonyl carbon loss and graphitic carbon growth data.

Previous work by Hauchard and Rowntree used grazing incidence IR spectroscopy to find cross sections as a function of incident electron energy for two sequential electron-induced reactions of adsorbed thin films of $Fe(CO)_5$ on a cooled (45 K) Au(111)/mica substrate exposed to 1 - 20 eV electrons.[32] At an incident electron energy of 20 eV using 5 Langmuir films, they found a cross section for the first reaction of 270 Å^2 and for the second reaction of 11.5 Å^2. This is significantly higher than the cross sections found in this work. However, Hauchard and Rowntree found that heating their $Fe(CO)_5$ films to 140 K and re-cooling to 45 K caused a restructuring in the $Fe(CO)_5$ film that the authors ascribe to aggregation. This restructuring was found to massively decrease the sensitivity of the $Fe(CO)_5$ films to electron irradiation; according to the authors estimate, it reduced the apparent cross section by 2-3 orders of magnitude. Thus, our observation of cross sections that are approximately 3 orders of magnitude lower than those determined by Hauchard and Rowntree align well with that estimation. This may be ascribed to the suppression of DEA in clustered $Fe(CO)_5$, as discussed previously;[30, 33] however, the appearance energies for fragments produced by DI were found to increase upon clustering[29] and in adsorbed thin films on Xe,[33] where the desorption thresholds for several iron-centered fragments were above 20 eV. Thus, the increase in aggregation of $Fe(CO)_5$ on the surface may also decrease the total cross section for DI by shifting the appearance energies for DI fragments, leading to the decreased cross section observed in this work.

157

Figure 5.4: Evolution of the C(1s), O(1s), and Fe(2p) XPS regions of $\approx$ 1.8 nm thin film of adsorbed Fe(CO)$_5$ upon irradiation with 1200 eV argon ions. The bottom spectra represent the un-irradiated film. Speciation is shown in the C(1s) region, where the red line represents the C(1s) peak associated with the precursor carbonyl ligands while the blue lines represent the C(1s) peak associated with the graphitic carbon species in the deposit. The black dashed lines in the O(1s) and Fe(2p) regions indicate oxide growth. The green curves in the Fe(2p) region shows the background. Ion dose is shown on the left-hand side in units of seconds.

5.3.2 Ion beam studies

Figures 5.4 and 5.5 show the evolution of the C (1s), O (1s), and Fe (2p) XPS

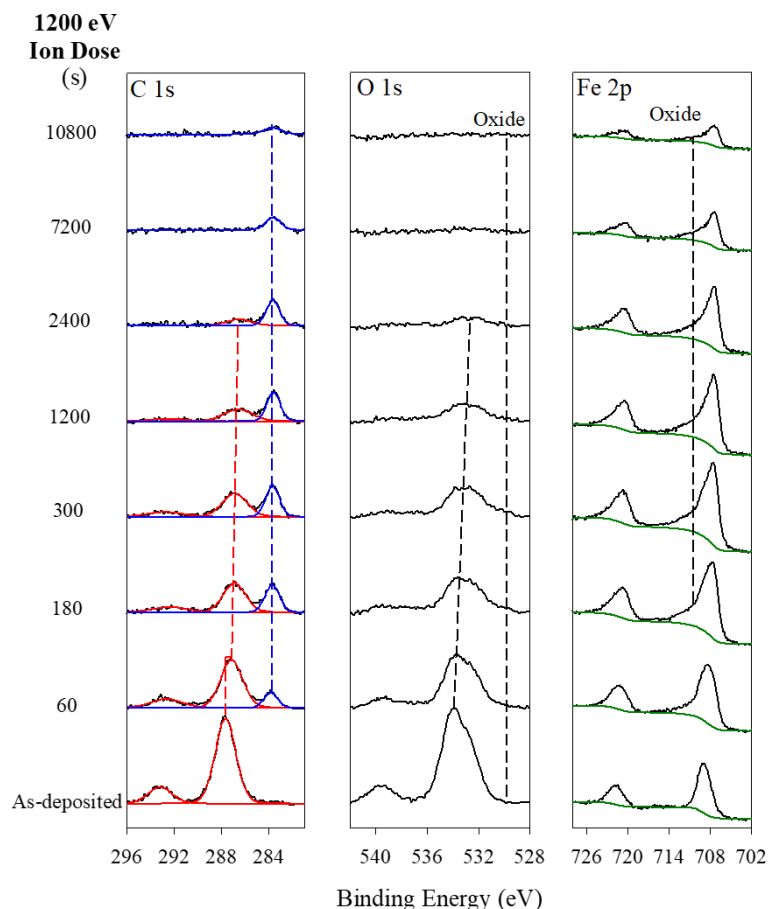regions of adsorbed thin films (1.8 nm) of Fe(CO)$_5$ upon irradiation with 1200
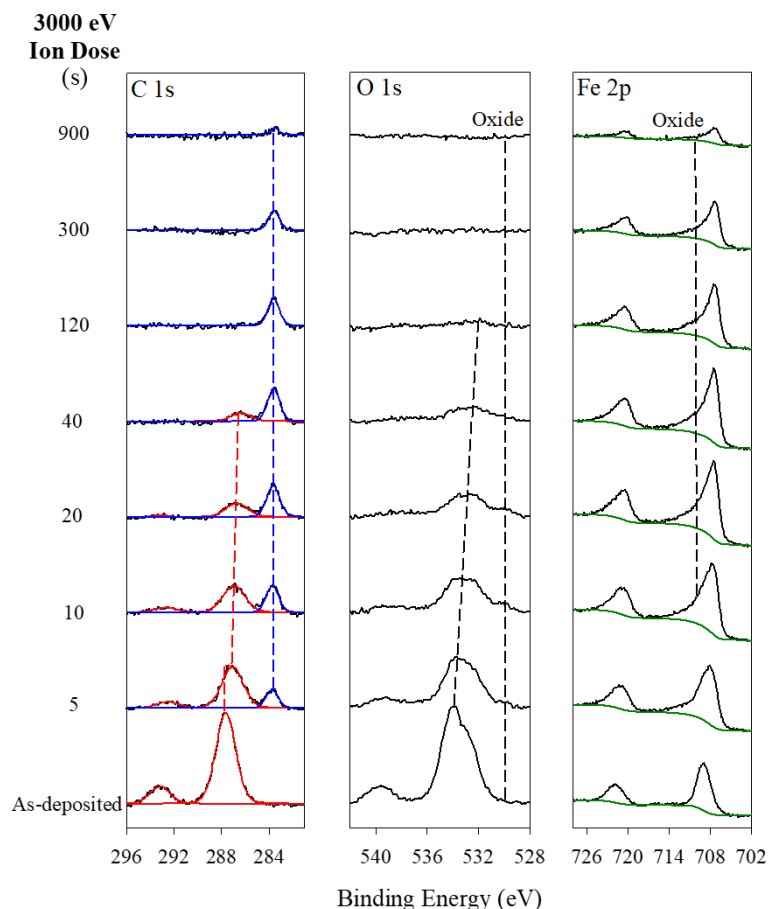
Figure 5.5: Evolution of the C(1s), O(1s), and Fe(2p) XPS regions of ≈ 1.8 nm thin film of adsorbed Fe(CO)$_5$ upon irradiation with 3000 eV argon ions. The bottom spectra represent the un-irradiated film. Speciation is shown in the C(1s) region, where the red line represents the C(1s) peak associated with the precursor carbonyl ligands while the blue lines represent the C(1s) peak associated with the graphitic carbon species in the deposit. The black dashed lines in the O(1s) and Fe(2p) regions indicate oxide growth. The green curves in the Fe(2p) region shows the background. Ion dose is shown on the left-hand side in units of seconds.

eV and 3000 eV Ar$^+$ ions, respectively. Effective dose is given in irradiation time. The as-deposited spectra are shown on the bottom of each region and are similar to those shown previously in Fig. 5.1 and described above. The

evolution of the C (1s) region upon 1200 eV and 3000 eV Ar^+ ion irradiation proceeds in a qualitatively similar manner to that observed upon irradiation with 500 eV electrons - the main CO C (1s) peak at 287.7 eV and the π-π* shakeup peak at 293.2 eV (both shown as red curves in Figs. 5.4 and 5.5) swiftly decrease in energy, while a lower binding energy peak at approximately 283.7 eV (shown as blue curves in Figs. 5.4 and 5.5), associated with graphitic carbon species, grows in. After 7200 s of irradiation with 1200 eV Ar^+ ions or 120 s of irradiation with 3000 eV Ar^+ ions, only the C (1s) peak associated with the graphitic carbon species remains. The graphitic carbon C (1s) peak then decreases in intensity with continued Ar^+ ion irradiation.

Changes in the O (1s) region upon 1200 eV and 3000 eV Ar^+ ion irradiation show much more significant divergence from the manner observed upon irradiation with 500 eV electrons. Upon exposure to either 1200 eV or 3000 eV Ar^+ ions, the asymmetrical main CO O (1s) peak at approximately 533.7 eV and the π-π* shakeup peak at 539.6 eV decrease in intensity and shift to lower binding energy, similarly to the behavior observed upon irradiation with 500 eV electrons. Unlike the behavior associated with electron irradiation, however, a significant oxide O (1s) peak is not observed, although a small shoulder in the oxide region (about 530.0 eV) is observed after about 180 s of irradiation with 1200 eV Ar^+ ions or 5 s of irradiation with 3000 eV Ar^+ ions.

The evolution of the Fe (2p) region upon irradiation with 1200 eV and 3000 eV Ar^+ ions is also substantially different from that observed upon irradiation with 500 eV electrons. Most noticeably, minimal iron oxide formation is observed upon Ar^+ ion irradiation. Additionally, the intensities of the Fe

(2p) peaks decrease substantially at high ion irradiation times, although the complex Fe (2p) background (shown as green curves in Figs. 4 and 5) makes quantitative analysis of the total iron loss upon exposure to Ar^+ ions difficult. The Fe ($2p_{3/2}$) and Fe ($2p_{1/2}$) peaks, initially at 708.8 and 721.7 eV, respectively, shift to lower binding energy, as is observed upon electron irradiation. After 10800 s of 1200 eV Ar^+ irradiation, the Fe ($2p_{3/2}$) and Fe ($2p_{1/2}$) peaks have shifted to 707.5 and 720.4 eV, respectively, while 900 s of 3000 eV Ar^+ irradiation causes the peaks to shift to 707.2 and 720.0 eV, respectively. These binding energies are close to those of metallic iron.[38]

Figures 5.6 and 5.7 show the change in carbon coverage (top), oxygen coverage (center), and Fe ($2p_{3/2}$) peak position (bottom) upon exposure to 1200 eV and 3000 eV Ar^+ ions, respectively. The change in carbon coverage is shown for the total carbon coverage (filled green circles), as well as deconvolution of the C (1s) region into carbonyl carbon coverage (filled red triangles) and graphitic carbon coverage (filled blue squares). The change in total oxygen coverage (filled green circles) is overlaid with the carbonyl carbon coverage (filled red triangles), showing strong correlation between the two loss profiles for irradiation with both 1200 eV and 3000 eV Ar^+ ions. Additionally, the graphitic carbon coverage follows very similar profiles for 1200 eV and 3000 eV Ar^+ ions. Taken together, this suggests that exposure of thin films of $Fe(CO)_5$ to 1200 eV and 3000 eV Ar^+ ions follows similar reaction mechanisms, albeit on differing timescales.

In the first approximately 100 s of 1200 eV Ar^+ ion exposure (Fig. 5.6), the

Figure 5.6: Changes in carbon coverage (top), oxygen coverage (center), and Fe ($2p_{3/2}$) peak position (bottom) upon exposure of ≈ 1.8 nm thin film of adsorbed Fe(CO)$_5$ to 1200 eV Ar$^+$ ions. The change in carbon coverage is shown for the total carbon coverage (filled green circles), as well as deconvolution of the C (1s) region into carbonyl carbon coverage (filled red triangles) and graphitic carbon coverage (filled blue squares). The change in total oxygen coverage (filled green circles) is overlaid with the carbonyl carbon coverage (filled red triangles).

total carbon coverage (filled green circles) decreases by about 40%. Deconvoluting the C (1s) region, the carbonyl carbon coverage (filled red triangles) has decreased by 60 % over this period, while the graphitic carbon coverage (filled
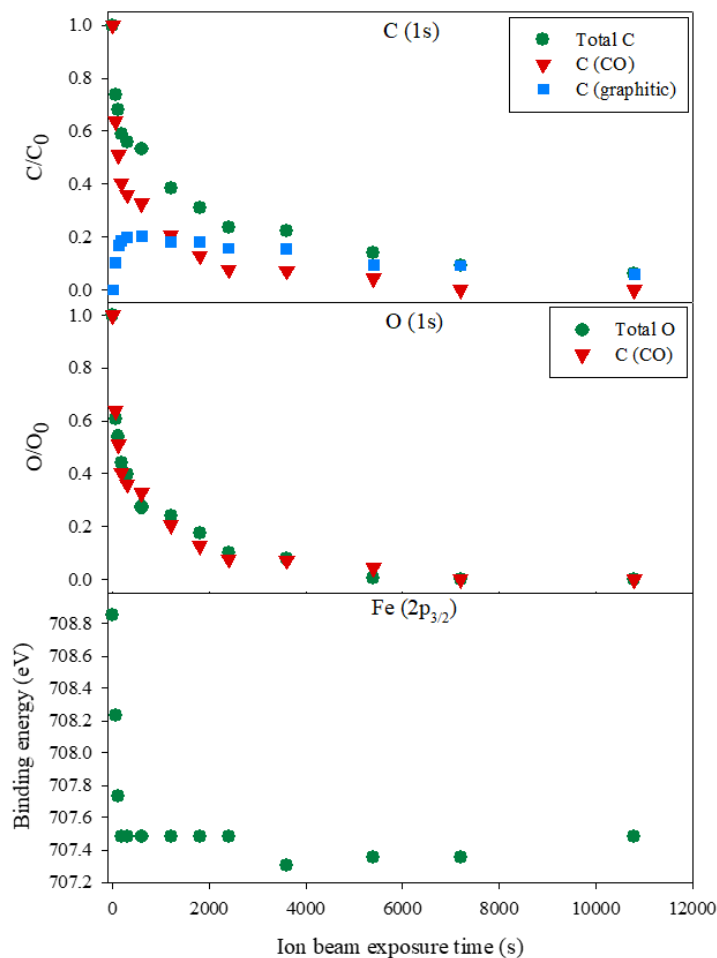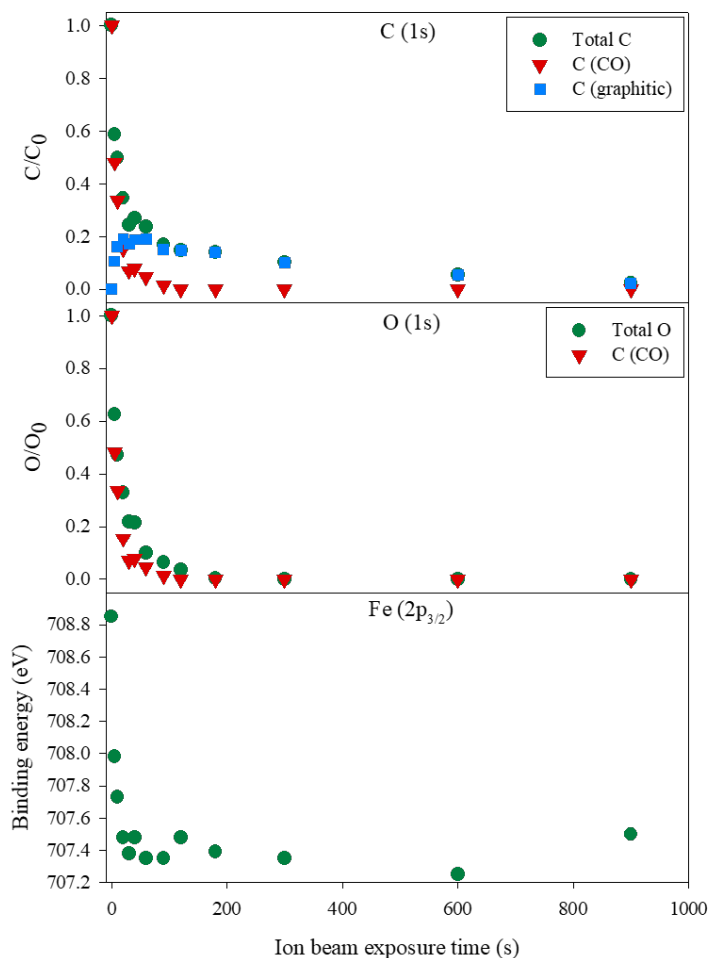
Figure 5.7: Changes in carbon coverage (top), oxygen coverage (center), and Fe ($2p_{3/2}$) peak position (bottom) upon exposure of ≈ 1.8 nm thin film of adsorbed Fe(CO)$_5$ to 3000 eV Ar$^+$ ions. The change in carbon coverage is shown for the total carbon coverage (filled green circles), as well as deconvolution of the C (1s) region into carbonyl carbon coverage (filled red triangles) and graphitic carbon coverage (filled blue squares). The change in total oxygen coverage (filled green circles) is overlaid with the carbonyl carbon coverage (filled red triangles).

blue squares) has increased to about 20 % of original C (1s) signal. The total

oxygen coverage (filled green circles) has decreased by about 60 %, similarly

to the carbonyl carbon coverage. This suggest that about two CO ligands have

left the surface during the first 100 s of 1200 eV Ar^+ ion exposure based on the 40 % decrease in total carbon coverage, while two CO ligands remain intact based on the remaining 40 % of the carbonyl carbon coverage. The final CO ligand has decomposed into graphitic carbon, which remains on the surface, and a reactive oxygen species, which does not. The reactive oxygen species likely does oxidize the iron, as can be seen in Figs. 5.4 and 5.5, but is swiftly sputtered away from the surface. Over this same period, the Fe ($2p_{3/2}$) peak quickly shifts downward in binding energy from 708.9 eV to 707.5 eV. Further 1200 eV Ar^+ ion exposure causes a continued decrease in carbonyl carbon coverage and total oxygen coverage; however, no further shift is observed in the Fe ($2p_{3/2}$) binding energy and the graphitic carbon coverage remains fairly consistent until about 3600 s of 1200 eV Ar^+ ion exposure. After this point, the graphitic carbon coverage steadily decreases.

Turning to Fig. 5.7, in the first approximately 20 s of 3000 eV Ar^+ ion exposure, the total carbon coverage and total oxygen coverage (both filled green circles) each decrease by about 65 %. During this period, the carbonyl carbon coverage (filled red triangles) decreases by about 85 %, while the graphitic carbon coverage (filled blue squares) incre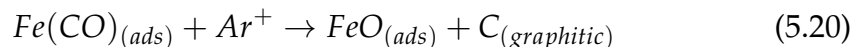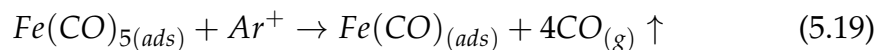ases to about 20 % of the initial carbon coverage. Additionally, the Fe ($2p_{3/2}$) peak shifts downward in binding energy from 708.9 eV to 707.4 eV, similarly to the shift observed during 1200 eV Ar^+ ion exposure. After 120 s of 3000 eV Ar^+ ion irradiation, no carbonyl carbon or oxygen remains on the surface; only graphitic carbon remains. Continued 3000 eV Ar^+ ion exposure causes the graphitic carbon coverage to steadily decrease.

Examining Figs. 5.4 - 5.7, it is evident that upon exposure to either 1200 or 3000 eV Ar^+ ions, adsorbed $Fe(CO)_5$ molecules lose a total of about 4 CO ligands and the remaining CO ligand dissociates into a graphitic carbon species and a reactive oxygen species that oxidizes the iron. The graphitic carbon species is persistent on the surface, while the oxide is swiftly sputtered off the surface. The graphitic carbon species and the iron are also sputtered off the surface, albeit more slowly than the oxide. These reactions can be summarized as:

$$Fe(CO)_{5(ads)} + Ar^+ \rightarrow Fe(CO)_{(ads)} + 4CO_{(g)} \uparrow \tag{5.19}$$

$$Fe(CO)_{(ads)} + Ar^+ \rightarrow FeO_{(ads)} + C_{(graphitic)} \tag{5.20}$$

It is also possible that the graphitic carbon and oxide are produced directly in Eq. 5.19; however, this is not able to be conclusively determined from the present study. After these steps, the remaining iron, oxygen, and graphitic carbon are all sputtered off the surface with continued Ar^+ ion exposure, with the sputter rate of the oxygen being significantly faster than the iron or the carbon. In a similar manner to our understanding of the electron-induced decomposition of adsorbed $Fe(CO)_5$, gas phase studies can be used to understand the initial reaction step (Eq. 5.19). Collisions between 3 kV Ar^+ and $Fe(CO)_5$ were found to primarily produce $[Fe(CO)]^+$,[31] which is similar to the fragmentation observed in the initial Ar^+ ion-induced decomposition step for adsorbed $Fe(CO)_5$ (Eq. 5.19). Interestingly, despite the relatively high energy of the primary Ar^+ ion beam (1200 - 3000 kV), Ar^+ ion irradiation leads preferentially to precursor bond dissociation rather than molecular desorption.

Comparing the effects of low-energy electron and Ar^+ ion exposure, it is evident that the two processes are somewhat mechanistically different. Electron-induced reactions of $Fe(CO)_5$ are characterized by desorption of about 2-3 of the nascent CO ligands (Eq. 5.1) followed by decomposition of the residual CO ligands (Eq. 5.2). In contrast, about 4 CO ligands desorb as a consequence of ion-beam exposure (Eq. 5.19), after which the residual CO ligand decomposes (Eq. 5.20) and the resultant oxide is swiftly sputtered away. Together, this suggests an initial step that is not driven by low energy secondary electrons as the extent of CO ejection is clearly greater for Ar^+-induced decomposition than for electron-induced decomposition.

If we model the energy transfer between the 1200 - 3000 kV incident Ar^+ ions and the adsorbed $Fe(CO)_5$ as a binary collision,[21] then the maximum energy (ΔK_{max}) that can be transferred to the adsorbed $Fe(CO)_5$ is:

$$\Delta K_{max} = K\frac{4m_{ion}m_{mol}}{m_{ion} + m_{mol}} \tag{5.21}$$

Here, K is the kinetic energy of the incident Ar^+ ion, m_{ion} is the mass of the Ar^+ ion and m_{mol} is the mass of the adsorbed molecule ($Fe(CO)_5$). For a 1200 eV incident Ar^+ ion, the maximum energy that can be transferred to an adsorbed $Fe(CO)_5$ molecule is 676 eV, and that for a 3000 eV incident Ar^+ ion is 1690 eV, although the actual energy transfer will be dependent on the impact parameter and thus may range from 0 - ΔK_{max}. This energy should be more than adequate to fully dissociate all CO ligands upon Ar^+ ion impact, as the first Fe-CO bond dissociation energy (BDE) in $Fe(CO)_5$ is 1.82 eV, and subsequent Fe-CO BDEs range from 0.5 - 1.6 eV.[44] However, this

may be complicated by the previously-reported aggregation of $Fe(CO)_5$ on surfaces above 125 K.[32] Aggregation may decrease the amount of energy that may be transferred to an individual $Fe(CO)_5$ molecule due to the increased mass of the aggregate. Despite this, it must be noted that the $C\equiv O$ bond has a BDE of 11.16 eV,[45] significantly higher than the BDEs of the Fe-CO bonds. Because of this, it must be considered possible that secondary electron-induced reactions play an important role in the second step (Eq. 5.20) of Ar^+ ion-induced decomposition of adsorbed $Fe(CO)_5$.

Figure 5.8 shows representative EDX spectra taken at 5 kV from the thickest point in three deposits made by exposing a silicon substrate to 800, 1200, and 1600 eV focused Ar^+ ion beams in the presence of gas phase $Fe(CO)_5$. The images overlaid with each spectrum are SEM images of the respective ion beam induced deposition (IBID) deposits taken at 5 kV. To the right of each spectrum is a compositional analysis showing the atomic percentage of C (red filled circles), O (orange filled triangles), Si (yellow filled squares), and Fe (green filled diamonds) at 11 points taken in a straight line across each IBID deposit as measured by the C K, O K, Fe L, and Si K X-rays. The distance between the points chosen for compositional analysis was not the same for each deposit; thus, individual points cannot be directly compared. Although Ar was detected by EDX, it could not be quantified using the JEOL software.

As can be seen in the EDX spectra in Fig. 5.8, each IBID deposit has areas that are adequately thick to block all signal from the silicon substrate using a 5 kV electron beam. The deposits are primarily comprised of iron, with some contamination from carbon, oxygen, and argon. The SEM images show that

167
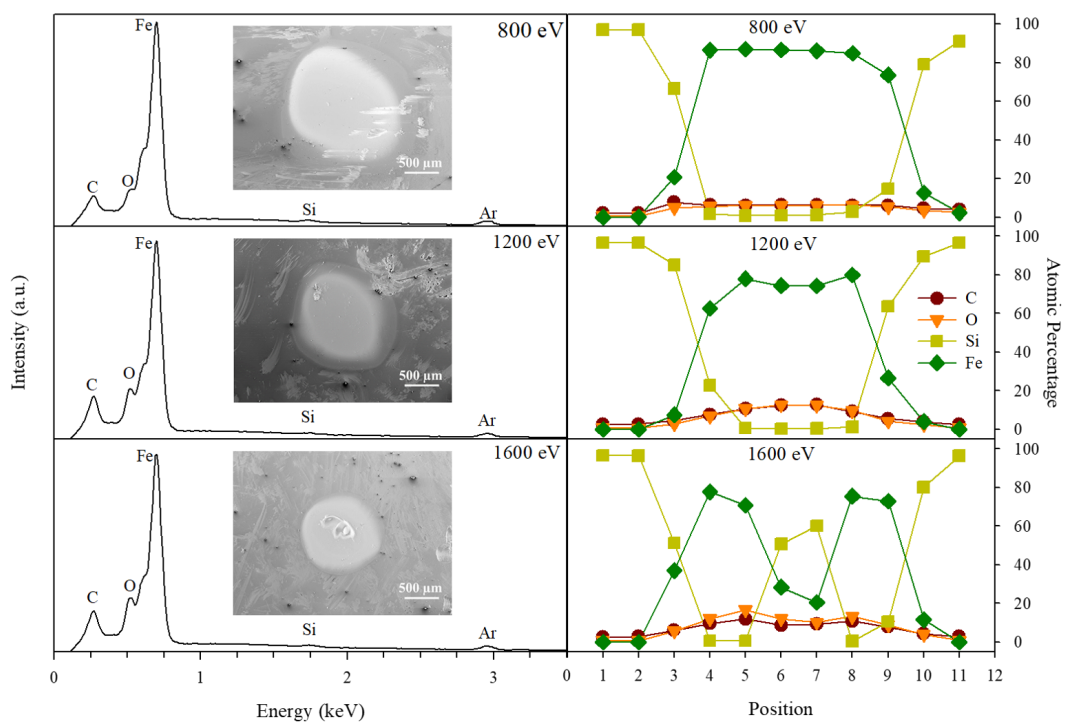
Figure 5.8: Representative EDX spectra, SEM images, and compositional analysis at 5 kV of IBID deposits made using $Fe(CO)_5$ and incident Ar^+ beam energies of 800, 1200, and 1600 eV.

the deposition area becomes smaller with increasing incident ion beam energy, likely due to the tighter focus of the ion beam at higher incident energies. As can be seen in the compositional analysis, the deposition performed using an 800 eV incident ion beam has a composition of 86.9 at. % Fe, 6.2 at. % C, 6.1 at. % O, and 0.8 at. % Si ($\approx$ 14:1:1 Fe:C:O). The 1200 eV incident ion beam produced a deposit composed of 77.9 at. % Fe, 10.7 at. % C, 10.7 at. % O, and 0.7 at. % Si ($\approx$ 7:1:1 Fe:C:O). The deposition produced using a 1600 eV incident ion beam was composed of 77.6 at. % Fe, 9.6 at. % C, 12.1 at. % O, and 0.7 at. % Si ($\approx$ 8:1:1 Fe:C:O). Thus, an increase in energy of the

incident argon ion beam produces a slight decrease in the purity of the deposit, with an increase in carbon and oxygen contamination. However, due to the tightening focus at of the primary argon beam with increased energy, it cannot be determined whether the differences between the deposits are caused by the higher energy of the incident Ar^+ ions or the higher ion flux at higher beam energies. Additionally, the increased ion beam energy produces a deposit with a thinner center, as can be seen in Fig. 5.8. This likely reflects an increase in ion sputtering at the center of the deposit, where the ion flux is likely to be the highest.

Comparing the IBID deposits to the UHV Ar^+ ion-induced decomposition of adsorbed films of $Fe(CO)_5$, the deposits have a slightly different iron-to-carbon-to-oxygen ratio (Fe:C:O) than might be anticipated from the UHV experiments. In the UHV experiments, about 4 CO ligands were lost in the first Ar^+ ion-induced decomposition step. This was followed by decomposition of the remaining ligand into a graphitic carbon species, which was persistent on the surface, and an oxide species, which was swiftly sputtered away. Because of this, the carbon concentration in the deposit was expected to be higher than the oxygen concentration; however, there were quite similar levels of carbon and oxygen contamination in all three IBID deposits. This observed discrepancy between the two experiments might be explained by the deposit growth rate limiting the sputtering of the oxide; however, the Fe:C:O ratio is also much higher in the deposit than would be expected if the oxide and graphitic remained in the deposit (expected value = 1:1:1). It must be noted here that, due to the higher temperature of the IBID deposition

169

as compared to the UHV experiments, CO found in the intermediates (here, $Fe(CO)_{(ads)}$) may thermally desorb after the initial deposition step (Eq.5.19), which is particularly likely here due to the high thermal efficiency of CO loss from $Fe(CO)_5$. This supports the hypothesis that CO desorption and the decomposition of the residual CO ligand into graphitic carbon and reactive oxygen species take place in two successive Ar^+-induced reaction steps (Eq. 5.19 and 5.20). This indicates that nearly pure iron deposits may be made from $Fe(CO)_5$ using low-energy ion beams at room temperature.

5.4 Conclusions

In this contribution, the low energy electron- (500 eV) and argon ion- (1200 - 3000 eV) induced decomposition of adsorbed $Fe(CO)_5$ were studied and compared to previous gas phase and surface studies. The initial decomposition step for electron-induced decomposition was found to produce a loss of $2-3$ CO ligands, followed by the electron-induced decomposition of the residual CO ligands to produce a graphitic carbon species and iron oxide. For argon ion-induced decomposition, the initial step comprised the desorption of 4 CO ligands, followed by the decomposition of the residual CO ligand and eventual sputtering of the oxide and graphitic carbon, as well as the iron. Thus, the initial ion-induced decomposition step appears to proceed via collision-induced energy transfer, while secondary electron-induced reactions may be important in the second ion-induced decomposition step. Deposits made from $Fe(CO)_5$ using IBID in a UHV chamber demonstrated that high-purity iron deposits may be made with low energy IBID using $Fe(CO)_5$.

References

[1] J. M. De Teresa, A Fernández-Pacheco, R Córdoba, L Serrano-Ramón, S Sangiao, M. R. Ibarra, *Journal of Physics D: Applied Physics* **2016**, *49*, 243003.

[2] S. D. Bader, *Reviews of Modern Physics* **2006**, *78*, 1–15.

[3] J. R. Childress, R. E. Fontana, *Comptes Rendus Physique* **2005**, *6*, 997–1012.

[4] D. A. Allwood, G. Xiong, M. D. Cooke, C. C. Faulkner, D Atkinson, N Vernier, R. P. Cowburn, *Science* **2002**, *296*, 2003–2006.

[5] S. S. P. Parkin, M. Hayashi, L. Thomas, *Science (New York N.Y.)* **2008**, *320*, 190–4.

[6] I. Utke, P. Hoffmann, J. Melngailis, *Journal of Vacuum Science & Technology B: Microelectronics and Nanometer Structures* **2008**, *26*, 1197.

[7] J. Melngailis, *Journal of Vacuum Science & Technology B: Microelectronics and Nanometer Structures* **1987**, *5*, 469.

[8] M. Gavagnin, H. D. Wanzenboeck, M. M. Shawrav, D. Belic, S. Wachter, S. Waid, M. Stoeger-Pollach, E. Bertagnolli, *Chemical Vapor Deposition* **2014**, *20*, 243–250.

[9] T. Lukasczyk, M. Schirmer, H.-P. Steinrück, H. Marbach, *Small* **2008**, *4*, 841–846.

[10] M. A. Bruk, E. N. Zhikharev, E. I. Grigor'ev, A. V. Spirin, V. A. Kal'nov, I. E. Kardash, *High Energy Chemistry* **2005**, *39*, 65–68.

[11] L. A. Rodríguez, L. Deen, R. Córdoba, C. Magén, E. Snoeck, B. Koopmans, J. M. De Teresa, *Beilstein Journal of Nanotechnology* **2015**, *6*, 1319–1331.

[12] M. Takeguchi, M. Shimojo, K. Mitsuishi, M. Tanaka, R. Che, K. Furuya, *Journal of Materials Science* **2006**, *41*, 4532–4536.

[13] C. Sanz-Martín, C. Magén, J. M. D. Teresa, *Nanomaterials* **2019**, *9*, 1715.

[14] R. L. Kubena, F. P. Stratton, T. M. Mayer in *Advanced Techniques for Integrated Circuit Processing, Vol. Proc. SPIE 1392*, (Eds.: J. A. Bondur, T. R. Turner), International Society for Optics and Photonics, **1991**, pp. 595–597.

[15] R. M. Thorman, R. K. T. P., D. H. Fairbrother, O. Ingólfsson, *Beilstein Journal of Nanotechnology* **2015**, *6*, 1904–1926.

[16] S. Engmann, M. Stano, S. Matejčík, O. Ingólfsson, *Physical chemistry chemical physics : PCCP* **2012**, *14*, 14611–8.

[17] J. D. Wnuk, J. M. Gorham, S. G. Rosenberg, W. F. van Dorp, T. E. Madey, C. W. Hagen, D. H. Fairbrother, *The Journal of Physical Chemistry C* **2009**, *113*, 2487–2496.

[18] K. Wnorowski, M. Stano, W. Barszczewska, A. Jówko, Š. Matejčík, *International Journal of Mass Spectrometry* **2012**, *314*, 42–48.

[19] K. Wnorowski, M. Stano, C. Matias, S. Denifl, W. Barszczewska, Š. Matejčík, *Rapid Communications in Mass Spectrometry* **2012**, *26*, 2093–2098.

[20] S. G. Rosenberg, M. Barclay, D. H. Fairbrother, *Physical Chemistry Chemical Physics* **2013**, *15*, 4002–4015.

[21] A. D. Dubner, A. Wagner, J. Melngailis, C. V. Thompson, *Journal of Applied Physics* **1991**, *70*, 665–673.

[22] J. S. Ro, C. V. Thompson, J. Melngailis, *Journal of Vacuum Science & Technology B: Microelectronics and Nanometer Structures* **1994**, *12*, 73.

[23] S. Lipp, L. Frey, C. Lehrer, E. Demm, S. Pauthner, H. Ryssel, *Microelectronics Reliability* **1996**, *36*, 1779–1782.

[24] P. Chen, H. W. M. Salemink, P. F. A. Alkemade, *Journal of Vacuum Science & Technology B: Microelectronics and Nanometer Structures* **2009**, *27*, 2718.

[25] P. Chen, E. van Veldhoven, C. A. Sanford, H. W. M. Salemink, D. J. Maas, D. A. Smith, P. D. Rack, P. F. A. Alkemade, *Nanotechnology* **2010**, *21*, 455302.

[26] R. M. Thorman, S. J. Matsuda, L. McElwee-White, D. H. Fairbrother, *The Journal of Physical Chemistry Letters* **2020**, *11*, 2006–2013.

[27] M. Allan, M. Lacko, P. Papp, Š. Matejčík, M. Zlatar, I. I. Fabrikant, J. Kočišek, J. Fedor, *Physical Chemistry Chemical Physics* **2018**, *20*, 11692–11701.

[28] M. Lacko, P. Papp, K. Wnorowski, Š. Matejčík, *The European Physical Journal D* **2015**, *69*, 84.

[29] J. Lengyel, J. Fedor, M. Fárník, *The Journal of Physical Chemistry C* **2016**, *120*, 17810–17816.

[30] J. Lengyel, P. Papp, Š. Matejčík, J. Kočišek, M. Fárník, J. Fedor, *Beilstein Journal of Nanotechnology* **2017**, *8*, 2200–2207.

[31] S. Indrajith, P. Rousseau, B. A. Huber, C. Nicolafrancesco, A. Domaracka, K. Grygoryeva, P. Nag, B. Sedmidubská, J. Fedor, J. Kočišek, *The Journal of Physical Chemistry C* **2019**, *123*, 10639–10645.

[32] C. Hauchard, P. A. Rowntree, *Canadian Journal of Chemistry* **2011**, *89*, 1163–1173.

[33] S. Massey, A. D. Bass, L. Sanche, *The Journal of Physical Chemistry C* **2015**, *119*, 12708–12719.

[34] J. F. Moulder, J. Chastain, *Handbook of x-ray photoelectron spectroscopy : a reference book of standard spectra for identification and interpretation of XPS data*, Physical Electronics Division, Perkin-Elmer Corp, **1992**, p. 259.

[35] E. W. Plummer, W. R. Salaneck, J. S. Miller, *Physical Review B* **1978**, *18*, 1673–1701.

[36] F. Zaera, *Journal of Vacuum Science & Technology A: Vacuum Surfaces and Films* **1989**, *7*, 640–645.

[37] D. Moon, D. Dwyer, S. Bernasek, *Surface Science* **1985**, *163*, 215–229.

[38] F. Zaera, *Langmuir* **1991**, *7*, 1188–1191.

[39] A. N. Mansour, R. A. Brizzolara, *Surface Science Spectra* **1996**, *4*, 345–350.

[40] T. Fujii, F. M. F. de Groot, G. A. Sawatzky, F. C. Voogt, T. Hibma, K. Okada, *Physical Review B* **1999**, *59*, 3195–3202.

[41] S. G. Rosenberg, M. Barclay, D. H. Fairbrother, *The Journal of Physical Chemistry C* **2013**, *117*, 16053–16064.

[42] R. K. T. P., I. Unlu, S. Barth, O. Ingólfsson, D. H. Fairbrother, *The Journal of Physical Chemistry C* **2018**, *122*, 2648–2660.

[43] I. Unlu, J. A. Spencer, K. R. Johnson, R. M. Thorman, O. Ingólfsson, L. McElwee-White, D. H. Fairbrother, *Physical Chemistry Chemical Physics* **2018**, *20*, 7862–7874.

[44] O. González-Blanco, V. Branchadell, *The Journal of Chemical Physics* **1999**, *110*, 778–783.

[45] J. A. Dean, *Lange's handbook of chemistry*, 15th ed., McGraw-Hill, New York, **1999**.

CURRICULUM VITAE

Rachel M. Thorman

2522 N Calvert St, Apt 3   (201) 286-3412

Baltimore, MD 21218   rachel.thorman@gmail.com

Education

Johns Hopkins University	9/2013 – present
Baltimore, MD	Chemistry

- Advisor: Professor D. Howard Fairbrother

University of Iceland	Ph.D. 10/2017
Reykjavik, Iceland	Chemistry

- Advisor: Professor Oddur Ingólfsson

Princeton University	B.A. 5/2011
Princeton, NJ	Chemistry

- Advisor: Professor Steven L. Bernasek (now at Yale-NUS)

Professional Experience

Graduate Research Assistant   1/2014 – present

Fairbrother Lab – Johns Hopkins University, Baltimore, MD, USA

Ingólfsson Lab – University of Iceland, Reykjavik, Iceland

- Headed collaboration between laboratories at University of Iceland, Johns Hopkins University, and other universities to study fundamental chemistry underlying nanofabrication techniques
- Performed and published research on fundamental low energy electron-induced reactions of organometallic precursors for focused electron beam induced deposition (FEBID) in the gas phase and on surfaces
- Performed and published research on fundamental low energy ion-induced surface reactions of organometallic precursors for focused ion beam induced deposition (FIBID)
- Received grant from COST Action CM1301 for short-term scientific mission to EMPA (Thun, Switzerland) to study *in situ* FEBID of organometallic precursors under Dr. Ivo Utke
- Used and analyzed data from mass spectrometry (QMS), X-ray photoelectron spectroscopy (XPS), Auger electron spectroscopy (AES), secondary electron microscopy (SEM), energy-dispersive X-ray spectroscopy (EDX), and temperature-programmed desorption (TPD)
- Maintained and repaired high vacuum and ultra-high vacuum (UHV) equipment
- Performed quantum chemical calculations on electron interactions with organometallic molecules for comparison to gas phase data
- Mentored visiting researchers and new students in use and maintenance of laboratory instrumentation

Teaching Assistant

University of Iceland   9/2015 – 12/2016

- Supervised third year chemistry students in physical chemistry lab
- Graded laboratory assignments, assisted in English science writing

Johns Hopkins University   9/2013 – 1/2014

- Supervised 20-student first year undergraduate laboratory class
- Held biweekly help sessions for lecture and laboratory classes

Research Technician – Hydrocarbon Sciences   6/2012 – 7/2013
ExxonMobil Research & Engineering
Annandale, NJ, USA

- Supported hydrocarbon science research with XPS
- Supported solvent-assisted hydroprocessing research with laboratory-scaled deasphalting and data organization and analysis

Undergraduate Research Assistant   6/2009 – 5/2011
Bernasek Lab – Princeton University
Princeton, NJ, USA

- Performed original research using XPS, atomic force microscopy (AFM), infrared spectrometry (FT-IR), alkali metal deposition, and surface functionalization

Publications

- *Paper*: R. M. Thorman, P. A. Jensen, J.-C. Yu, S. J. Matsuda, L. McElwee-White, O. Ingólfsson, and D. H. Fairbrother. "Electron-induced reactions of $Ru(CO)_4I_2$: gas phase, surface, and FEBID." (submitted, 2020).
- *Paper*: R. M. Thorman, S. J. Matsuda, L. McElwee-White, and D. H. Fairbrother. "Identifying and rationalizing the differing surface reactions of low-energy electrons and ions with an organometallic precursor." J. Phys. Chem. Lett. 11, 2006-2013 (2020).
- *Paper*: F. Ferreira da Silva, R. M. Thorman, R. Bjornsson, H. Lu, L. McElwee-White, and O. Ingólfsson. "Dissociation of the FEBID precursor *cis*-Pt(CO)2Cl2 driven by low-energy electrons." Phys. Chem. Chem. Phys. 22, 6100-6108 (2020).
- *Paper*: M. Cipriani, R. M. Thorman, C. R. Brewer, L. McElwee-White, and O. Ingólfsson. "Dissociative ionization of the potential focused electron beam induced deposition precursor π-allyl ruthenium (II) tricarbonyl bromide, a combined theoretical and experimental study." Eur. Phys. J. D 73, 227 (2019).
- *Paper*: W. G. Carden, R. M. Thorman, I. Unlu, K. A. Abboud, D. H. Fairbrother, and L. McElwee-White. "Design, synthesis, and evaluation of CF_3AuCNR precursors for focused electron beam-induced deposition of gold." ACS Appl. Mater. Interfaces 11 (12), 11976-11987 (2019).
- *Graduate Thesis*: "Low-energy electron interactions with two organometallic precursors for focused electron beam induced deposition: $(\eta^3\text{-}C_3H_5)Ru(CO)_3Br$ and $(\eta^5\text{-}Cp)Fe(CO)_2Mn(CO)_5$;" University of Iceland (unpublished, 2017).
- *Paper*: I. Unlu, J. A. Spencer, K. R. Johnson, R. M. Thorman, O. Ingólfsson, L. McElwee-White, and D. H. Fairbrother. "Electron induced surface reactions of $(\eta^5\text{-}C_5H_5)Fe(CO)_2Mn(CO)_5$, a potential heterobimetallic precursor for focused electron beam induced deposition (FEBID)." Phys. Chem. Chem. Phys. 20, 7862-7874 (2018).
- *Paper*: R. M. Thorman, I. Unlu, K. Johnson, R. Bjornsson, L. McElwee-White, D. H. Fairbrother, and O. Ingólfsson. "Low energy electron-induced decomposition of $(\eta^5\text{-}$

Cp)Fe(CO)$_2$Mn(CO)$_5$, a potential bimetallic precursor for focused electron beam induced deposition of alloy structures." Phys. Chem. Chem. Phys. 20, 5644-5656 (2018).

- *Paper*: R. M. Thorman, J. A. Brannaka, L. McElwee-White, and O. Ingólfsson. "Low energy electron-induced decomposition of (η^3-C$_3$H$_5$)Ru(CO)$_3$Br, a potential focused electron beam induced deposition precursor with a heteroleptic ligand set." Phys. Chem. Chem. Phys. 19, 13264-13271 (2017).
- *Paper*: R. M. Thorman, R. Bjornsson, and O. Ingólfsson. "Computational study of dissociative electron attachment to π-allyl ruthenium (II) tricarbonyl bromide." Eur. Phys. J. D 70, 164 (2016).
- *Paper*: R. M. Thorman, R. K. T. P., D. H. Fairbrother, and O. Ingólfsson. "The role of low-energy electrons in focused electron beam induced deposition: four case studies of representative precursors." Beilstein J. Nanotechnol. 6, 1904–1926 (2015).
- *Paper*: D. P. Cherney, C. Wu, R. M. Thorman, J. L. Hegner, M. S. Yeganeh, D. Ferrughelli, and E. Ulysse. "Investigating the Impact of Crude Oil Solubility on Water-in-Oil Emulsion Stability and Its Relation to Molecular Composition of Crude Oil at the Oil–Water Interface." Energy Fuels 29 (6), 3616–3625 (2015).
- *Paper*: A. M. Hibberd, R. M. Thorman, J. D. Wnuk, and S. L. Bernasek. "Rb deposition on alkanethiolate monolayers on Au." J. Appl. Phys. 112, 023110 (2012).
- *Undergraduate Thesis*: "Investigation of the effects of alkali metal deposition on model atomic magnetometer wall coatings;" Princeton University (unpublished, 2011).

Presentations

- *Talk*: "Surface reactions of low energy electrons and ions with organometallic precursors and their relevance to charged particle deposition processes." Talk presented at: AVS 66th International Symposium and Exhibition; October, 2019; Columbus, OH, USA
- *Poster*: "Low-energy electron interactions with the hetero-binuclear FEBID precursor (η^5-Cp)Fe(CO)$_2$Mn(CO)$_5$." Poster presented at: CELINA 2017 – 4th Meeting of COST Action CM1301; September 2017; Porto, Portugal.
- *Posters*: "Computational study of dissociative electron attachment to π-allyl ruthenium (II) tricarbonyl bromide;" "Low energy electron-induced dissociation mechanisms of dicobalt octacarbonyl." Posters presented at: CELINA 2016 – 3rd Meeting of COST Action CM1301; May 2016; Krakow, Poland.
- *Posters*: "A side-by-side comparison of comprehensive gas phase, surface, and *in-situ* studies of two FEBID precursors: MeCpPtMe$_3$ and π-C$_3$H$_5$Ru(CO)$_3$Br." Posters presented at: CELINA 2015 – 2nd Meeting of COST Action CM1301; May 2015; Bratislava, Slovakia.
- *Poster*: "Low Energy Electron Interactions with π-Allyl Ruthenium Tricarbonyl Bromide in the Gas Phase." Poster presented at: FEBIP 2014 - 5th workshop on Focused Electron Beam Induced Processing; July 2014; Frankfurt am Main, Germany.
- *Poster*: "Characterization of π-allyl ruthenium tricarbonyl bromide as a potential EBID precursor by gas-phase and surface studies." Poster presented at: CELINA 2014 – 1st Meeting of COST Action CM1301; March 2014; Erlangen, Germany.
- *Talk*: "Direct-write nanofabrication: writing nanostructures with an electron-beam 'pen'." Talk given at: Efnís Conference 2015; October 2015; Reykjavík, Iceland.

- *Talk*: "The role of low-energy electrons in focused electron beam induced deposition of ruthenium-centered precursors." Talk given at: CELINA 2015 – 2nd Meeting of COST Action CM1301; May 2015; Bratislava, Slovakia.
- *Talk*: "The role of low-energy electrons in focused electron beam induced deposition of ruthenium-centered precursors." Talk given at: Chemistry and Biochemistry Seminar Series, University of Iceland; December 2014; Reykjavik, Iceland.
- *Talk*: "Low energy electron interactions with a typical electron beam induced deposition (EBID) precursor – π-allyl ruthenium tricarbonyl bromide." Talk given at: SPIG 2014 – 27th Summer School and International Symposium on the Physics of Ionized Gases; August 2014; Belgrade, Serbia.